thesis plag.pdf

Delhi Technological University

Document Details

Submission ID
trn:oid:::27535:116778405

Submission Date
Oct 15, 2025, 1:25 PM GMT+5:30

Download Date
Oct 15, 2025, 1:48 PM GMT+5:30

File Name
thesis plag.pdf

File Size
7.5 MB

145 Pages

40,339 Words

185,349 Characters

7% Overall Similarity

The combined total of all matches, including overlapping sources, for each database.

Filtered from the Report

- Bibliography
- Quoted Text
- Cited Text
- Small Matches (less than 10 words)
- Crossref database

Exclusions

- 44 Excluded Matches

Match Groups

50 Not Cited or Quoted 7%
Matches with neither in-text citation nor quotation marks

0 Missing Quotations 0%
Matches that are still very similar to source material

0 Missing Citation 0%
Matches that have quotation marks, but no in-text citation

0 Cited and Quoted 0%
Matches with in-text citation present, but no quotation marks

Top Sources

5% Internet sources
3% Publications
6% Submitted works (Student Papers)

Integrity Flags

1 Integrity Flag for Review

Replaced Characters
263 suspect characters on 55 pages
Letters are swapped with similar characters from another alphabet.

Our system's algorithms look deeply at a document for any inconsistencies that would set it apart from a normal submission. If we notice something strange, we flag it for you to review.

A Flag is not necessarily an indicator of a problem. However, we'd recommend you focus your attention there for further review.

Match Groups

- **50** Not Cited or Quoted 7%
  Matches with neither in-text citation nor quotation marks
- **0** Missing Quotations 0%
  Matches that are still very similar to source material
- **0** Missing Citation 0%
  Matches that have quotation marks, but no in-text citation
- **0** Cited and Quoted 0%
  Matches with in-text citation present, but no quotation marks

Top Sources

- 5% Internet sources
- 3% Publications
- 6% Submitted works (Student Papers)

Top Sources

The sources with the highest number of matches within the submission. Overlapping sources will not be displayed.

1	Internet	1library.net <1%
2	Submitted works	Victoria University on 2020-01-18 <1%
3	Submitted works	Jawaharlal Nehru Technological University Kakinada on 2014-02-25 <1%
4	Internet	dspace.cc.tut.fi <1%
5	Publication	Rico, Ulises Pineda. "Link Optimisation for MIMO Communication Systems.", The ... <1%
6	Submitted works	University of Bradford on 2007-05-30 <1%
7	Submitted works	Higher Education Commission Pakistan on 2016-01-11 <1%
8	Internet	www.researchgate.net <1%
9	Internet	ia902803.us.archive.org <1%
10	Internet	blog.smowcode.com <1%

11 Internet
info.daviscollege.edu <1%

12 Submitted works
University of Bradford on 2010-08-30 <1%

13 Internet
pt.slideshare.net <1%

14 Internet
www.sutel.go.cr <1%

15 Submitted works
National Institute of Technology, MIZORAM on 2025-02-25 <1%

16 Internet
pdffox.com <1%

17 Internet
www.jpier.org <1%

18 Submitted works
Higher Education Commission Pakistan on 2010-05-21 <1%

19 Submitted works
International Islamic University Chittagong on 2022-12-20 <1%

20 Submitted works
University of Bedfordshire on 2020-03-24 <1%

21 Submitted works
University of Leeds on 2021-07-29 <1%

22 Internet
iris.rais.is <1%

23 Submitted works
South Bank University on 2025-04-16 <1%

24 Submitted works
University of Bristol on 2006-11-01 <1%

25 Submitted works
University of Northumbria at Newcastle on 2010-08-04 <1%

26 Internet
d-scholarship.pitt.edu <1%

27 Internet
dspace.lib.cranfield.ac.uk <1%

28 Internet
dspace.library.uvic.ca <1%

29 Submitted works
Macquarie University on 2017-11-06 <1%

30 Publication
Majnaric Borad, Jeffrey Kezele. "Applications of Loop-Based Advanced Electromag... <1%

31 Submitted works
National Institute of Technology, Hamirpur on 2019-05-30 <1%

32 Submitted works
University Tun Hussein Onn Malaysia on 2013-10-23 <1%

33 Submitted works
University of Hong Kong on 2018-07-11 <1%

34 Submitted works
University of Sheffield on 2023-10-16 <1%

35 Internet
dlibrary.univ-boumerdes.dz:8080 <1%

36 Internet
ia801402.us.archive.org <1%

37 Internet
umpir.ump.edu.my <1%

38 Publication
Al Naiemy, Yahiea M. H.. "Innovations in Antenna Designs Based Artificial Materi... <1%

39 Submitted works
Arts, Sciences & Technology University In Lebanon on 2024-07-21 <1%

40 Publication
Binod Kumar Kanaujia, Surendra Kumar Gupta, Jugul Kishor, Deepak Gangwar. "P... <1%

41 Submitted works
Higher Education Commission Pakistan on 2010-05-20 <1%

42 Submitted works
Middle East Technical University on 2014-08-21 <1%

43 Publication
Sessions, Ryan. "Applications of Mathematical Optics and the Electrodynamics of ... <1%

44 Submitted works
University of Bradford on 2023-02-28 <1%

45 Internet
hal.science <1%

46 Internet
qmro.qmul.ac.uk <1%

47 Internet
www.coursehero.com <1%

48 Internet
www.ukessays.com <1%

Abstract

The surge in demand for high data rates has resulted in the exponential growth of wireless communication systems. Thus, there is a requirement for compact, high gain, and Wideband/ Ultra-wideband (UWB) antennas capable of supporting 5G and beyond communication networks. With increasing reliance on high data rates, wide impedance bandwidths (BW), Low-latency, and seamless connectivity, antenna systems must evolve to address challenges such as spectrum congestion, gain enhancement, polarisation control, and size reduction.

The antenna parameters, such as Gain, Directivity, BW, Polarisation, Radiation Patterns and Efficiency, can be '*enhanced*' by introducing the Metamaterials (MMTs)/ Metasurfaces (MSs). This thesis presents an in-depth investigation into the design and analysis of *gain enhanced microstrip antennas* using MTMs/ MSs, and 3D-printed Metastructures. The research is focused on Sub-6 GHz, X-band, and millimetre-Wave (mm-Wave) frequency ranges, covering applications in Internet of Things (IoT), Internet of Vehicles (IoV), CubeSat systems, point-to-point (p2p) terrestrial 5G communication, and Small 5G Base stations.

In the Sub-6 GHz band, a UWB Multiple Input Multiple Output (MIMO) antenna is designed to achieve a wide impedance BW of 2.37 GHz to 8 GHz with a fractional BW of 108.58%. The antenna, intended for IoT/IoV applications, integrates an artificial magnetic conductor (AMC) with dual rings to generate dual resonances, enhancing gain and improving port isolation. The 5 × 8 AMC array placement enhances gain up to 7 dBi from a baseline of 2.3 dBi, while isolation is improved to >19.66 dB. Furthermore, essential MIMO performance metrics such as ECC (<0.0037), CCL (<0.12 bits/s/Hz), and TARC (< -10 dB) remain within acceptable limits. The compact size and wide operational BW of the design make it suitable for IoT, WiFi, LTE, WiMax, and WiFi-6E bands.

For CubeSat applications, a circularly polarised (CP) antenna is proposed using a polarisation reconfigurable metasurface (PRMS). By forming a Fabry–Perot cavity with a 9 × 9 PRMS array, the antenna achieves an Axial Ratio BW (ARBW) of 2.31 GHz, closely matched with an impedance BW of 2.41 GHz. The design enhances the gain from 7.3 dBi to 17.1 dBi while achieving compatibility with both right-hand and left-hand CP waves. This antenna design addresses one of the critical challenges in CP antenna design, where ARBW is typically narrower than impedance BW, thereby making the antenna suitable for satellite based communication.

In the X-band spectrum, a phase gradient metasurface flat lens (PGMS-FL) is introduced to attain a high gain, narrow beams for p2p terrestrial 5G communication. The PGMS-FL array achieves beamwidths between 13.2° and 16.5° with a maximum gain of 17.7 dBi at 11.2 GHz. The polarisation-insensitive nature of the PGMS unit cells ensures

stable CP performance, making the antenna a viable candidate for terrestrial p2p 5G communication.

Four distinct antennas are designed and analysed at mm-Wave frequencies to overcome propagation losses and achieve high capacity wireless links. A UWB AMC array is used to enhance the gain of a MIMO antenna from 8.5 dBi to 12.21 dBi while maintaining port isolation above 19 dB. A second MIMO antenna, integrates a PGMS lens for beam tilting to $\pm$ 24º, enabling robust non-line-of-sight (NLOS) communication to improve SNR. The third design incorporates double-negative (DNG) unit cells to achieve a gain improvement of 4 dB and a front-to-back ratio increase from 10.81 dB to 20.6 dB, enhancing link reliability. Finally, a 3D-printed metastructure array embedded in a planar dipole antenna achieves flat gain with 0.45 dB variance, i.e. 11.07 dBi to 11.45 dBi across 22 GHz to 26.6 GHz.

The findings of this thesis emphasise the importance of unit cell design in gain enhancement, BW widening, and polarisation stability. Symmetry, polarisation insensitivity, and angular stability emerge as key factors for optimising metastructures for antenna applications. Integrating AMCs, PRMS, PGMS, DNGs, and 3D-printed metastructures across multiple frequency bands demonstrates significant gain enhancements while maintaining compact profiles.

Overall, the research outcomes provide compact, high-performance antenna designs suitable for 5G communication. The proposed antennas cover diverse frequency bands, which include WiFi/ WiMax/ Bluetooth, Mid-band, Sub-6 GHz, WiFi-6E X-band, MVDDS, and mm-Wave enables applications in IoT/IoV, terrestrial 5G networks, CubeSat communication, and broadband satellite services. By addressing challenges such as narrow BW, low gain, polarisation mismatching, and size, this thesis contributes to the advancement of antenna designs that are efficient, reliable, and adaptable to the evolving needs of modern communication systems.

The major highlights of this research are:

- Design antennas to cover newly defined frequencies by the FCC *(WiFi-6E* and *MVDDS)* with an enhanced gain.
- To enhance the ARBW of the CP antenna and increase the gain using MMT or a metal cavity, with a small structure.
- Design an antenna with gain enhancement for wide impedance BW, low profile and high directivity.
- To achieve enhanced gain enhancement for UWB antennas, maintaining antenna size as minimal as possible.
- Design an electrically small antenna with flat gain through the operating BW and a high front-to-back ratio.

Table of Contents

List of Figures

List of Tables

List of Abbreviations

AIS	Artificial Impedance Surface
AR	Axial Ratio
ARBW	Axial Ratio Bandwidth
AMC	Artificial Magnetic Conductor
BW	Bandwidth
CCL	Channel Capacity Loss
CP	Circular Polarisation
CPW	Coplanar Waveguide
DG	Diversity Gain
DNG	Double Negative
DPS	Double positive
DRA	Dielectric Resonator Antennas
ECC	Envelop Correlation Coefficient
EB	Exabytes
EM	Electromagnetic
EBG	Electromagnetic Bandgap
ENG	Epsilon Negative
EP	Elliptical Polarisation
FPC	Fabry-Perot Cavity
FCC	Federal Communications Commission
FSS	Frequency Selective Surfaces
FTBR	Front to Back Ratio

FWA	Fixed Wireless Access
HIS	High Impedance Surface
HPBW	Half Power Beam Width
IoT	Internet of Things
IoV	Internet of Vehicles
LP	Linear Polarisation
MMTs	Metamaterials
MSs	Metasurfaces
MSA	Microstrip Antennas
mm-Waves	Millimetre Waves
MNG	Mu Negative
MNZ	Mu Near Zero
MVDDS	Multichannel Video Distribution and Data Service
NL	Neutralising line
NRW	Nicolson-Ross-Weir
NRIM	Negative Refractive Index Material
NLOS	Non line-of-sight
PRS	Partially Reflective Surface
PRMS	Partially Reflective Metasurface
PEC	Perfect Electric Conductor
PGMS	Phase-Gradient MS
PMC	Perfect Magnetic Conductor
PBG	Photonic Band Gap

p2p	Point-to-Point
RI	Refractive Index
SISO	Single Input and Single Output
SINR	Signal to Interference to Noise Ratio
SNR	Signal to Noise Ratio
SNG	Single Negative
SRR	Split Ring Resonator
TARC	Total Active Reflection Coefficient
TVWS	TV White Space
UC	Unit Cell
UWB	Ultrawide band
VNA	Vector Network Analyser
ZIM	Zero Index Material
4G	4th Generation
5G	5th Generation

List of Symbols

c	Speed of Light
ε_r	Relative Permittivity
μ_r	Relative Permeability
Tan (δ)	Loss Tangent
λ_o	Free space wavelength
η	Efficiency
Γ	Reflection Coefficient
ω	Angular frequency
β	Phase Constant
k	Wave Number
f	Focal Distance
D	Large Dimension of Antenna

47

CHAPTER 1

INTRODUCTION

1.1 Background

As technology advances, the need for internet connectivity is exploding. Cisco reported that in 2021, 58% of the global population were internet users compared to 44% in 2016. Mobile devices and internet connections were 2.3 billion, which rose to 3.5 billion in 2021 [1]. In November 2020, Ericsson reported data traffic at a global level of 65 Exabytes (EB) per month, excluding the Fixed Wireless Access (FWA) point, by the end of 2021 [2]. Ericsson also reports post *pandemic COVID-19*, India's dependency on telecom networks increased to satisfy its business and personal needs [2]. In 2021, India recorded the highest growth in mobile broadband, with an average data consumption of 17 GB per month per user. Nokia reports that India's 4th Generation (4G) network carries all data traffic [3].

Fig 1.1: Multiple Wireless Communication devices installed with Microstrip Patch Antennas.

All this global data traffic is carried by a 4G network only. To which mm-wave technology in a *high-band* and *mid-band* is a solution for tackling multiple device traffic because of its inherent large bandwidths (BW), this Generation of wireless communication is called the 5th Generation (5G). The Federal Communication Commission (FCC) defined mm-wave spectrum at 24 GHz and above for 5G communication, Internet of Things (IoT), advanced spectrum-based services, and Satellite broadband services. The FCC allotted 24 GHz band (24.75 GHz to 25.25 GHz), 28 GHz band (27.5GHz to 28.35 GHz), 37 GHz band (37.6 GHz to 38.6 GHz), 39 GHz (38.6 GHz

19

14

to 40 GHz), 39 GHz band (38.6 GHz- 40 GHz), 47 GHz (47.2 GHz to 48.2 GHz) and 50 GHz band (50.4 GHz to 52.6 GHz). Also, the 64 GHz to 71 GHz band [4], [5]. The FCC has also proposed to expand the 70/80/90 GHz band for 5G communication [6]. The mm-Waves are defined from 24 GHz to 100 GHz. In March 2021, the FCC opened a *mid-band* 100 MHz (3.45 GHz to 3.55 GHz) of the band for 5G communication in a shared spectrum of 3.1 GHz to 3.55 GHz, which is part of federal and non-federal radio services [7], [8]. Prior to this expansion, the FCC allotted 500 MHz of bandwidth from 3.7GHz to 4.2 GHz for mobile 5G communication as a licensed spectrum [9]. All these *high* and *mid* bands will help serve as the solution to the surge demand for high data rates in mobile/cellular wireless communication systems. But are cellular/ mobile devices the only reason for internet traffic? *No*.

Every day, multiple devices are connected to the internet, such as smartphones, smart watches, smart speakers (*Google Home* and *Amazon Echo*), tablets, computers, VRs, etc., through *WiFi,* as shown in Fig. 1.1. Apparently, mobile data is not the epitome of internet/data traffic. The multiple devices, as mentioned earlier, use WiFi, which provides low-cost wireless connectivity to consumers across the globe, and are also responsible for high data rates. The demand for wireless connectivity is growing continuously. Since the *Pandemic* (*COVID-19*), this need cannot be *unseen*. The FCC in 2020 reported Cisco had projected a doubling in data traffic between 2019 and 2022. Also, most mobile data traffic is delivered through unlicensed wireless protocols such as *WiFi*, Bluetooth, etc. [10].

1.2 New Frequencies

To meet this demand, different unlicensed frequencies are being studied, expanded or utilised. The solution to these issues, while maintaining good wave propagation, is the following set of frequencies, which can be considered as a substitute/along with current WiFi services, i.e., 2.45 GHz and Sub 6 GHz band.

1. TV White Space (*TVWS*) band (470 MHz to 890 MHz) [11].

2. Ultrawide band (UWB) (3.1 GHz to 10.6 GHz) [12].

3. *WiFi-6E* (5.925 GHz to 7.125 GHz) [10].

4. Multichannel Video Distribution and Data Service (*MVDDS*) band (12.2 GHz to 12.7 GHz) [13].

5. Millimetre Waves (*mm-Waves*) (24 GHz to 100 GHz) [4], [5] and [6].

Out of the mentioned frequencies, TVWS, WiFi-6E, UWB, and mm-Waves are unlicensed frequencies, while MVDDS is a licensed band which is currently being explored. Multiple devices use wireless communication using unlicensed frequencies. Thus, it makes communication devices inexpensive for consumers. Using a licensed MVDDS band for the same purpose makes communication between devices with no congestion and efficient, but expensive for wireless communication devices [10], [13],

[14]. Now that the FCC has expanded the spectrum, hopefully, it will satisfy our needs for the BW crunch in the coming years. To serve these frequencies, Microstrip Antennas (MSAs) are best suited. As they have simple yet effective geometry, which offers advantages such as compact designs, low volume, light weight, easy fabrication, and easy integration with compact planar devices [15].

1.3 Microstrip Antennas

The MSAs were studied and practically developed around the 1970s. Since then, extensive research and analysis have been carried out for the development of MSAs. The common features of MSA are:

(a) A dielectric substrate (ε_r) layer sandwiched between two thin copper layers.

(b) The top region has a small amount of copper layer, often called a *Patch*.

(c) The bottom region copper layer is much larger than the patch is called a *Ground plane*.

(d) Power is applied through a *feed* to the patch.

A typical structure of MSA is shown in Fig. 1.2. The patch length is about 1/3 λ_o to 1/2 λ_o (where λ_o is a free space wavelength), which corresponds to the resonating frequency. The thickness of the dielectric constant varies from 0.001 λ_o to 0.005 λ_o. A dielectric constant closer to unity (i.e. of *air*) will result in high efficiency (η) and large BW, and a material with a high dielectric constant will result in low efficiency and narrow BW. With these properties, MSA can be low profile, conformal and robust. MSAs are versatile in producing a wide variety of radiation patterns and polarisation depending upon the excited mode and shape of the patch. The MSA performance is based on the parameters, *Reflection Coefficient*, *Bandwidth*, *Radiation pattern*, *Directivity*, *Efficiency*, *Gain*, and *Polarisation.*

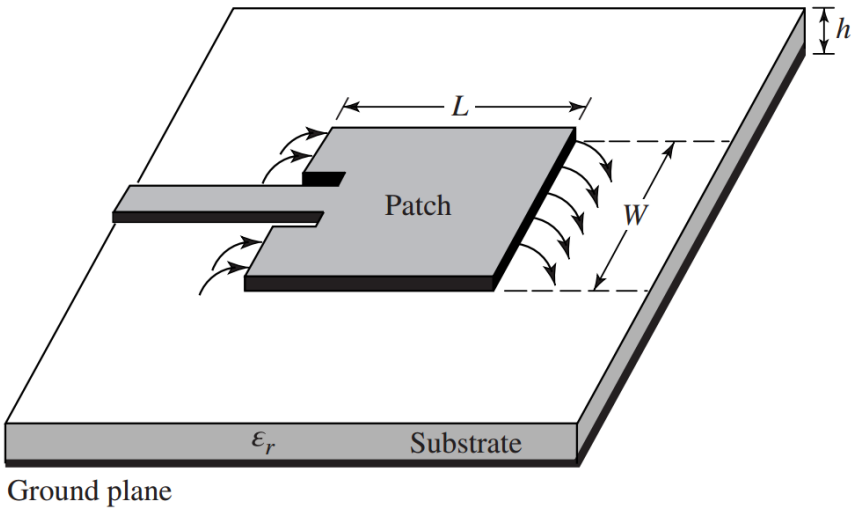

Fig. 1.2: Rectangular Microstrip Patch Antenna [15].

- *Reflection Coefficient*: The Reflection Coefficient is defined as the ratio of reflected power to incident power. If P_r is the reflected power and P_i is the incident power then the Reflection Coefficient (Γ) is given as

$$\Gamma = \frac{P_r}{P_i} = \frac{Z_L - Z_0}{Z_L + Z_0} \quad (1.1)$$

where

Z_L is load impedance and Z_o is characteristic impedance.

- *Bandwidth (BW):* It is defined as a range of frequencies in which antenna parameters are within the acceptable value of those at the centre frequency.

$$BW = f_H - f_L \quad (1.2)$$

where

f_H is the higher resonating frequency and f_L is the lower resonating frequency. Typically, Patch antennas offer 5 % to 10 % fractional BW, which is often low for high speed communication.

- *Radiation Pattern*: The graphical representation of radiation characteristics of the antenna as a function of space coordinates. Mostly, radiation pattern is determined in the Farfield, and it is also represented as a function of directional coordinates.

- *Radiation Intensity*: Power radiated by the antenna in a *given* direction per unit solid angle.

$$U = r^2 W_{rad} \quad (1.3)$$

where

U is radiation intensity (W/ unit solid angle)

W_{rad} is radiation density (W/m^2)

- *Radiation Density*: The total power radiated, which is uniformly distributed over the surface of a sphere of radius *r*.

$$W_{rad} = \frac{P_{rad}}{4\pi r^2} \quad (1.4)$$

- *Beam Width*: Beam Width, also known as Half Power Beam Width (HPBW), is the angle measured at one-half of the beam of maximum radiation intensity.

- *Directivity (D)*: The ratio of the radiation intensity in a given direction to radiation intensity averaged over all directions.

$$D = \frac{4\pi U}{P_{rad}} \quad (1.5)$$

- *Total Antenna Efficiency (η)*: The total antenna efficiency accounts for losses at input terminal, conductivity, and dielectric.

$$\eta = e_r e_c e_d \quad (1.6)$$

where
e_r is reflection efficiency (1-$|\Gamma^2|$)
e_c is conductivity loss
e_d is dielectric loss

- *Gain (G)*: It is the ratio of the radiation intensity in a given direction to the radiation intensity if power accepted by the antenna is radiated isotropically.

$$G = \eta D \quad (1.7)$$

- *Polarisation*: The property of electromagnetic (EM) waves describing the time-varying direction and relative extreme magnitude of the electric field vector; tracing a *figure* as a function of time at a fixed location in space as observed along the direction of wave propagation. The polarisations are classified as Linear, Elliptical and Circular polarisation.

  - Linear Polarisation: An electric field vector at any point in space as a function of time is always directed along the line; the field is said to be linearly polarised.

  - Elliptical Polarisation: If the tip of an electric field vector traces an ellipse in space as a function of time, then it is an elliptical polarisation.

  - Circular Polarisation: If the tip of an electric field vector traces a circle in space as a function of time, then it is circular polarisation.

1.4 MIMO Antennas

High data rates up to 1 Gbps can be attained with a Single Input and Single Output (SISO) antenna with sufficient BW and Modulation techniques as the transmitter and receiver. However, the SISO transceiver has several issues, such as low Signal to Noise ratio (SNR), which limits the spectral efficiency. For 5G communication, spectral efficiency requires a high number of bits to be transmitted per unit BW, measured in bits per second per Hertz (bits/sec/Hz). The transmit power for indoor communication is limited to 1 W, and outdoors it is 10 times higher. The SNR is limited to 30 dB to 35 dB because of complicated linear receivers with low phase error. The Signal to Interference to Noise ratio (SINR) is also limited because of co-channel interference. Low SINR means more users and more data, along with *capped* interference, leading to high spectral

efficiency. The average SINR lies between 10 dB and 20 dB, which means increasing spectral efficiency beyond 2-4 bits/sec/Hz is not possible for Non line-of-sight (NLOS). For a high data rate up to 1 Gbps, the SISO system will require 220 MHz BW, which reduces the communication range to 35 % of the reference system range. Because wide BW requires more power and resources, it reduces the effective coverage distance.

In contrast, the Multiple Input and Multiple Output (MIMO) system can reach up to 1 Gbps data rates using 20 MHz BW and a 10 × 10 antenna array. The reference range can be maintained up to 80 %. This shows, the MIMO system achieves high spectral efficiency and better coverage without increasing transmit power. The SNR is improved with no additional power. The performance improvement in the MIMO system is due to *Array Gain*, *Diversity Gain*, *Spatial Multiplexing Gain,* and *Interference reduction*. In the following, these properties are discussed:

- *Array Gain*: Array gain refers to the result of processing at the transmitter and receiver to increase the received SNR by the coherent combining effect of signals from different transmit or receive antennas.

- *Diversity Gain*: Diversity gain refers to the improvement in signal reliability achieved using multiple transmit and receive antennas to counter fading and channel impairment.

- *Spatial Multiplexing Gain*: The MIMO channels increase the capacity for no additional power or BW; this gain is referred to as Spatial Multiplexing Gain. This is realised by transmitting independent signals from individual antennas.

- *Interference Reduction*: In the MIMO system, spatial diversity is preferred over time/ frequency diversity. Multiple antennas for reception, the arriving signal from different directions has different spatial characteristics- angle of arrival, phase and amplitude. These signals are received by the antenna array, and co-channel signals are leveraged to reduce interference. This allows aggressive frequency reuse, thereby increasing multicell capacity.

1.5 Research Motivation

The Patch antennas are always used for wireless communication in various applications because they are compact, conformal, easy to fabricate, low-cost, etc. But patch antennas also have low efficiency, low gain, and narrow bandwidth, which are the major drawbacks [15], [16]. Most of the reported WiFi/ WiMax, Sub-6 GHz, and UWB antennas (Single and MIMO) suffer from low gain due to their unconventional design, partial ground plane and Defected Ground Structures (DGS) to accommodate wide impedance BW, which results in low directivity, bi-directional radiation, and low efficiency, often leads to a *poor gain* of the antenna [17], [18], [19], [20], [21], [22], [23], as shown in Fig. 1.3. The gain of these antennas varies between 0.5 dBi and 6 dBi, which

is unsuitable for point-to-point (p2p) 5G communication [24]. The gain and BW of the antenna can be *improved* by incorporating different techniques, such as an increase in the height of substrate, aperture coupling, proximity coupling, stacked layers, parasitic elements, Directors, Dielectric Resonator Antennas (DRA), and *Metamaterials* [25], [26], [27], [28], [29], [30], respectively.

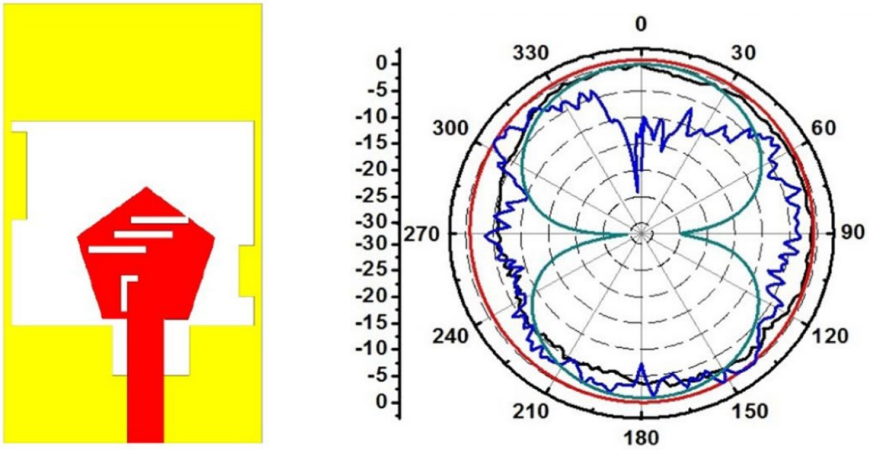

(a) (b)

Fig. 1.3: Bidirectional radiation pattern of DGS incorporated patch antenna (a) patch antenna & (b) bidirectional radiational pattern [19].

To counter the low gain, low directionality, and high side lobes for p2p communication, Array Antennas are effective due to their low profile. Arrays are usually used for scanning since they have a high directivity [15]. As the number of elements increases, the gain of the antenna array increases, but as the structures keep increasing, there are inevitable losses across the power dividers [31]. Not only, power dividers increase losses, but also the transmission line circuit gets complex with an increase in the number of elements, as seen in [32], [33], [34], [35], [36], [37]. In addition to this, as the number of elements increases, maintaining isolation between these elements gets difficult. Hence, design and analysis become complicated.

As the performance of MSAs is bound to their shape, size, and material used, i.e., dielectric constant (ε_r) and their thickness, to maintain low surface waves. This mostly affects the radiation characteristics, such as radiation patterns and gain. Also, BW and axial ratio (AR) BW are inherently narrow [38]. To overcome these limitations, *Metamaterials* (MMTs) can be integrated with the antennas to enhance their performance; due to their unique structures and EM waves manipulation properties. Which will significantly benefit p2p 5G communication. Therefore, MMTs are the centre of attraction for researchers around the *world*. The MMTs are engineered artificial materials; materials that show unnatural material properties, for instance, Double Negative (DNG) medium properties, Negative Permittivity ($\varepsilon_r < 0$), Negative Permeability ($\mu_r < 0$), and Negative Refractive Index (NRI) ($n < 0$) with a *negative phase* value [39], [40]. MMTs are

categorised into four types [41] which are Left Hand Materials, as shown in Table 1.1. The Artificial Magnetic Conductor (AMC), Electromagnetic Bandgap structure (EBG), and High Impedance Surface (HIS) are Artificial Impedance MMT structures which can be used as reflectors, isolators, decouplers, and to reduce surface waves, respectively. MMTs can be utilised as a *lens* to enhance the gain [42], *Absorbers* to absorb EM waves at the required [43], Beam splitters, to convert the polarisation of the source antenna, Polarisation converters [44], etc. An extensive survey on MMT is presented in [41], [45], [46], [47], [48], [49]; MMTs are used as gain enhancers, absorbers, and isolation enhancers for multiple-input multiple-output (MIMO) antennas. This indicates that MMTs are essential to enhance the antenna performance and are key to the future low-profile antennas for 5G communication.

Table 1.1: Categories of Metamaterial.

Sr. No.	Categories	Material Properties
1.	Negative Refractive Index Material (NRI/ NRIM)	The refractive index is negative at the required frequencies.
2.	Double Negative (DNG)	Both permittivity and permeability negative.
3.	Single Negative (SNG)	Either permittivity (ENG) or permeability is negative (MNG), and the other is positive.
4.	Zero Index Material (ZIM)	Both/ Either of permittivity or permeability are zero.
5.	Artificial Magnetic Conductor (AMC), Electromagnetic Bandgap structure (EBG), and High Impedance Surface (HIS)	AMC dual of a perfect electric conductor, EBG restricts wave propagation in the frequency band, and HIS suppress the Surface wave, which enhances the gain by reducing sidelobes.

1.6 Research Contribution

In this thesis, novel designs of the MMTs and MSs for the gain enhancement of the antenna are proposed for p2p 5G communication. The proposed MMTs and MSs are Wideband/ UWB to encompass a wide spectrum of resonating frequencies. The key contributions are as follows:

- Designed Sub 6 UWB GHz MIMO antenna with a high gain and high port isolation, which covered frequencies, Wifi/WiMax/Bluetooth, 3.5 GHz 5G, 5 GH 5G and Wifi-6E. The MIMO antenna was mounted on the Vehicle to verify its radiation characteristics for IoT/IoV applications.

- An MS is designed to enhance the gain and ARBW of the RHCP antenna for CubeSat applications. The compact profile of the MS incorporated antenna resulted in ARBW almost impedance BW with an enhanced gain. The symmetric MS structure can also work with an LHCP antenna to result in identical results as that of a gain enhanced RHCP antenna.

- Designed an MS to enhance the gain of the antenna with highly directive beams. Almost flat gain is achieved for the operating BW; while maintaining a low profile. The Axial beamwidths closely match the HPBW of directive beams. The symmetric MS resulted in a polarisation insensitive MS.

- An AMC with UWB phase BW is designed with a capacitive slot in it to enhance the gain of the UWB mm-Wave MIMO antenna. UWB AMC integrated MIMO antenna has high isolation and high gain for the impedance BW.

- Designed MMTs/ MSs for the electrically small size antennas resonating at mm-Wave frequencies to enhance their gain, which will be a flat gain for the operating BW with high FTBR.

1.7 Thesis Organisation

This thesis is titled **'Design and Analysis of Gain Enhanced Microstrip Antennas using Metamaterials for 5G Applications'**, comprising seven chapters that discuss the design and analysis of antennas embedded with MMTs/MSs for enhancing their performances in terms of directivity, gain, BW, and ARBW. The operating frequency range for these MMTs/MSs antennas is from 2 GHz to 40 GHz. The thesis is organised as follows:

- *Chapter 1: Introduction*

This chapter gives an insight into a general review of microstrip patch antennas. The performance parameters with their definition, advantages and disadvantages are briefly discussed. A light is also shed on MMTs/ MSs, the principle of working and their types. The limitations of patch antennas, such as low gain, narrow bandwidths, and low ARBW, can be overcome by utilising MMTs/MSs and their types are also discussed.

- *Chapter 2: Literature Review*

In this chapter, an in-depth characterisation of MMTs/MSs for various applications is presented. The resonant and non-resonant behaviour is explained through different models of SRR. The extraction of NRI, Negative Permittivity, and Negative Permeability using the NRW method. The MMTs, such as LHM and AIS, with their methodology, antenna, assembly, key findings and drawbacks are discussed extensively. Lastly, based on the study of different MMTs, the research gaps are identified and framed.

- *Chapter 3: Design and Analysis of Sub-6 GHz UWB Antenna for IoT Application*

The third chapter discusses the need for Sub-6 GHz and Wifi-6E frequencies for IoT/5G applications. The design and analysis of the dual band AMC and MIMO patch antenna are presented. The methodology to achieve high isolation by designing a decoupling circuit for the gain enhanced antenna is given. The performance of the gain enhanced MIMO antenna is also presented when the antenna is integrated on top of the vehicle. Lastly, the MIMO performance is verified through testing and compared with simulated results.

- *Chapter 4: Design of Partially Reflective Surfaces to enhance Gain and ARBW of the CP antenna*

For satellite communication, high gain CP antennas operating in the X-band (8 GHz to 12 GHz) are embedded with the satellites. This chapter is devoted to the development of MSs called Partially Reflective Surfaces to enhance the gain of the radiator RHCP antenna. The designed MSs are modified to enhance the ARBW of the radiator to match its impedance BW. A thorough analysis of the integration of the MS array onto the CP radiator and enhancing its ARBW is presented. Lastly, the same MS array is used to enhance the gain and ARBW of the LHCP antenna, which verifies the versatility of the designed MS array.

- *Chapter 5: Phase-Gradient MS Lens antenna for 12 GHz 5G communication*

For terrestrial 5G communication, the MVDDS band (12.2 GHz to 12.7 GHz) is used for its high speed video and data delivery. A polarisation insensitive MS is designed to attain a phase gradient of 180º with high transmission levels. How each MS cell introduces a time delay is calculated and discussed. These MSs in the form of a 15×15 array lead to gain enhancement. A CP antenna/radiator is used as a source to feed the lens, and how MS reacts to the CP waves is also presented.

- *Chapter 6: Gain enhanced UWB and Wide band mm-waves Antennas for 5G communication*

The mm-wave antennas are widely known for their inherent capacity to result in UWB or wide bands while keeping a small size with respect to the wavelength of the resonant frequency. However, mm-wave antennas also have inherent low gain and poor propagation. Therefore, different types of MSs, such as AMC, DNG, Phase gradient, and 3D meta-structures, are incorporated in the antenna design for its gain enhancement.

- *Chapter 7: Conclusion, Future Scope and Social Impact*

This chapter summarises the key findings and highlights the significance of the conducted research in the previous chapters, where different MMTs/MSs are designed and analysed to enhance the gain of the microstrip antennas. It outlines how these enhanced antennas in the future can be tested in the field for deployment. This chapter also gives insight, how these antennas can serve as the base station antennas in real-time and socio-economic impact.

Chapter 2

Literature Review

2.1 Introduction

As discussed in CHAPTER 1, Today, we are in desperate need of wideband and high gain antennas. Therefore, 5G, WiFi-6E, and mm-waves antennas with high gain are hot topics of research for compact devices. However, due to the need for wideband compact devices for wireless communication, antenna miniaturisation has severely affected gain. For example, a partial ground plane results in bidirectional radiation and gain fluctuation, as mentioned earlier. An *IEEE* Gain of the antenna is defined as *"The ratio of intensity, in a given direction, to the radiation intensity that would be obtained if power accepted by the antenna were radiated isotropically"* [15]. This means that gain is necessary for p2p communication with an extended range, to suppress the SNR, and to reduce interference from other signals [41].

2.2 Metamaterials and Their Types

The term *Metamaterials* is a composition of two letters, '*Meta*' and '*Materials*'. In Greek, it means *beyond*, and these materials are artificially developed materials which exhibit unnatural, extraordinary EM properties. When an EM wave is passed through the MMTs layer/slab, then EM wave properties such as phase, polarisation, intensity, direction, etc, can be modified easily. The MMT are also addressed as Metasurface (MS) in 2-dimensional or 2D form. MMTs are mainly divided into two types: Left Hand Materials and Artificial Impedance Surfaces. The types are discussed in the following sections.

2.2.1 Left Hand Materials

MMTs are artificially engineered materials with unique structures which exhibit unnatural EM properties. Unlike natural materials, which have positive permittivity ($0 < \varepsilon$) and permeability ($0 < \mu$), the MMTs have negative permittivity ($\varepsilon < 0$) and permeability ($\mu < 0$). Therefore, they are also known as Left Handed Materials (LHMs), as shown in Fig. 2.1. In general, with reference to constitutive parameters, permittivity and permeability *materials* can be classified into four categories:

- Positive ε and Positive μ are double positive (*DPS*) materials.
- Positive ε and Negative μ are *Mu* negative (*MNG*) materials.
- Negative ε and Positive μ are Epsilon negative (*ENG*) materials.
- Negative ε and Negative μ are double negative (*DNG*) materials.

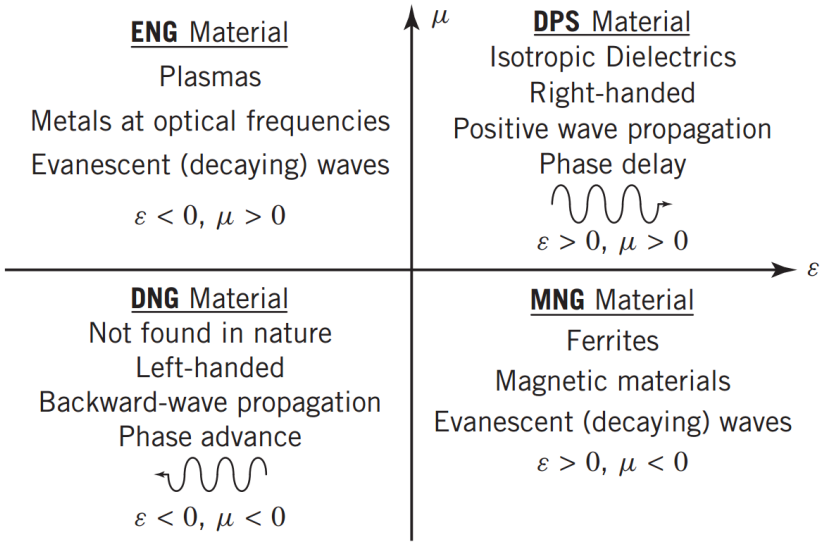

Fig. 2.1: Material classification as per their permittivity and permeability.

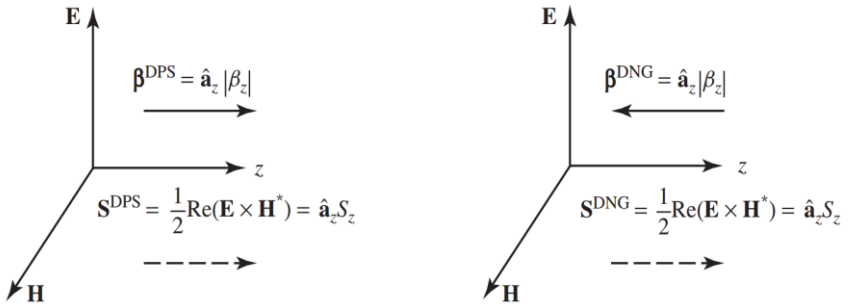

(a) (b)

Fig. 2.2: EM wave phase direction in (a) DPS medium and (b) DNG medium.

The materials shown in Fig. 2.1., the DPS are natural materials like air, quartz, water, etc., the MNG are magnetic materials, the ENG are plasma. Among these materials, DNG got special attention due to its double negative properties, which are not found naturally but can be realised artificially. When the EM wave is incident on the DNG slab/ layer, it was found that the EM wave propagating through the DNG layer has a direction of power density vector in the opposite direction to wave propagation, as shown in Fig. 2.2. Therefore, these materials are referred to as LHM or Backwards wave materials. In Fig. 2.2, the *dashed* line is the direction of wave propagation, while the *solid* line is the direction of the phase vector of EM wave. This results in antiparallel phase (*phase advancement*) and group velocity.

As the DNG material has negative permittivity and negative permeability, the refractive index (RI) widely noted as n, of the metamaterial can be calculated from Eqn. (2.1), therefore, DNG materials are also known as Negative Index Materials (NIM) [39].

$$n = \pm\sqrt{\varepsilon\mu} \qquad (2.1)$$

Snell's law of refraction, from Eqn. (2.2-a & b), suggests that when the refractive indices forming an interface are positive, i.e., both media are DPS, then the refracted (transmitted) wave will be on the same side of the reflected wave, as shown in Fig. 2.3 (a). However, when one medium has an NRI, then the refracted wave emerges on the same side of the incident/transmitted wave, as shown in Fig. 2.3 (b). The DNG materials with NRI, the phase constant (wave number) of the EM wave is negative and can be evaluated from Eqn. (2.3). This shows that, when the EM wave moves forward in time, there will be *phase advancement*, i.e., phase wavefronts are moving towards the source. Instead of a phase delay in the natural materials. Based on the above theory, DPS-DNG slabs or lenses are studied, which are also referred to as *Veselago Lenses.*

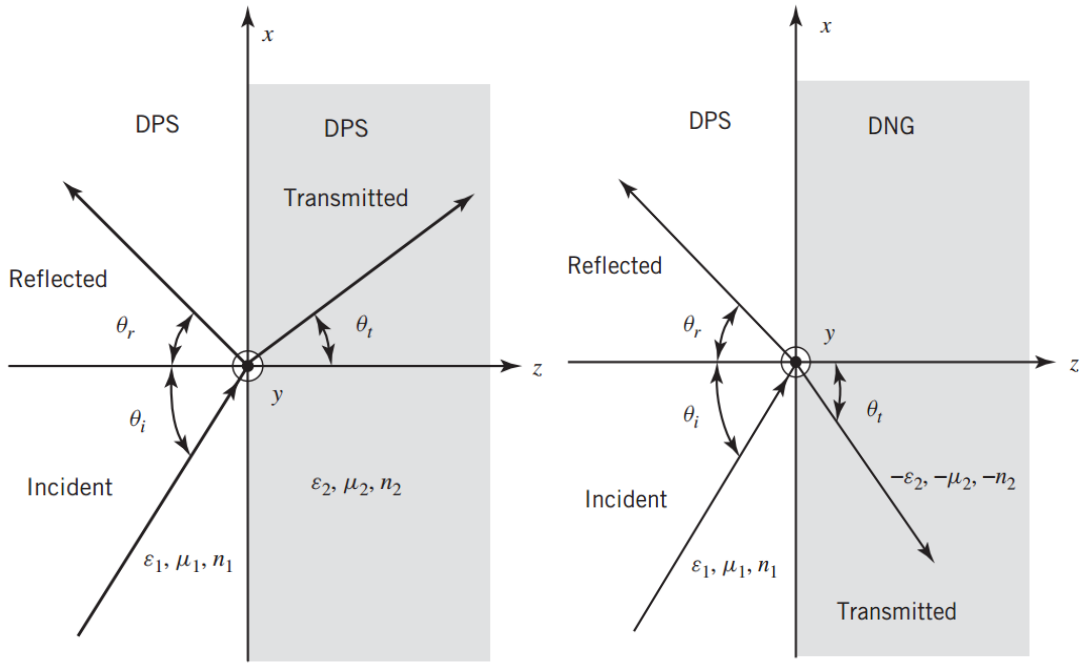

(a) (b)

Fig. 2.3: Wave refraction for (a) DPS-DPS media and (b) DPS-DNG [39].

$$\beta_1 sin\theta_i = \omega\sqrt{\varepsilon_1\mu_1}\, sin\theta_i \equiv \beta_2 sin\theta_t = \omega\sqrt{\varepsilon_2\mu_2}\, sin\theta_t \qquad (2.2\text{-a})$$

which can also be written as,

$$n_1 sin\theta_i = n_2 sin\theta_t \qquad (2.2\text{-b})$$

$$\beta_2 sin\theta_t = \omega\sqrt{\varepsilon_2\mu_2}\, sin\theta_t \qquad (2.3)$$

2.2.2 Artificial Impedance Surfaces

Artificial Impedance Surfaces (AIS), as the name suggests, are *engineered* structures to alter the impedance of the surface to control radiation characteristics, radiation efficiency and radiation pattern of the antenna. The Photonic Band Gap (PBG) structures are targeted at optical frequencies. They have the ability to restrict the propagation of a certain range of optical frequencies, creating a band gap. The PBG structures were extended into other structures to include other frequencies, such as Electromagnetic Band Gap (EBG) structure, High Impedance Structure (HIS), and Artificial Magnetic Conductors (AMC) [39], are subset of the Perfect Magnetic Conductor (PMC).

The surface waves affect the radiation characteristics, pattern and gain. The EBG structures operate similarly to PBG structures but at microwave frequencies; they suppress surface waves for a range of frequencies, creating a band gap for a low-profile MSA. However, EBG structures can only be made using vias to counter surface waves, which complicates the circuits. Also, the band gaps generated by the EBG structures have a narrow BW. The HIS structure does not require vias; they are planar structures with the patch and ground. When HIS is incident with planar waves, then it results in very high surface impedance (Z_s), this structure forms an *LC* circuit from which Z_s can be calculated from Eqn. (2.4) [50].

$$Z_s = j\omega L + \frac{1}{j\omega C} \tag{2.4}$$

where L is the inductance from the metal strips and C is the capacitance between the metal strips of the HIS structure.

Metal sheets are a Perfect Electric Conductor (PEC) found naturally, but a PMC is not. The reflection coefficient of the PEC is ($\Gamma = -1$) and its dual PMC has ($\Gamma = +1$). Therefore, reflected EM waves from the PEC has a 180º phase shift with an equal amplitude, which causes wave cancellation. Due to this, the radiation efficiency and gain decrease. The minimum distance between the antenna and a PEC reflector needs to be 1/2 λ_0 (where λ_0 is a free space wavelength). Such antenna arrangement is unsuitable for Spacecrafts, which will result in a high Radar Cross Section (RCS) or, in general, increase antenna profile with low efficiency. Contrary to PEC, PMC have 0º phase shift for a reflected EM wave. Therefore, firstly, PMCs are beneficial to counter the problem of low radiation efficiency. Secondly, as PMCs demonstrate high surface impedance, AMC are also capable of suppressing the surface wave,

The image currents of the PMC are *in-phase* with the original image currents. This property is leveraged to utilise the PMC as a reflector array and place the antenna in close proximity of the PMC array. It reduces the antenna profile from 1/2 λ_0 to 1/4 λ_0. The in-phase reflection is observed for the $+90^\circ$ to -90° of the reflection phase. The depiction of the PMC in-phase reflection is shown in Fig.2.4.

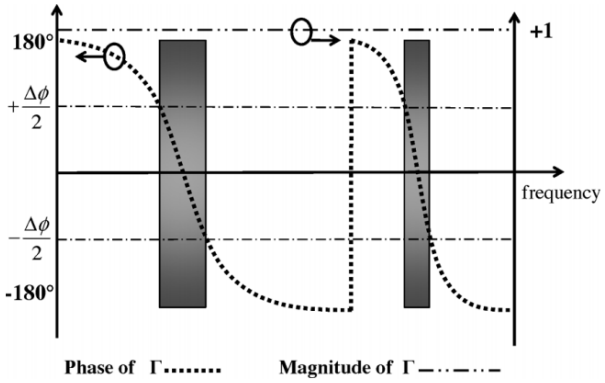

Fig. 2.4: In-phase reflection and reflection coefficient of the typical AMC unit cell [51].

2.3 Unit Cells and MMT Extraction

2.3.1 Unit Cells

The work established by Veseleago was further studied by *Pendry et al*, who suggested that artificial materials can be created by Periodic structures. *Smith et al* built the periodic structures, consisting of the *Unit Cells*, which exhibited DNG characteristics. It was achieved using concentric Split Rings with a thin metal strip structure etched on the dielectric substrate thickness ($d << \lambda$), which are confined to the size 1/10 λ_0 (where λ_0 corresponds to the resonating frequency) called as Unit Cell [52]. These structures are commonly known as Split Ring Resonator (SRR). An array of unit cells of SRR are shown in Fig. 2.5.

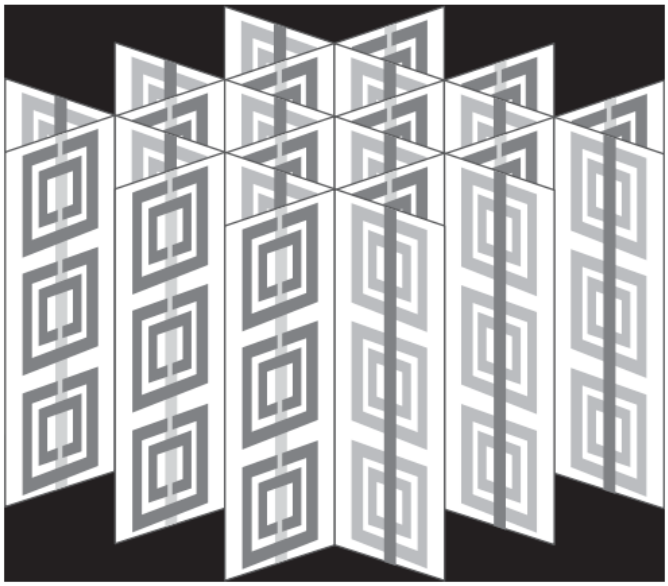

Fig. 2.5: Array of Split Ring Resonators with thin metal strip [39].

2.3.2 MMT Properties Extraction

Assuming the dielectric thickness of the MMT array is very small (d << λ). The Nicolson-Ross-Weir (NRW) method is widely used to extract Permittivity and Permeability. When the MMT unit cell is excited with EM waves. The S-parameters data retrieved from the simulation software or the Vector Network Analyser (VNA) is required. For further analysis, two constants are named V_1 and V_2.

$$V_1 = S_{12} + S_{11} \tag{2.5}$$

$$V_2 = S_{12} - S_{11} \tag{2.6}$$

Similarly, X and Y needs to be defined,

$$\mathrm{X} = \frac{1+V_1V_2}{V_1+V_2} = \frac{1+T^2}{2T} \tag{2.7}$$

$$\mathrm{Y} = \frac{1+V_1V_2}{V_1+V_2} = \frac{1+\Gamma^2}{2\Gamma} \tag{2.8}$$

Where, T and Γ are the transmission coefficient and reflection coefficient, respectively.

$$\mathrm{T} = \mathrm{X} \pm \sqrt{X^2 - 1} \tag{2.9}$$

$$\Gamma = \mathrm{Y} \pm \sqrt{Y^2 - 1} \tag{2.10}$$

The Z and Γ can also be written as,

$$Z = \frac{V_1-\Gamma}{1-V_1\Gamma} \tag{2.11}$$

$$\Gamma = \frac{Z-V_2}{1-ZV_2} \tag{2.12}$$

$$1 - Z = \frac{(1-V_1)(1+\Gamma)}{1-\Gamma V_1} \tag{2.13}$$

As the thickness of dielectric is very small and considering approximations, the permittivity and refractive index can be obtained from:

$$\varepsilon_r = \left(\frac{k}{k_O}\right)^2 \frac{1}{\mu_r} \tag{2.14}$$

$$n = \sqrt{\varepsilon_r \mu_r} = \frac{k}{k_o} \tag{2.15}$$

Here, $\varepsilon = \varepsilon_o \varepsilon_r$ and $\mu = \mu_o \mu_r$ the complex wave number given as $k = \omega \sqrt{\varepsilon_r \mu_r}/c = k_o \sqrt{\varepsilon_r \mu_r}$ and considering approximation $T \sim 1 - jkd$. The permitivity (ε_r) is calculated from,

$$\varepsilon \approx \mu_r + j \frac{2S_{11}}{k_o d} \tag{2.16}$$

The Eqn. (2.14), (2.15), and (2.16) can be used to extract MMT parameters.

In [53] a simple approach of NRW is presented to calculate ε_r & μ_r as follows,

$$\varepsilon_r \sim \frac{2}{jk_o d} \times \frac{1 - V_1}{1 + V_1} \tag{2.17}$$

$$\mu_r \sim \frac{2}{jk_o d} \times \frac{1 - V_2}{1 + V_2} \tag{2.18}$$

where $k_o = \frac{2\pi f}{c}$ and c is the speed of light (3×10^8 m/s) and the refractive index can be calculated using Eqn. (2.15).

Although MMT are primarily divided into two main types, DNG and AIS. However, they are not limited to them. A few examples are Zero Index Material (ZIM), Gradient Refractive Index (GRIN), Epsilon Near Zero (ENZ), Mu Near Zero (MNZ), Phase Gradience Metasurface (PGMS), etc. In further sections, different reported MMTs are discussed in detail.

2.4 Previous Work

A SRR structure is used to enhance the gain of a 2-element antenna array resonating at 5.8 GHz [54]. However, the BW of the MMT and antenna are narrow. A 2× 3 DNG lens is used in [55]. In [56] gain enhancement for the UWB antenna is achieved using resonant and non-resonant MMT cells over the frequency range 3 GHz to 14 GHz. The MMT unit cells have resonance from 9.8 GHz to 12.8 GHz. A 2×2 array of MMT unit cells placed in the same plane as the ground plane. However, the gain enhancement is found in the MMT resonance BW, and the gain variation is 6 dB as shown in Fig. 2.6. Similarly, A low-profile UWB antenna [57] incorporated with a dual layer of MMTs, have high gain variation from 6 dBi to 12 dBi. In [58] the DNG cells are incorporated with end-fire dipole antenna to enhance the gain. The DNG cells shown in Fig. 2.7 (a) are placed close to the radiator for gain enhancement. Also, an interesting point has been pointed out by the authors, as shown in Fig. 2.7 (b), that the reflection coefficient for the DNG cell should be well below -10 dB, and the transmission coefficient should be 0 dB throughout the mm-wave antenna's BW to improve the gain, i.e., it is working as resonating MMTs. The gain was enhanced by 3.5 dB for the resonating frequencies.

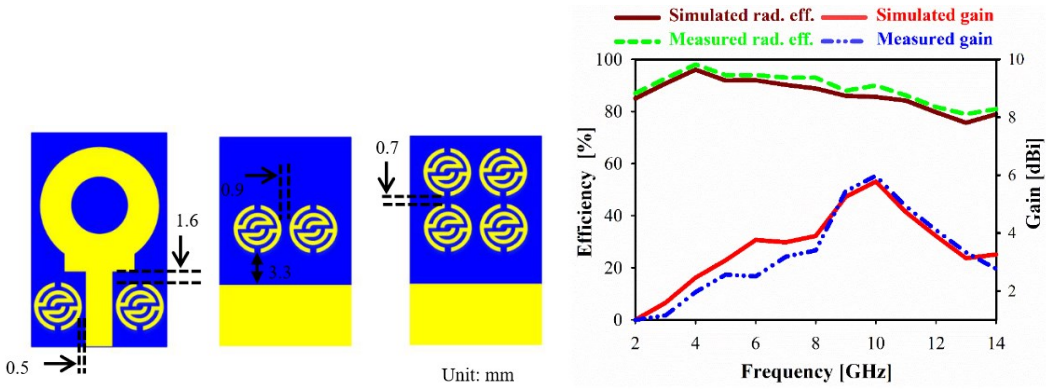

(a) (b)

Fig. 2.6: Reported UWB Antenna with MMTs (a) Antenna Structure, (g) Gain and Efficiency [56].

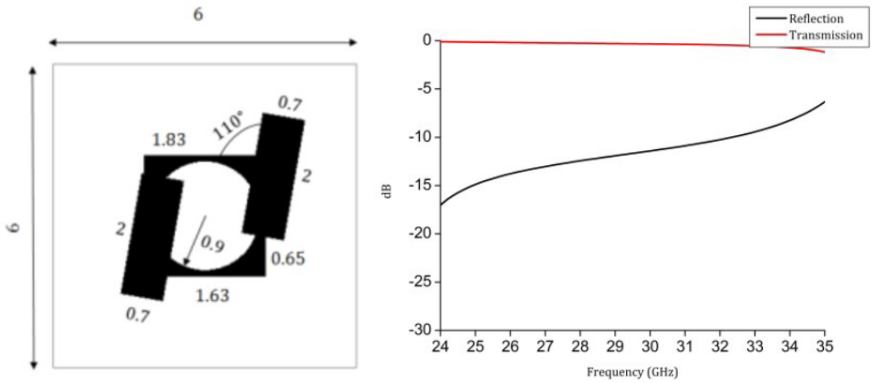

(a) (b)

Fig. 2.7: (a) Reported DNG cell, (b) Reflection and Transmission coefficient for DNG cell in [58].

A MMT lens is implemented in [59] to improve the gain of the inset patch antenna resonating at 12 GHz. An MMT structure with a NRI, negative permittivity and permeability was reported for operating BW. The two layers of MMT were stacked on the patch antenna at 10 mm. These two layers of MMT served as the lens, which helped to increase the gain by 71% more than the antenna without the lens. The gain was increased by 3 dB, which was also validated by measured results. In [42], the lens concept is reported where the MMT is addressed as NIM. The reported NIM structure has a NRI and negative permittivity and permeability, which also qualify as DNG. The NIM lens was kept on the top side of the antenna to enhance the gain of 8.55 dB in E-plane and 6.2 dB in H-plane at 10 GHz. In [60], three layers of MMT are referred to as the Superstrate. The designed MMT structure has near zero properties for permittivity, permeability, and reflection coefficient, well below -10 dB. The three layers on top of the antenna are shown in Fig. 2.8, increased the gain to 7.8 dB at 10 GHz which is 80% gain enhancement than

original patch antenna. This antenna has a very narrow band, and the size is large at 10 GHz. The extensive study for MMT with DNG properties or NRI is reported [61], [62], [63], [64], [65], [66]. In [67] MMT structures are used to deflect the beam away from broadside radiation to $\pm 38^{o}$. Non-resonant MMT structures were placed between two antennas. Here, S_{21} > -10 dB and S_{11}= 0 dB; therefore, the MMTs act as a reflector. The refractive index of the MMT is negative for the operating frequencies between 5 GHz and 5.5 GHz; hence, these MMTs are called NIM.

Although NIM or DNG materials result in unnatural EM properties, Materials with a refractive index value *zero* or close to zero also result in a similar way. The ZIMs' refractive index is between the values $-1< n < +1$; hence, they are named *Zero Index Materials* (ZIM) [68]. To enhance the gain, the Vivaldi antenna is integrated with ZIM unit cells in the aperture of the Vivaldi Antenna. As the EM energy flows through the ZIM, due to the geometric placement of the unit cell, EM energy is concentrated along the MMT, enhancing gain. A GRIN MMT in [69], i.e., the refractive index of the MMT, gradually increases with the increase in desired frequency range, as shown in Fig. 2.9. Therefore, these materials are called *Gradient Refractive Index* (GRIN) materials. The MMTs, either with negative Epsilon or negative Mu, also deliver similar EM characteristics to NIM. The negative Epsilon is obtained from the notches/ split rings in the patch of the unit cell are responsible for Capacitance, which may lead to negative permittivity [70]. On the other hand, thin metal strips lead to high Inductance and thus result in negative permeability [71]. The MMT structures, which yield a permittivity response close to zero, but *not* negative, also have promising results [72]. These MMTs are called *Epsilon Near Zero (ENZ)*. Similarly, MMT structures with a permeability value nearer to *Mu Near Zero(MNZ)* are utilised to enhance the gain of the patch antenna.

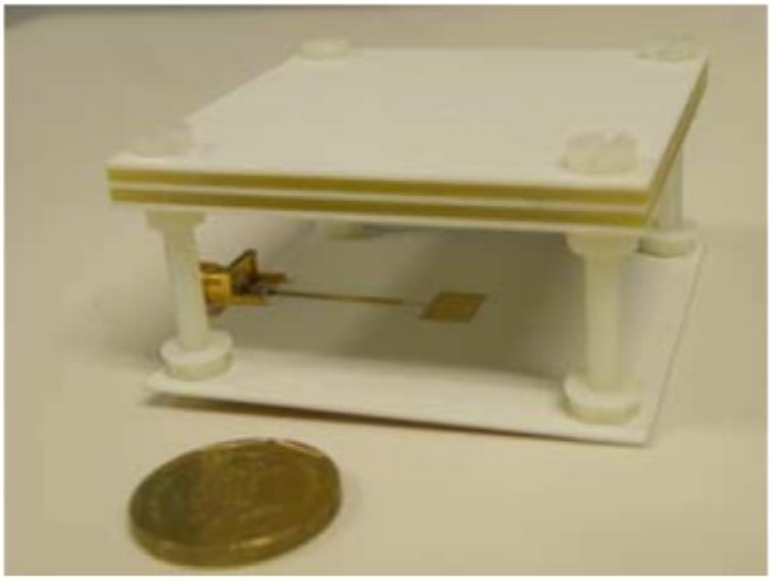

Fig. 2.8: Reported antenna integrated with NRI MMT in [60].

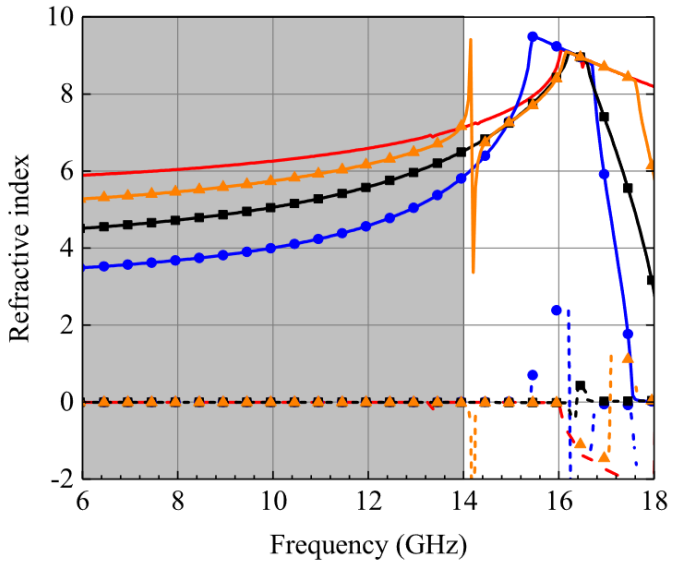

Fig. 2.9: Reported MMT have a Gradient Refractive Index in [69].

The MMTs have also gained the name Frequency Selective Surface (FSS) because MMT structures are bound to respond uniquely to the frequencies of interest. The FSS in [63] is used as a reflector to enhance the gain as the FSS unit cell has $S_{21} > -10$ dB. The gain-enhancing materials are placed at some distance from the patch. Due to this, antenna volume has become large. Also, these antennas have narrow BW with a low Front to Back ratio (FTBR). In [62], MMT is placed on top, at the height of 9 mm for the main patch, as shown in Figure 2.10. Though there is some gain enhancement, the antenna has poor FTBR, as shown in Figure 2.11.

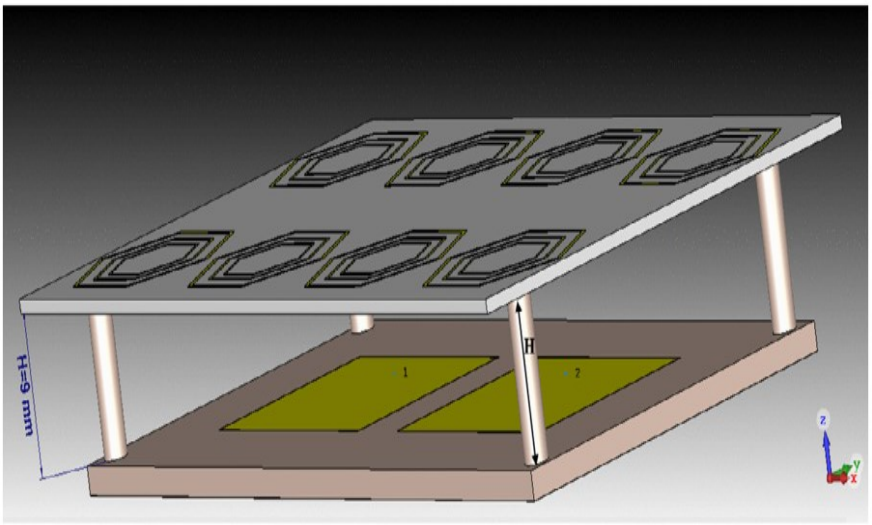

Figure 2.10: MMT for gain enhancement for MIMO antenna [62].

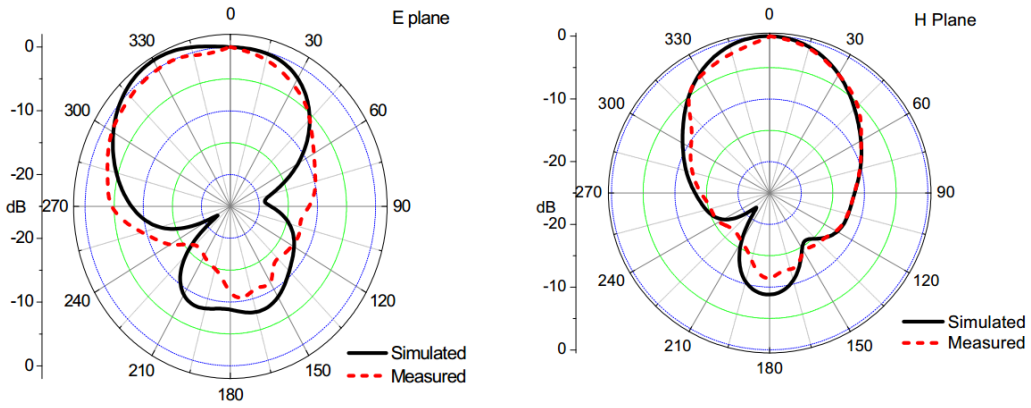

(a) (b)

Figure 2.11: Radiation pattern for MIMO antenna with a low FTBR, (a) E-plane, and (b) H-plane. [62]

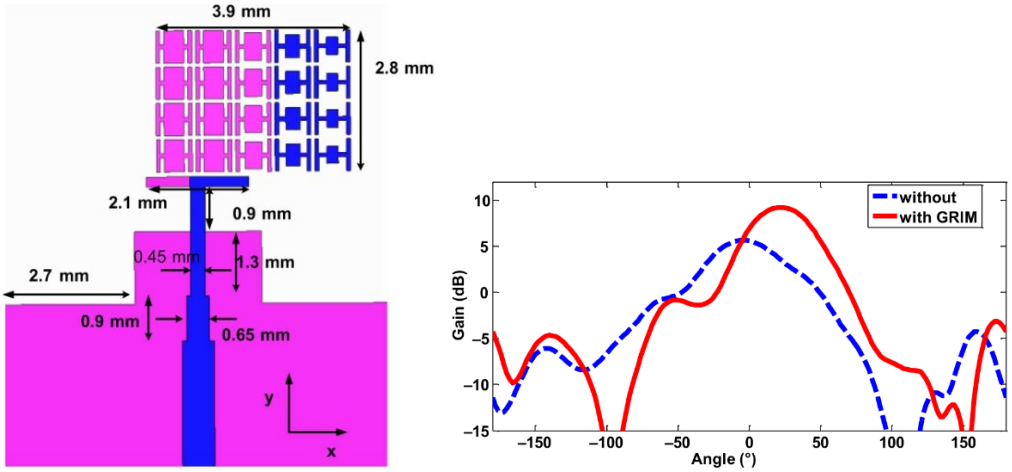

(a) (b)

Figure 2.12: (a) GRIM loaded antenna for beam deflection, (b) deflected beam in the E-plane at 60 GHz [73].

The research mentioned above has the gain enhancement, but with low FTBR or wide beamwidth and broadside radiation, which does not thoroughly serve the purpose of gain enhancement. Volume of the antenna is a constraint because of the requirement for compact circuits, as the MMT layer is placed on top of the antenna as a lens or superstrate at a height between *λ/4* and *λ/2*. The end-fire antennas with gain enhancement are studied. A UWB Vivaldi Antenna [68]. gain enhancement and beam deflection using different MMT arrays [73], [74]. The MMT unit cells are placed in the E-plane of the end-fire antenna to concentrate EM energy at 90º to enhance gain. The MMT cells can be modified to tilt the end-fire from 90º to the required angle, as shown in Fig. 2.12. As can be seen in Fig. 2.12, A Gradient Refractive Index Material (GRIM) is used to deflect the beam by

26º in E-plane and gain enhancement of 4 dBi for the end-fire antenna. The end-fire antennas include MIMO configuration with the gain enhancement; two-port dipole antennas are placed orthogonally to achieve high isolation and gain enhancement using ZIM [75]. This shows that a pattern diversity can be achieved along with gain enhancement. Although end-fire antennas have large BW and low profile, including gain enhancement techniques, for the long distance p2p communication, end-fire radiation is not always suitable in a wireless application. A broadside radiation with a narrow beamwidth and a minimum back-lobe is required in multiple base-station antennas.

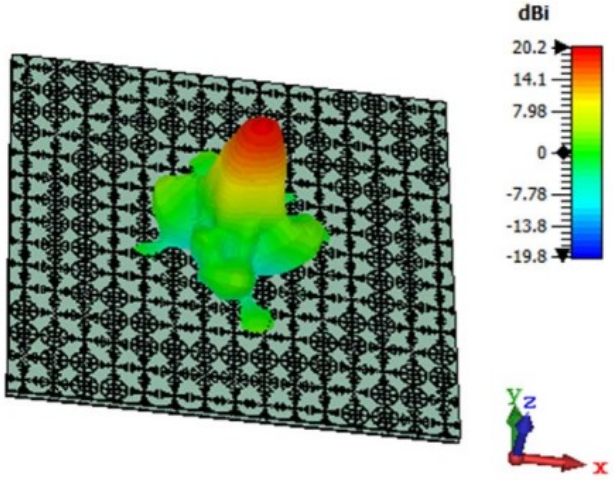

Figure 2.13: Phase Gradient Metasurface (PGMS) for gain enhancement [76].

In recent years, coded MMT has been used as a large M×N array (where M and N are the number of MMT unit cells) for obtaining a broadside high directivity called a *Lens*. These lenses are helpful for antennas (patch or horn antennas) to generate highly directional beams at microwave and mm-waves. These Lenses are placed at a focal distance *f* from the antenna to converge the wide beam radiation into a narrow directive beam, resulting in gain enhancement. These lenses can be transmissive or reflective; transmissive lenses have a high transmission coefficient (1 or 0 dB), while reflective lenses have low transmission levels (0.1 or -10 dB), widely known as a reflectarray. However, the working of these lenses is similar. The focal distance of the lens is calculated from Eqn. 2.19. On the surface of the lens, unit cells are placed to create a phase variation between unit cells to converge the beam in the broadside direction. These lens effectively works with mm-wave MIMO antennas, since the size of a single mm-wave antenna is very small. This way, wide-angle beam scanning is possible with massive MIMO [76]. In Fig. 2.13, the coded lens array is reported for gain enhancement up to 20 dBi.

$$\phi(r) = -\frac{\pi r^2}{\lambda f} \tag{2.19}$$

where ϕ(r) is phase shift between unit cells at a distant 'r' from the center unit cell.

Also, in [77], a coded metasurface lens is reported for gain enhancement along with different coded MMT structures. These coded MMT structures are not only used for gain enhancement but also to change the polarisation of emitted EM waves. In [78], a polarisation sensitive lens is reported, which acts as a transmit array and reflect array depending on whether the incident wave is x-polarised or y-polarised, respectively. The same concept of the lens array is also implemented in [79], [80], which increases the directivity of the antennas. A side lobe suppression using a metasurface is reported in [81]. One layer controls the amplitude, and the second layer controls the phase, which ultimately leads to low magnitude side lobes. A multi-layered polarisation converter transmitarray and reflectarray is reported in [82], as shown in Fig. 2.14. The 'H' shaped patch in three layers can convert x-polarised waves to y-polarised waves and vice versa.

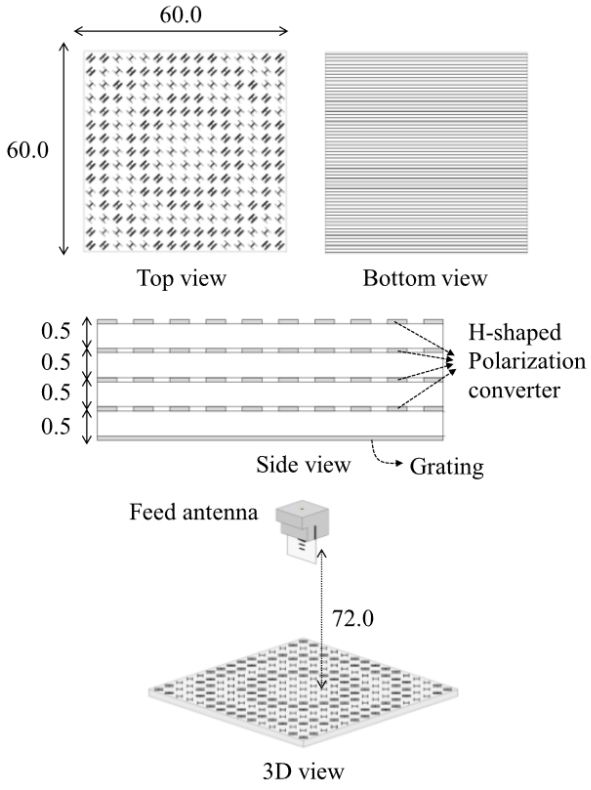

Fig. 2.14: Structure of the reported combinational transmitarray and reflectarray in [82].

The lenses are effective for the 5G base station as base stations are not restricted to a small size as compared to small wifi modules, which are confined to a small size and wide BW. The MMT lens at microwave frequencies are narrowband with a large size [83]. The wideband antennas with partial ground plane or DGS are preferred at microwave frequencies due to their compactness compared to antenna size at resonant length λ/2. However, the partial ground plane or DGS leads to high back lobes and side lobes.

The back lobe and side lobes suppression can be achieved by placing a reflector under the antenna for broadside radiation. This PEC reflector is kept at a distance of λ/4, but a regular PEC reflector gives in-phase and out-of-phase reflection for different wavelengths [50]. Due to this constructive and destructive interference of incident and reflected waves, results inconsistency in the radiation pattern. *What is a better reflector than a metal reflector?— PMC*. The PMC is used as a reflector to suppress the back lobes and sidelobes. PMC have the property of in-phase reflection between +90º and −90º because they have high impedance, ideally *infinite*, which prevents the formation of image current on the PMC surface [84]. This means the reflected waves have a phase difference of 0º for PMC; unlike PEC, the reflected waves have 180º with respect to the incident waves. Since PMC is duel of PEC, the reflection coefficient of PMC is 1 or 0 dB. Because of this property, a PMC reflector can be placed in very close proximity to the antenna, as shown in Fig. 2.15 [85]. The PMC does not exist naturally; they are engineered structures; as discussed earlier, they are also known as AIS. The PMC/ AIS exhibit some interesting properties, extremely high surface impedance, which does not allow surface currents. Thus, these structures are also called HIS. These structures restrict the propagation of specific frequencies, creating a bandgap for EM waves. Hence, the PMC is also known as EBG structures [84], [85] and lastly, AMC.

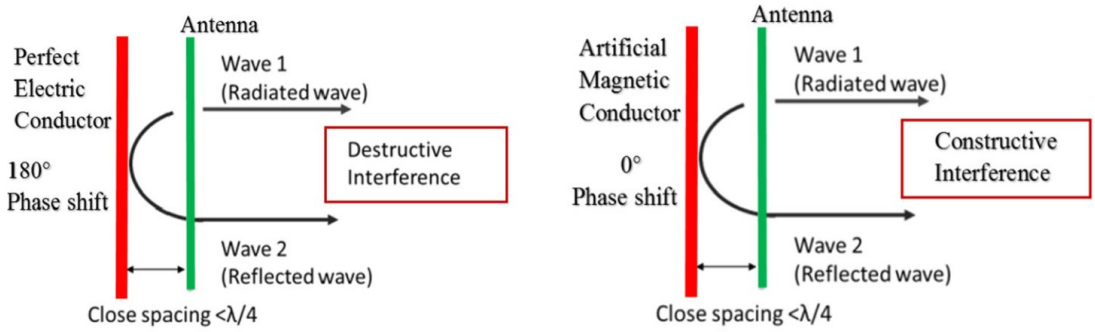

Fig. 2.15: Depiction of destructive and constructive interference for PEC and PMC reflectors, respectively [86].

The AMC reported in [87] have a linear reflection coefficient of 1 and reflection between +90º and −90º for 2.65GHz to 3.25GHz. The AMC acts as EBG in the given BW, thus reducing the size of the antenna. Although the height is only 1 mm between the antenna EBG array, the EBG BW is low, which leads to gain enhancement for narrow band antennas. A MIMO antenna resonating from 2 GHz to 4 GHz is reported in [88]. The maximum gain was achieved up to 10.8 dBi, but the total height and diameter of the antenna are 18 mm and 125.6 mm, as shown in Fig. 2.16. The AMC BW measured at ±90º is wide enough to result in gain enhancement without affecting the resonance of both antennas and the isolation between them. The structural symmetry of the reported AMC supports the x-polarised and y-polarised E-fields of both ports. A simple dipole antenna backed with an AMC reflector in [89] works at 2.4 GHz and 5.5 GHz and maximum gain of 7 dBi and 8 dBi, respectively. And the structure size is 12.5 × 120 mm².

As seen in Fig. 2.17, A similar dipole concept is implemented in [90] for MIMO with dual narrow bands at 2.4 GHz and 5.5 GHz. The structure size of 104 × 104 mm^2 and a height of 11 mm obtained a maximum gain of 7 dBi. Although both antenna structures have broadside antenna radiation, BW are narrow with large size structures.

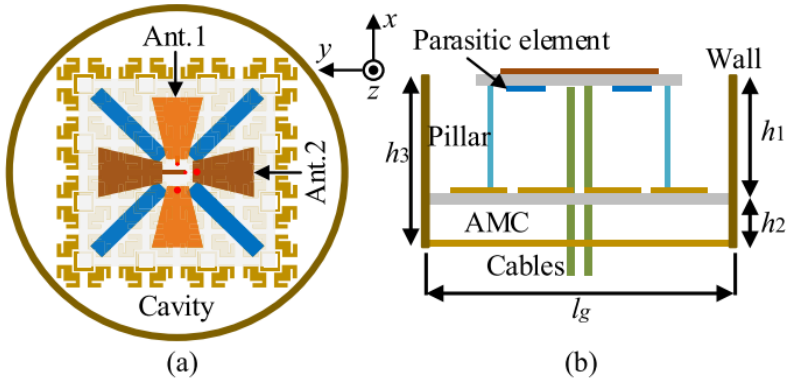

Fig. 2.16: Gain enhanced MIMO antenna (a) Top view, (b) Side view [88].

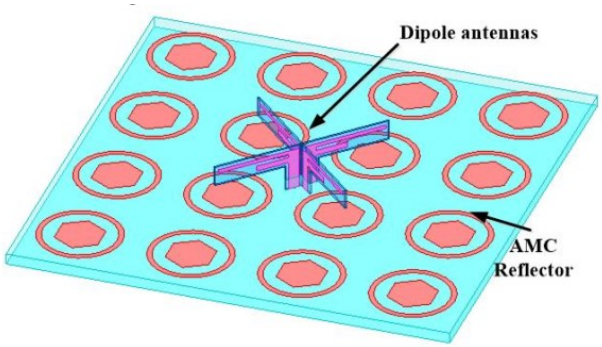

Fig. 2.17: Dipole MIMO antenna with AMC reflector [89].

Another dipole with a wide BW of 4.77 GHz to 7.12 GHz is reported with a height of 4 mm only between the antenna and AMC. The minimum and maximum gains are 8 dBi and 9.9 dBi, respectively [91]. This suggests a wide band antenna can have a low profile with high gain if AMC BW is equivalent to antenna impedance BW. The coupling between the antenna and the AMC reflector will affect the reflection coefficient as the height between the antenna and the AMC is reduced. For that antenna, parameters need to be adjusted to the right dimensions. The Wideband and UWB antennas with AMC are also reported in various research, but with the drawback of large spacing between the antenna and AMC. In [92], operating BW is from 4 GHz to 7 GHz, height between the Coplanar Waveguide (CPW) antenna and AMC is 28 mm, as shown in Fig. 2.18. The FTBR is poor with gain enhancement as shown in Fig. 2.19, because the spacing is too large, which leads to broad beamwidths with high sidelobes.

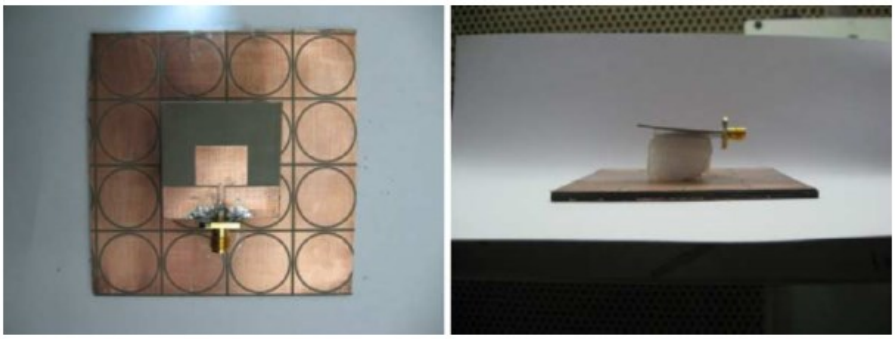

(a) (b)

Fig. 2.18: Reported CPW antenna with AMC reflector (a) Top view, (b) Side view [92].

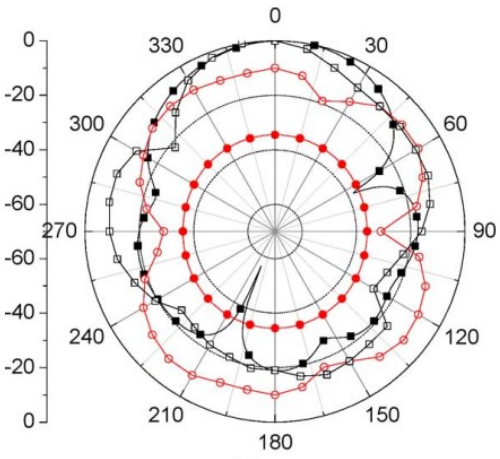

Fig. 2.19: E-plane radiation pattern of gain enhanced antenna at 4.45GHz [92].

The largest distance, 36.14 mm, between the antenna and FSS is reported in [93]. Also, the total size of FSS is 115 × 115 mm^2 as shown in Fig. 2.20. The antenna operates for the UWB range from 1.8 GHz to 15.2 GHz; as mentioned earlier, as the spacing between antenna and MMT reflector increases, it affects the FTBR and a gain variation is observed for the impedance BW. In [94], two Frequency Selective Surfaces (FSS) with a dielectric constant of 10.2 and a UWB CPW antenna operating from 2.5 GHz to 11 GHz are reported. But the height between CPW and both FSS is 22 mm, which does affect the FTBR of the antenna. Similarly, in [95], the FSS is kept at 17 mm under the UWB antenna, affecting the FTBR. The UWB antenna reported in [96] has a height of 10 mm below the antenna surface. In [97], an FSS layer is kept at 10 mm below the UWB CPW, but the radiation patterns are less directive. As the distance between the antenna and AMC is reduced, the antenna beams are more directive. Thus, stable ration patterns are obtained in the broadside direction. As suggested in [98], 6 mm is established between the antenna and AMC array with the size only 76 × 78 mm^2. The gain increased by 5 dB with a good

FTBR at 4 GHz, as shown in Fig. 2.21.A mm-wave MIMO antenna backed with an AMC at 4 mm from the antenna improved the gain by 55% [99].

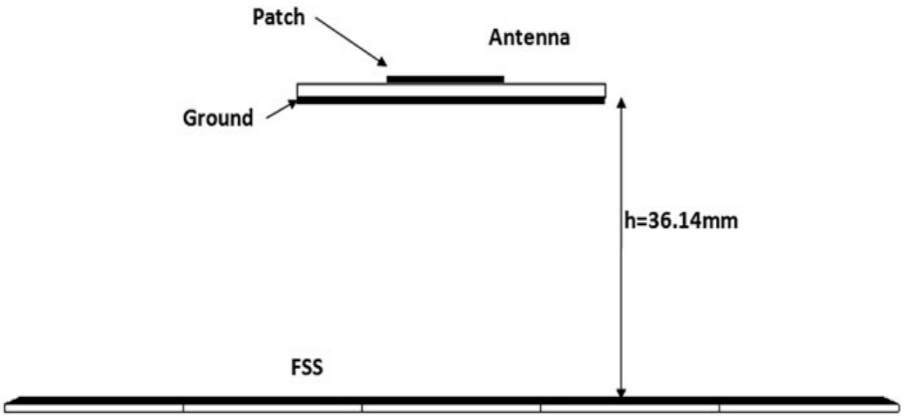

Fig. 2.20: UWB antenna with an FSS as a reflector in [100].

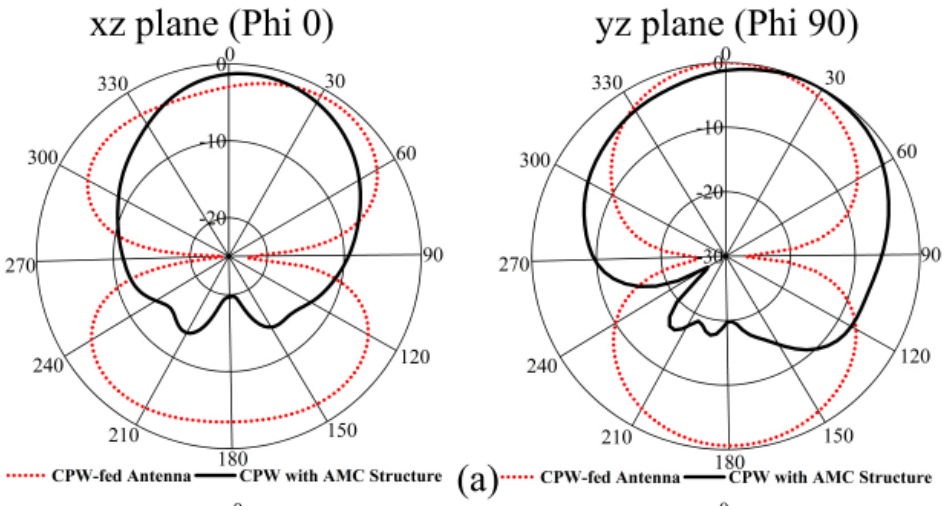

Fig. 2.21: CPW antenna radiation pattern without and with AMC [98].

Circular Polarisation (CP) is essential for transmission and reception effectively, as like polarised antennas will have an efficient signal strength and unlike polarised antennas will have no signals at the receiver. In the patch antennas, CP is obtained by exciting two orthogonal modes with a 90º phase difference between them. However, CP BW are usually narrow, i.e., 10 % of Impedance BW. The MMTs are advantageous to overcome the limitation of narrow CP BW. MMTs' structures can manipulate EM waves to convert their polarisation (LP to CP) and enhance the ARBW.

The Circularly Polarised Antennas (CPA) with gain enhancement are studied to improve the p2p communication. An AMC reflector is used to convert at RFID and WLAN frequencies [101]. With the use of the AMC reflector, substantial FTBR is achieved in the radiation patterns. The edges of the patch antenna are chamfered generate CP. Which is the simplest and effective method to obtain CP [102]. A 6 × 6 array for HIS is placed in the same plane as of patch to reduce surface waves. This also helped improve the BW for the mm-wave antenna, as shown in Fig. 2.22 [102]. The loading of HIS also improved the axial ratio BW of the antenna, obtaining a maximum gain of 11 dBi. A MIMO configuration can also be produced using this single antenna element. Since the HIS restrict surface waves from travelling, developed MIMO will have high port isolation. The high gain can be obtained with no inconsistency in the radiation patterns. This shows that with the use of PMC MMTs, impedance BW and ARBW can be enhanced.

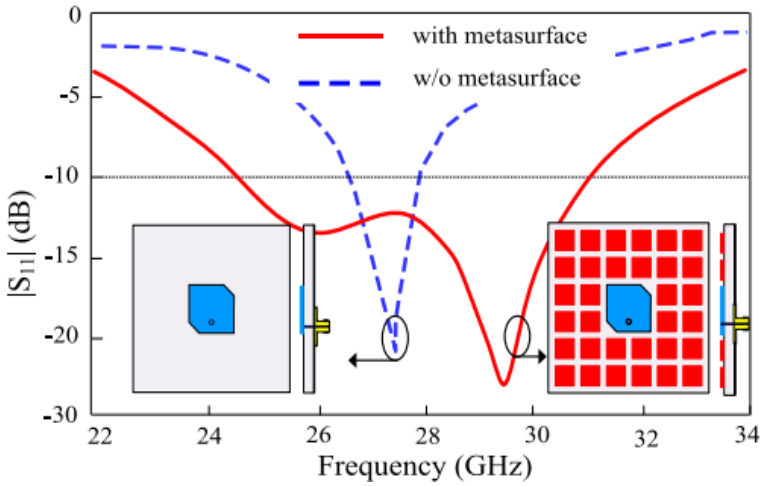

Fig. 2.22: Comparison of S11 for without and with HIS loading [102].

A Cross dipole antenna also produces CP when two orthogonal arms have equal admittance, and the angle of admittance differs by 90º [103]. A cross dipole antenna in [104] back with an AMC reflector just 1mm below, but it has very narrow axial bands at 2.4 GHz and 3.5 GHz. A metal cavity, as shown in Fig. 2.23, is used to enhance gain and achieve good FTBR. The cross dipole with parasitic elements enhances the antenna's BW and axial ratio BW. A maximum 10 dBi gain is reported, and an ARBW of almost 3 GHz [105]. Although a high gain and wide ARBW of 3 GHz is achieved, the fabrication of the antenna structure could be costly, and the carrying out of measurements would be difficult. Since different heights need to be maintained within the metal cavity. Hence, simple structures with effective output need to be explored. This reduces the cost of fabrication, minimises human error while assembling and testing antenna structure. It is important to obtain precise results in measurements which match the simulated results on the software.

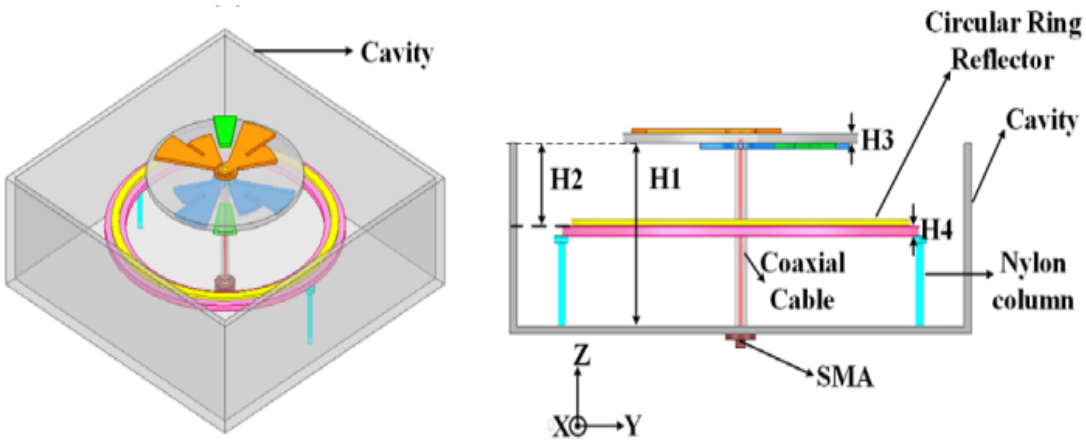

Fig. 2.23: Reported metal cavity back dipole antenna [105].

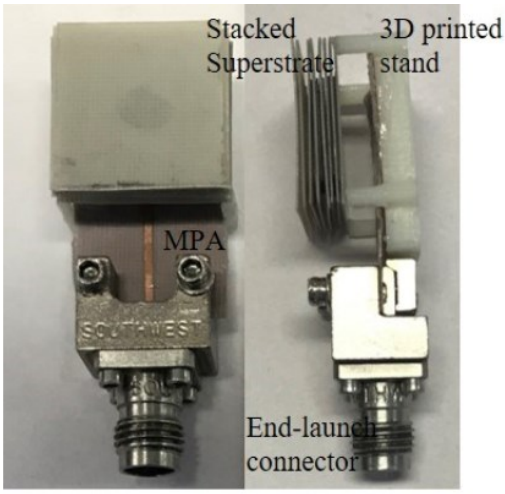

Fig. 2.24: A stacked substrate for gain enhancement onto a mm-wave antenna [66].

Substrates with different dielectric constants and heights are used for antenna fabrication. This substrate can also act as a superstrate by stacking multiple layers of the substrate on the radiator for gain enhancement [66], as shown in Fig. 2.24. The eight layers of Superstrate or substrate attained a gain enhancement of 4 dBi. In the past few decades of development, it has been found that a high dielectric constant dielectric material with different sizes and shapes acts as a *resonator*. These are known as *Dielectric Resonator Antennas (DRA).* DRA's are used to increase the gain of the antenna. A high dielectric constant material of different geometric shapes and sizes is placed on the feeding network, through which the dielectric material. This configuration gives a very high gain with a good FTBR [106], [107], [108], [109]. With these unique features of the DRA, 3D printed structures have their own advantages, such as easy and precise fabrication, cost efficiency, and most importantly, light-weight 3D structures can be printed as required with different

shapes and sizes, which emulate DRA properties. Apart from this, 3D printed structures have MMT properties to enhance gain [110], change polarisation from linear to circular [111], [112] and radome to minimise EM interference [113]. A 3D printed lens is used to enhance the gain of the mm-wave antenna as shown in Fig. 2.25. A 3D printed polariser enhanced the gain by 5 dB and converted linear polarisation to circular polarisation, the 3Dprinted polariser is shown in Fig. 2.26 [112].

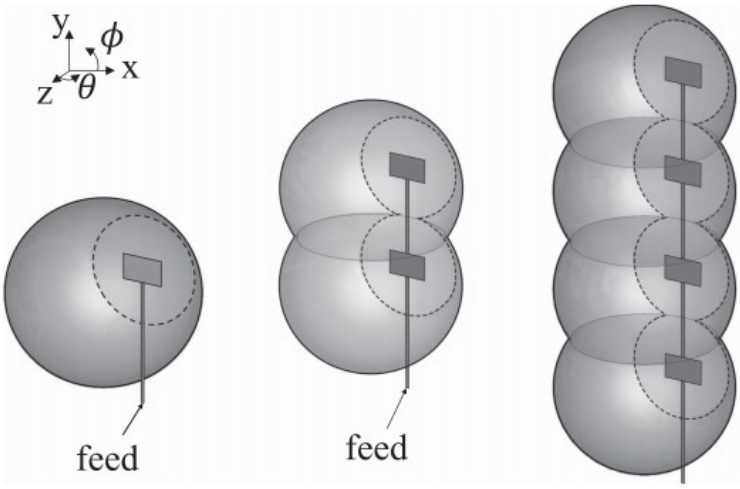

Fig. 2.25: Series-fed mm-wave with 3D printed lens for gain enhancement [110].

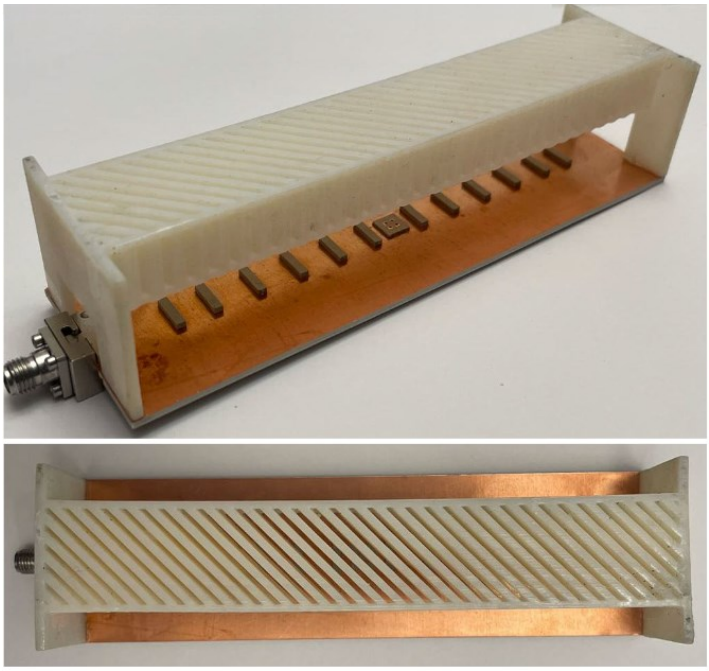

Fig. 2.26: Magnetoelectric antenna with 3D printed polariser [112].

2.5 Research Findings

The research findings on gain enhanced antennas using Left-Handed Materials MMTs are summarised in Table 2.1, and gain enhanced antennas using AIS MMTs are summarised in Table 2.2. The tables highlight the methodology for the gain enhancement of the patch antennas with key findings and drawbacks.

Table 2.1: Key findings and Drawbacks of different types of Left-Handed Materials integrated with patch antennas.

Ref.	Year	Antenna structure/ Methodology	Key findings/Drawbacks
[60]	2012	Negative RI MMT layers are placed on top of the antenna to enhance gain.	High gain enhancement is achieved. The MMT's thin metal and gaps between them act as an inductor and a capacitor, respectively.
[114]	2015	1×4 unit cells are used as a radiator and partial ground to obtain UWB.	Positive and Negative RI are obtained. However, high variation in RI and gain is observed.
[115]	2015	To generate multibands, SRR is utilised as a patch.	The SRR can be used to improve impedance matching at desired frequencies. However, narrow bands are obtained.
[116]	2016	Two EBGs are used to reject the WiMAX band (3.3-3.8 GHz).	EBG effectively adds a notch in resonance at 3.3-3.8 GHz. For the UWB the gain variation is more than 4 dB.

[117]	2017	Two SRR MMTs are used as a polarisation rotor to enhance isolation between MIMO ports.	SRR rotates the E-field orientation from Horizontal to Vertical and vice versa. This makes the polarisation of the MIMO antenna orthogonal, resulting in high isolation.
[118]	2017	2×2 parasitic MMT unit cells are used to reduce the antenna size and enhance impedance BW.	Composite right/left-handed material reduced the antenna size approx. by half, and the enhanced BW is six times that of a conventional antenna's BW.
[119]	2017	A non-uniform MMT array is used as a Superstrate. A non-uniform array results in a wide bandwidth.	High gain and wide BW of 2 GHz is achieved. The Superstrate is placed at a height of 1 mm from the patch antenna.
[120]	2017	High permittivity 10×25 MS array slabs are installed on the Vivaldi antenna for gain enhancement.	Gain enhancement for the UWB is achieved using dual MS slabs placed at the top and bottom of the Vivaldi antenna. This antenna-MS configuration increases antenna profile.
[121]	2018	Interdigital Capacitor (IDC) and SRR MMTs are loaded in the Coplanar Waveguide antenna to generate multibands and CP.	A combination of IDC and SRR generates generates multiband. However, the study of how CP is obtained is not presented.

[122]	2018	An MS array with truncated edges is used as a superstrate to enhance the gain and to obtain a wideband CP.	The L-shaped feed generated CP and MS enhanced the ARBW. However, enhanced gain varies more than 5 dB, and ARBW is around 30%.
[123]	2018	Wideband mm-wave MMT UC have a high RI between 1.9 and 2.1. The MMT UC are also used to tilt the beam of EM radiation of two offset ports.	The MMT UC is a capacitive-loaded loop, which generates a wide UC BW. The low variation in RI generates low gain variations. The beam tilting results in wide area scanning.
[62]	2019	An array of 2×4 MMT superstrate is used to enhance gain and isolation between the two ports.	The superstrate forms a Fabry-Perot cavity, which enhances the gain. Due to the low height of 9 mm between the antenna and the superstrate, coupling fields are restricted, increasing isolation.
[124]	2019	Non-periodic MS are used as radiating elements to widen impedance BW and high gain.	With a slight variation in the MS ring size, wide range of BW is obtained. As the Non-periodic MS array is excited, each MS BW in combination results in a wide impedance BW. It also increases the directivity, thus increasing gain.

[57]	2019	A dual-layer non-uniform MS acts as a wideband radiator excited by an aperture-coupled antenna.	Although a wideband is obtained through non-uniform MS, the gain variation is almost 5 dBi.
[75]	2019	ZIMs are placed in the aperture of the mm-wave MIMO dipole antenna to enhance the gain.	The ZIMs are dual polarised; therefore, Antenna polarisation remains unaffected. Therefore, gain enhancement is achieved for the 6 GHz impedance BW.
[80]	2020	A PGMS lens is used to enhance the gain of 8×8 dual polarised MIMO antennas. The ports are orthogonal	The phase gradience 305º with high transmission PGMS UC are designed to attain maximum enhanced gain of 22.4 dBi. The beam scanning is ±25º.
[125]	2020	An MS with a ring on the top and a complement of a ring on the bottom side of the MS acts as a partially reflective surface (PRS).	The 6×6 array of PRMS increases the gain of the aperture-coupled antenna. The MS partially reflects EM and results in constructive interference. However, enhanced has 8 dB of variation.
[126]	2020	High and low permittivity MS are designed and analysed. The stable E-field phase leads to gain enhancement.	As the frequency increase permittivity increases. Therefore, the MS is addressed as High and low permittivity MS.

[127]	2021	Two different GRIN MS are used as a lens to enhance the gain of the wide band antenna.	13 layers GRIN MS of are stacked and placed in front of end-fire radiation for gain enhancement. High and stable gain is obtained, Also, due to two metal plates and an MS lens, the design becomes a complex circuit to fabricate and assemble.
[81]	2021	Two MS lenses are incorporated with the MIMO antennas. MS-1 controls the amplitude, and MS-2 controls the phase of the EM waves. The combination of two lenses results in a focused beam.	The MS-1 reduces the side lobe levels, and the MS-2 focuses the beam at the centre of the lens. Maximum gain of 23.4 dBi and side lobes levels < -20.9 dB. However, the antenna assembly is very large.
[76]	2022	UWB PGMS is incorporated with the MIMO antenna for the gain enhancement.	High transmission in the PGMS UC can be obtained through an air gap between two layers of substrates in the UC. Symmetry in the UC will result in polarisation insensitivity.
[128]	2022	A Fabry-Perot cavity principle is used for gain enhancement, and a metal wall is installed to tilt the radiation beam.	maximum gain of 16 dBi is attained, and average gain is more than 10 dBi for the BW using PRMS and a metal reflector.

			However, the main radiator/ antenna is suspended between the PRMS layer and a metal reflector acting as a ground. This antenna combination is difficult to assemble and test due to its fragility.
[129]	2023	Beam steering is achieved through the reconfiguration technique using PIN diodes. The PGMS lens is used to enhance the gain.	To attain high aperture efficiency, antenna size must be restricted to a small size with high gain.
[130]	2023	MMT with a zero RI or ZIM are used to enhance the gain of the mm-wave substrate integrated waveguide (SIW) antenna.	When an EM wave travels from a material with n = 0 to a material with n =1, then the refracted EM wave reduces the EM phase variation to zero.
[110]	2024	A 3D printed dome lens is used for a series-fed array antenna.	Planar E-fields are obtained using a 3D printed dome lens, which resulted in constructive interference and high gain enhancement.
[131]	2024	High and stable permittivity MMT are added to Vivaldi to enhance the gain.	To maintain phase velocity across the aperture of the Vivaldi antenna, the number of MMT UCs is gradually decreased towards the outwards to increase gain.

Table 2.2: Key findings and Drawbacks of different types of AIS integrated with patch antennas.

Ref.	**Year**	**Antenna structure/ Methodology**	**Key findings/ Drawbacks**
[132]	2015	Wideband AMC is incorporated with wide dipole MIMO antenna for gain enhancement. Dipole antennas are placed orthogonally for high port isolation.	Thick AMC substrate results in high AMC BW. The dipole antenna and AMC structure have similar BWs; therefore, sufficient gain enhancement is attained.
[90]	2017	A 4×4 AMC array reflector is used to gain enhancement of the dipole MIMO antenna.	High enhanced gain is achieved while maintaining high isolation. This is done by matching the antenna and AMC BW. However the size of the AMC array is very large.
[133]	2019	An EGB reflector is used as a reflector for gain enhancement of the UWB mm-wave antenna array. The antenna also has a two-port MIMO configuration.	The array antennas have resonance from 22 GHz to 50 GHz and EBG structure has a narrow BW of approx. 2.5 GHz. Therefore, high gain variation more than 7 dB is observed i.e., 104×104 mm^2.
[134]	2020	AMC incorporated with a varactor diode is used as a reflector to enhance the gain	The distance between the antenna and the AMC array is only 2mm. However, AMC has a narrow BW; less

		and for frequency reconfiguration.	than 150 MHz. Impedance BW is also narrow. The frequency reconfiguration is achieved at the expense of impedance BW and matching.
[135]	2021	The wide band AMC reflector is utilised as a reflector for the gain enhancement of the wide band dipole patch antenna.	To attain a wide AMC BW, AMC thickness was increased from 3 mm to 8 mm along with a modified AMC patch with slots.
[109]	2022	A dual band AMC reflector is realised to enhance the gain of the DRA MIMO antenna.	Mainly gain enhancement is observed for frequencies ±90º. However, UWB gain enhancement is also because of the presence of the ground plane in the AMC reflector.
[136]	2022	An AIS with an LP to CP polarisation conversion property. The AIS also results in high gain.	Although a high gain of 5dBi is achieved with the low profile, the dual bands have narrow ARBW.
[137]	2024	Dual polarised dipole antennas with high isolation are placed onto the symmetric AMC array reflector for the gain enhancement.	Air gap of 17 mm between AMC patch and ground is maintained to result AMC BW of 3.5 GHz. Also metal wall cavity is added to structure for gain enhancement.

[138]	2024	A symmetrical polarisation insensitive AMC structure is used for gain enhancement of the CP antenna.	The cross dipole antenna structure with spiral arms results in CP at lower frequencies. To enhance the gain, a symmetrical AMC structure is utilised, which doesn't affect the polarisation of the CP antenna. However, ARBW of the antenna are narrow.

2.6 Limitations (Gaps) in the Reported MMT and Antenna Structures

With the extensive literature survey, it is found that the MMT structures, i.e., LHM and AIS, have emerged as a promising approach to enhance gain, change polarisation or enhance the impedance BW of the antenna. Although antennas with wide impedance BW and MMTs or MSs are embedded for enhancing or altering antenna performance, i.e., gain enhancement, ARBW enhancement, impedance BW enhancement, polarisation conversion, etc. While maintaining the compact antenna profile, which is crucial for the implementation of practical applications.

The limitations can be categorised as follows:

- Recently launched WiFi-6E, MVDDS and mm-Wave frequencies have not been explored with low profile gain enhanced and high FTBR antennas for the p2p communication.

- The Perfect Magnetic Conductors (PMCs) with a narrow phase have been studied extensively. However, PMCs with a wide or UWB phase need to be researched. When integrated with the antenna/radiator, the whole antenna needs to have a low or compact profile.

- Narrow and Wideband antennas with a high gain are investigated. However, the antenna structures have large volumes and polarisation-sensitive MMTs/MSs embedded in the antenna assembly. This makes MMTs/MS incompatible with different antenna structures.

- The reported circularly polarised antennas integrated with MMTs/MSs have narrow impedance BW and ARBW. In some wide band antennas, the ARBW is smaller than the impedance BW. Also, these antennas have large cavities or large reflectors for gain enhancement, which increases the antenna volume.

2.7 Research Objectives

In this thesis, different MMTs are designed to enhance the *gain* while maintaining a *low profile* of the MSAs to improve the p2p 5G communication. To accomplish it following research objectives are defined:

- **Research Objective 1:** Design antennas to cover newly defined frequencies by FCC *(WiFi-6E* and *MVDDS)* with an enhanced gain.

- **Research Objective 2:** Increase the axial BW of the CP antenna and increase the gain using MMT or a metal cavity, with a small structure.
- **Research Objective 3:** Design an antenna with gain enhancement for wide impedance BW, low profile and high directivity.

- **Research Objective 4:** To achieve enhanced gain enhancement for UWB antennas, maintaining antenna size as minimal as possible.

- **Research Objective 5:** Design an electrically small antenna with flat gain through the operating BW and a high front-to-back ratio.

2.8 Summary

The MMTs/ MSs structures, like LHM and AIS, have shown great potential in improving antenna performance by enhancing gain, bandwidth, and polarisation, limiting the compact antenna structures for practical application. However, challenges, such as the limited exploration of newer frequency bands like WiFi-6E, MVDDS, and mm-Wave with high gain, high FTBR antennas, and matching ARBW with the impedance BW while maintaining higher antenna gain, could be addressed with the design and analysis of the new MMT/MS structures, which will overcome these limitations being effective with promising results, design and fabrication friendly for ease of analysis and ease of measurements and most importantly cost effective. This approach will meet the demand and supply for high data rates of the p2p 5G communication.

Chapter 3

Design and Analysis of Sub-6 GHz UWB Antenna for IoT Application

3.1 Introduction

The demand for high data rates is increasing. Therefore, Sub-6 GHz 5G wireless communication frequencies, 3.5 GHz, 5.5 GHz and Wifi-6E are being integrated into a communication device [139]. Utilising this IoT has emerged to share data at high data rates between connected devices and with minimum human interference [140]. The Internet of Vehicles (IoV), which is a subset of IoT, is a modern-day evolving technology [141]. The vehicles are installed with communication devices to improve the Intravehicle and Intervehicle communication [142]. An overview of the IoT application is depicted in Fig. 3.1 (a), and Fig. 3.1 (b) depicts vehicles installed with the Vehicular Base Station (VBS) antennas to communicate with the wireless devices in their surroundings. Multiple different antennas in the recent past have been studied and analysed for IoT/IoV applications [143], [144], [145], [146]. In [143] and [144] Sub-6 GHz antennas have low gain; also, Sub-6 GHz 5G frequencies are not part of the operating frequencies. The multiband [145] and wideband [147] antennas have covered all required Sub-6 GHz frequencies. In [146] A reflectarray is used to enhance the gain; however, its structure is large, and a radome is difficult to integrate with the vehicle. To enhance the gain of the multiband antenna artificial magnetic conductor (AMC) reflector is used in [148] and [149] without MIMO configuration for vehicular communication. However, for higher data rates, wideband MIMO antennas are preferred over multiband antennas. This will result in minimum multipath fading and suppress interference. Therefore, MIMO antennas are key to 5G or IoT networks [150].

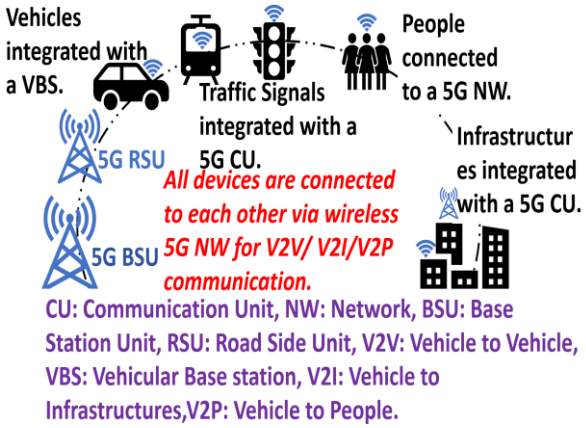

(a)

(b)

Fig. 3.1: (a) Overview of the IoT application, (b) VBS connected to each other and RSUs.

Multiple MIMO antennas without gain enhancement for IoV application are well in-depth investigated in [151], [152], [153]. To achieve high isolation, antennas are placed orthogonally with a shared aperture [151], π-shaped decoupling circuit for [152], Spatially separated antenna in [153]. However, employing these techniques, antenna structures have a large profile. Gain enhanced MIMO antennas are studied in [113], [154], [155], [156]. To enhance the gain of the Vivaldi MIMO antenna, an MS are embedded [113]; however, the gain enhancement is observed in higher frequencies and with the gain variation of 2.5 dB. For gain enhancement, an MS and EBG structures are utilised [154]. However, a 3 dB gain variation is observed due to the use of vias for high isolation. To improve the gain and isolation of the antenna, an MS is used[155]. The antennas have a high gain more than 8 dBi and an isolation higher than 20 dB, but BW less than 2 GHz in [156] and [157]. To enhance the gain, an AMC reflector is used, and a neutralising line (NL) serves as an isolation enhancer [109]. A symmetrical AMC reflector is used for the gain enhancement of a CP MIMO antenna operating at UHF and WLAN frequencies in [158].

Although many antenna structures mentioned above exhibit multiband characteristics, wideband and UWB performance, high gain, and good isolation, most of them have complex designs and relatively large profiles. Antennas with large profiles require considerable space, making their integration into vehicles as VBS challenging. Moreover, the existing IoT/IoV antennas do not cover Sub-6 GHz 5G frequency bands.

To overcome the limitations mentioned above, a MIMO antenna which covers multiple communication standards, such as Wifi / WiMax / Bluetooth / LTE frequency, Mid-band, 5 GHz band and Wifi-6E (5.9 GHz - 7.2 GHz) and downlink satcom band

(7.36 GHz - 8.06 GHz) is designed and investigated in this chapter. A 5 × 8 Dual Ring Dual Band (DRDB) AMC array is embedded with the MIMO antenna structure for gain enhancement. The gain is enhanced from 3.7 dBi to 5.1 dBi, 3.2 dBi to 5.8 dBi, 4.2 dBi to 6.8 dBi, and 5.8 dBi to 7.1 dBi at the frequencies 2.5 GHz, 3.5 GHz, 5.5 GHz and 7.2 GHz, respectively. To achieve the isolation of more than 19.66 dB between MIMO ports, two 1 × 3 vertical AMC walls are placed between the ports, enabling space utilisation. The Sub-6 GHz UWB MIMO antenna for IoT/IoV applications has a profile of 0.39 λ_0 × 0.63 λ_0 × 0.14 λ_0 only. This makes the proposed antenna compact, and its IoT/IoV application is verified by placing the proposed MIMO antenna on a vehicle through the simulations.

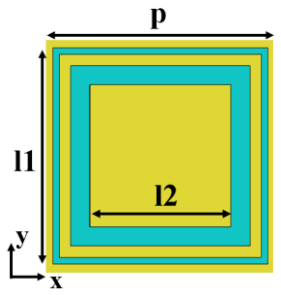

(a)

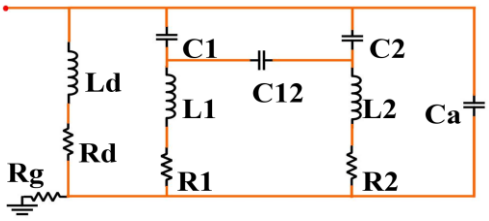

(b)

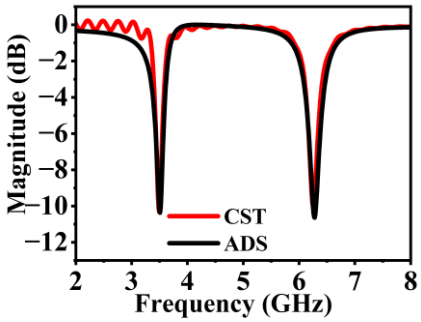

(c)

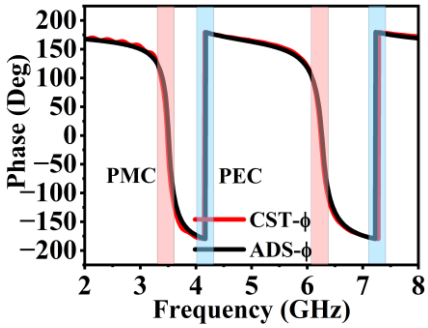

(d)

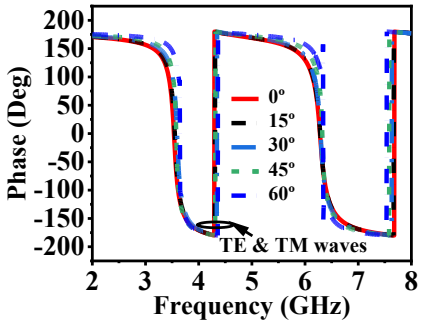

(e)

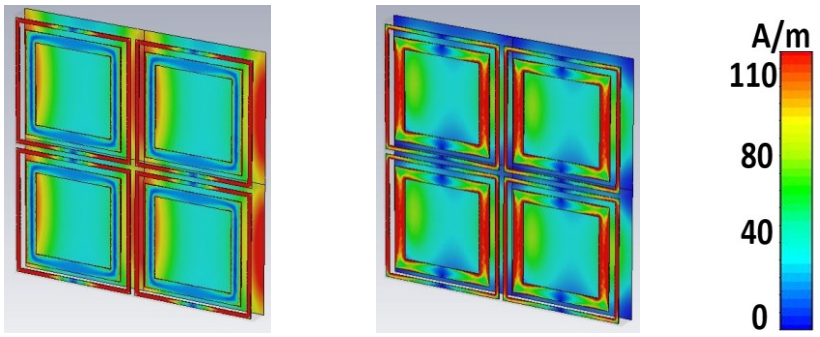

(f) (g)

Fig. 3.2: (a) Proposed AMC, (b) Equivalent circuit, (c) Magnitude, (d) Phase, (e) Study of different angles of incidences, (f) Surface current distribution at 3.5 GHz, and (g) Surface current distribution at 6.3 GHz. (Here, p = 10, l1 = 9.6, l2 = 8, outer-width = 0.3, inner-width = 0.85, hs1 = 1.55 all dimensions are in mm, ε_r = 4.4, Ld = 0.37 nH, L1 = 0.77 nH, L2 = 1.12 nH, Rd=0.7 Ω, R1 = 0.76 Ω, R2 = 0.001 Ω, Rg = 0.0025 Ω, C1 = 0.63 pF, C12 = 0.15 pF, C2 = 1.3 pF, Ca = 0.2 pF).

3.2 Design of DRDB AMC UC and Two Port MIMO Antenna

The proposed DRDB-AMC UC and its equivalent circuit (EC) are shown in Fig. 3.2 (a) & (b), respectively. The boundary conditions are applied in the x-direction and y-direction as PEC and PMC, respectively, and the UC is excited from the z-direction. The thin outer ring is responsible for the resonance at 3.5 GHz, and the thick inner ring is responsible for the resonance at 6.3 GHz, as shown in Fig. 3.2 (c). These dual resonances create two PMC and two PEC bands in its de-embedded phase. Two PMC bands are observed at 3.5 GHz and 6.3 GHz, respectively and two PEC bands, 4.25 GHz & 7.7 GHz, as shown in Fig. 3.2 (d). The PMC bands phase is measured at ± 90º from 3.45 GHz to 3.6 GHz and 6.1 GHz to 6.3 GHz, respectively. A sharp 180º phase reversal will be observed at PEC bands 4.29 GHz and 7.68 GHz, but the magnitude will remain the same. These found bands of DRDB-AMC UC are in the desired operating frequency range of 2 GHz to 7 GHz of Sub-6 GHz 5G communication. Different angles of incidence are studied to verify DRDB-AMC UC stability, as shown in Fig. 3.2 (e). The incidence angle (θ) is varied from 0º to 60º, and it is observed that the proposed AMC has stability up to 45º of angle of incidence. As the proposed AMC is symmetric in the x-direction and the y-direction, the incident transverse electric (TE) waves and transverse magnetic (TM) waves will generate identical phase responses, as shown in Fig. 3.2 (e).

The outer ring constitutes a high surface current distribution at 3.5 GHz, verifying its resonance. Similarly, the inner ring constitutes a higher surface current at 6.3 GHz, verifying its resonance. The surface current distributions at 3.5 GHz and 6.3 GHz are shown in Fig. 3.2 (f) & (g). Due to the strong coupling between the rings produces capacitance (C12).

The proposed DRDB-AMC UC can be verified through its EC, shown in the Fig. 3.2 (b). In the EC of AMC, the inner ring produces the capacitor (C1), inductor (L1), and resistor (R1), and the outer ring produces the capacitor (C2), inductor (L2), and resistor (R2). C12 is the capacitance between two rings, and the Capacitor (Ca) is produced because of the adjacent DRDB-AMC UC. Lastly, Rd is the dielectric capacitance, and Rg is the grounding resistor of the UC. These components were tuned to obtain identical results to the proposed DRDB-AMC UC. In Fig. 3.2 (c) & (d), the magnitude and phase response of the DRDB-AMC UC and its EC are shown. It depicts that both circuit responses are identical. The resonant frequency (f_0) of AMC-EC is calculated from the Eqn. 3.2 to Eqn. 3.5 present in [156].

$$f_0 = \frac{1}{2\pi\sqrt{L_F C_F}} \tag{3.1}$$

$$L_F = Lp||Ld \tag{3.2}$$

$$Lp = L1||L2 \tag{3.3}$$

$$C_F = Cp + C12 \tag{3.4}$$

$$Cp = C1 + C2 + Ca \tag{3.5}$$

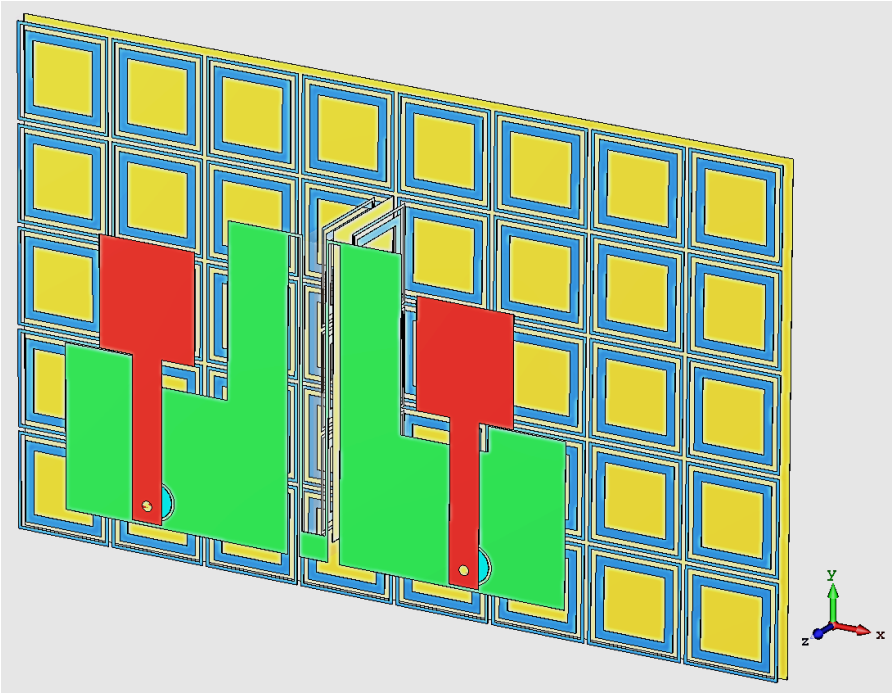

(a)

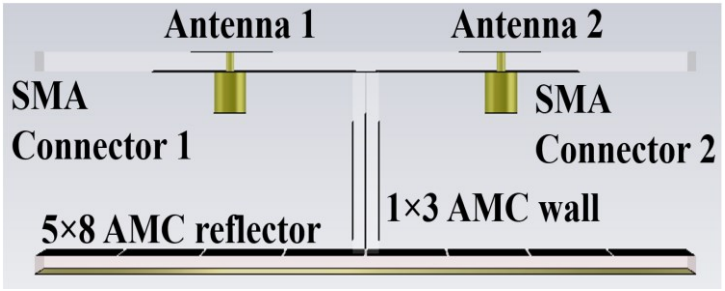

(b)

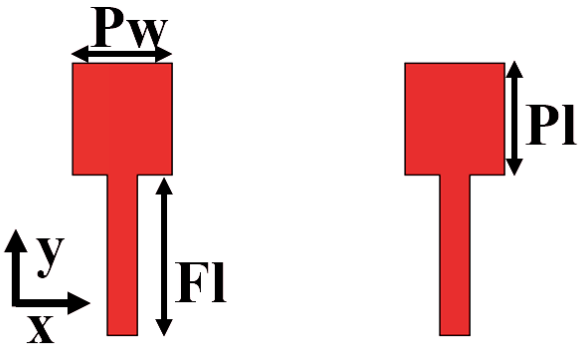

(c)

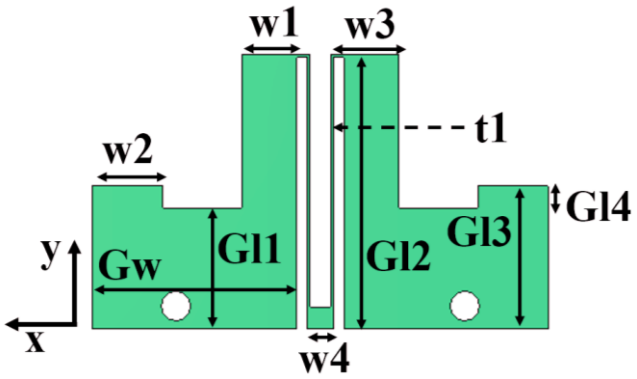

(d)

Fig. 3.3: Proposed MIMO Antenna structure: (a) Perspective view, (b) Side view, (c) Patch, (d) Ground Plane. (Pw = 10, Pl = 11, Fl = 16, Tw = 3.1, Gl1 = 13.7, Gl2 = 30.7, Gl3 = 16.4, Gl4 = 2.72, Gw = 23.3, w1 = 6.3, w2 = 8, w3 = 7.8, t1 = 0.3, hs2 = 1.55, all dimensions are in mm, $\varepsilon_r = 4.4$.)

The proposed MIMO antenna structure is shown in Fig. 3.3 (a) & (b). Fig. 3.3 (c) & (d) depicts the design parameters and substrate information. The proposed MIMO

antenna is designed in four steps, as shown in Fig. 3.4. At first step, Antenna A (Ant. A) is consists of conventional square patch antennas, Antenna 1 (Ant. 1) and Antenna (Ant. 2), fed through a microstrip line of width (Tw) and a partial ground plane is employed to obtain a UWB impedance BW. To deflect E-fields away from interfering with each other, a side arm of width 'w1' of 6 mm is introduced in the ground plane as shown in Fig. 3.4 (a). This increases port isolation between Ant. 1 and Ant. 2, which are 5.1 mm apart from each other. These two antennas are connected by a 0.5 mm thin copper line. To achieve UWB impedance matching below < -10 dB, a protrusion stub of width 'w2' of 8 mm is added to the ground plane, and its length (Gl1) is set to 13.5 mm for UWB characteristics. The side arm length (Gl2) is set to 30 mm. The Ant. A resonates from 2.55 GHz to 8 GHz, and it has an isolation of more than 20 dB, as shown in Fig. 3.5 (a). Due to the partial ground plane, a UWB characteristic is achieved at the expense of the back radiation, which results in low gain as depicted in Fig. 3.5 (b).

Since Ant. A suffers through low gain and high back radiation due to the partial ground plane in the lower frequencies; a 5 × 8 DRDB-AMC array is added as a reflector beneath the Ant. A, at a height (h) of 0.11 λ_o mm (λ_o at 2.37 GHz), this new iteration of antenna is called Antenna B (Ant. B), shown in Fig. 3.4. The MIMO antenna parameters w2 and Gl1 are kept the same as those of Ant. A, to analyse the impact on the S-parameters. The Ant. B resonates from 2.53 GHz to 8 GHz as shown in Fig. 3.5 (a); however, the resonance is affected around 7.1 GHz (-9.02 dB) because of the coupling due to the AMC. Also, the isolation has been affected for the frequencies below 5 GHz, as shown in Fig. 3.5 (a). On the other hand, with the introduction of the 5 × 8 DRDB-AMC reflector to the MIMO antenna, the gain has enhanced remarkably from 2.3 dBi to 7 dBi at 3 GHz. A small gain variation is observed over the band, as shown in Fig. 3.5 (b), which does not affect the 5G communication.

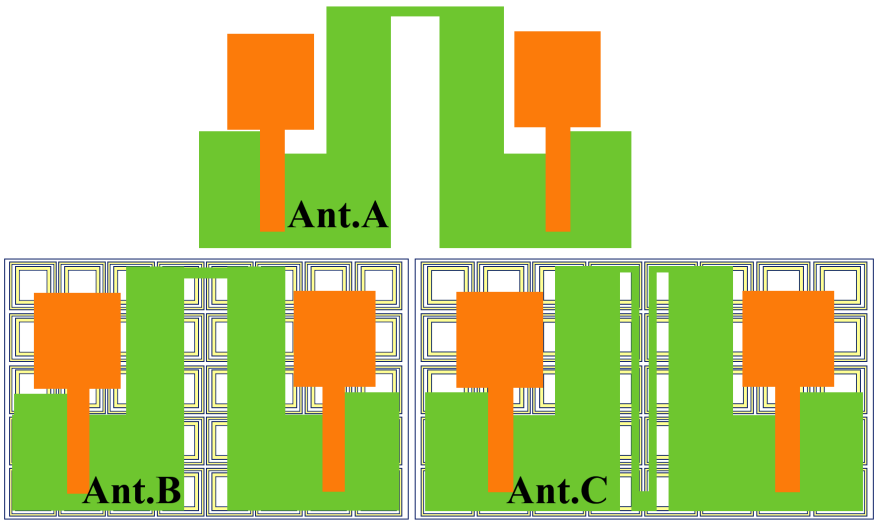

Fig. 3.4: Steps to design MIMO antenna from Ant. A to Ant. C.

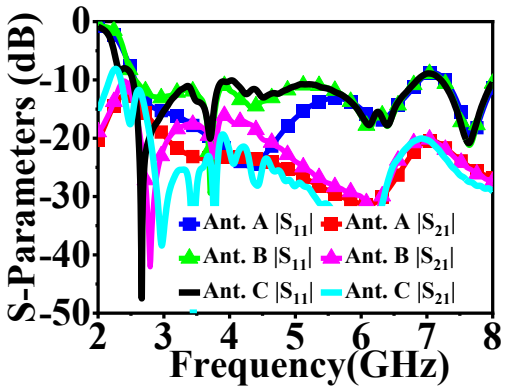

(a)

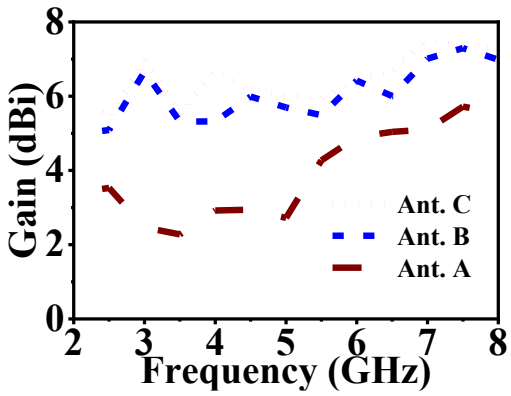

(b)

Fig. 3.5: (a) S-Parameters for Ant. A, Ant. B, Ant. C and Ant. D, (b) Gain Vs. Frequency plots for Ant. B and Ant. C.

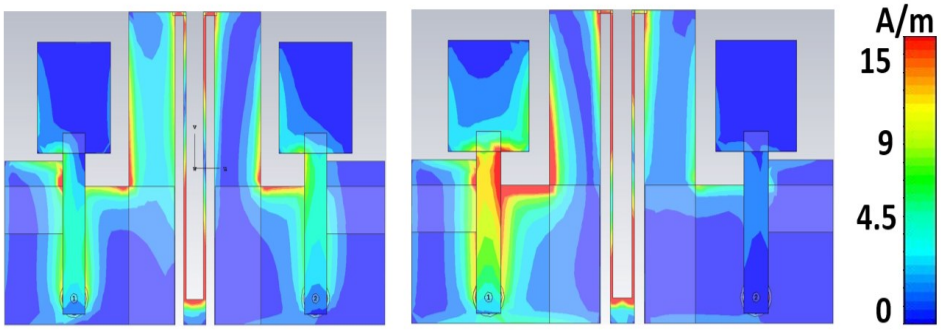

(a) (b)

Fig. 3.6: Surface current distribution at 2.4 GHz for active port 1, (a) Ant. D without AMC wall, (b) Ant. D with AMC wall.

To improve resonance and isolation, the thin copper line which separates antenna 1 & antenna 2 is modified into a 'U' shaped neutralising line (NL) as depicted in Fig. 3.4; this iteration of the antenna is called Antenna C (Ant. C), shown in Fig. 3.4. As the NL is to the MIMO antenna, the resonance length is elongated the lower resonance is shifted to a lower spectrum. To ensure impedance matching at 2.4 GHz, the side arm length (Gl2) is increased from 30 mm to 30.7 mm, which also increases NL length. Thus, the resonance magnitude is improved at 2.45 GHz from -4.01 dB to -8.22 dB as shown in Fig. 3.5 (a). The isolation for the lower frequencies is improved as compared to Ant. B. However, an isolation of 12 dB is observed around 2.45 GHz, which is poor for 5G communication. The poor isolation is due to the mutual coupling between the MIMO antenna and AMC array. The gain of Ant. C is not affected by introducing NL, as shown in Fig. 3.5 (b).

The poor isolation between the two ports at 2.4 GHz is because of the interaction of reflected waves from Ant. 1 and Ant. 2 off the 5 × 8 AMC array, which interacts and disrupts both resonance and isolation around 2.4 GHz, as shown in Fig. 3.5 (a). The surface current distribution at 2.4 GHz shows that the surface current is entering Ant. 2 from Ant. 1, which is affecting the port isolation and resonance, as shown in Fig. 3.6 (a). To realize resonance at 2.4 GHz while maintaining high gain and isolation levels of approximately 20 dB across the operational BW—without the use of vias, complex circuitry—two vertical 1 × 3 DRDB-AMC walls, based on the proposed AMC unit cell, are positioned beneath Ant. C. This iteration is called Antenna D (Ant. D), is placed between antenna 1 and antenna 2. With this approach, the predefined height 'h' between the MIMO antenna and the AMC reflector is utilised for isolation enhancement rather than incorporating MMT/ MS, which will increase the antenna profile. The use of the same AMC structure for the wall as the AMC reflector also saved time to design and analyse a different MMT/ MS. This solution avoids intricate designs and structures, which make fabrication and measurements difficult. Along with this, the antenna profile may increase, as reported in [113], [154], [155], [156].

These vertical AMC walls are arranged back-to-back as depicted in Fig. 3.3 (b). The interfering E-fields from both antennas are redirected away from each other. This prevents mutual coupling and improves impedance matching around 2.4 GHz. This is validated through the current distribution shown in Fig. 3.6 (b). It shows with DRDB-AMC walls installed in the MIMO antenna, a small amount of surface current around port 2 when port 1 is active and similar results will be observed for port 1 when port 2 is active. In this way, Ant. D operating frequency is lowered to 2.37 GHz from 2.53 GHz, and isolation greater than 19.66 dB is obtained, as shown in Fig. 3.7 (a) and (b), respectively. And as the isolation around 7.2 GHz is improved, its resonance is also improved. This proves that mutual coupling does, in fact, affect the impedance matching. The gain plots of Ant. C and Ant. D is compared in Fig. 3.7 (c), gain is enhanced at 2.5 GHz from 3.7 to 5.1 dBi, 3.5 GHz from 3.2 to 5.8 dBi, 5.5 GHz from 4.2 dBi to 6.8 dBi, and 7.2 GHz from 5.8 to 7.1 dBi. The gain variation of 2.5 dB is observed over the operating BW.

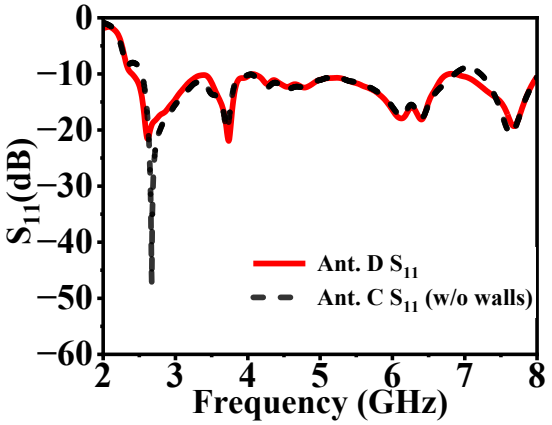

(a)

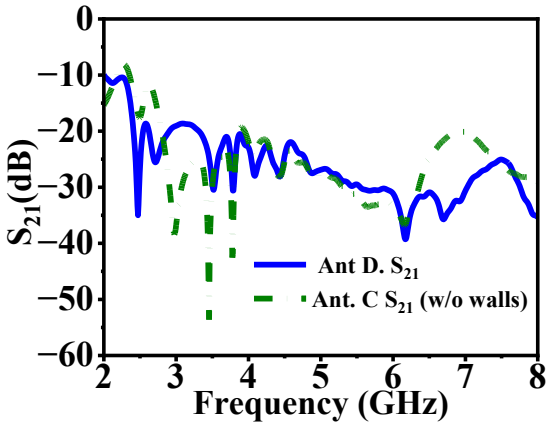

(b)

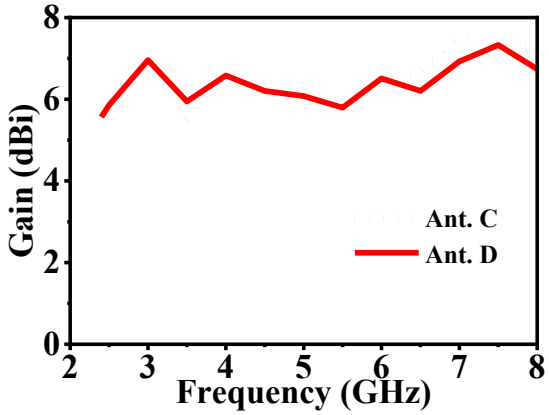

(c)

Fig. 3.7: (a) Simulated S_{11} for Ant. D, (b) Simulated S_{21} for Ant. D and (c) Simulated gain for Ant. D.

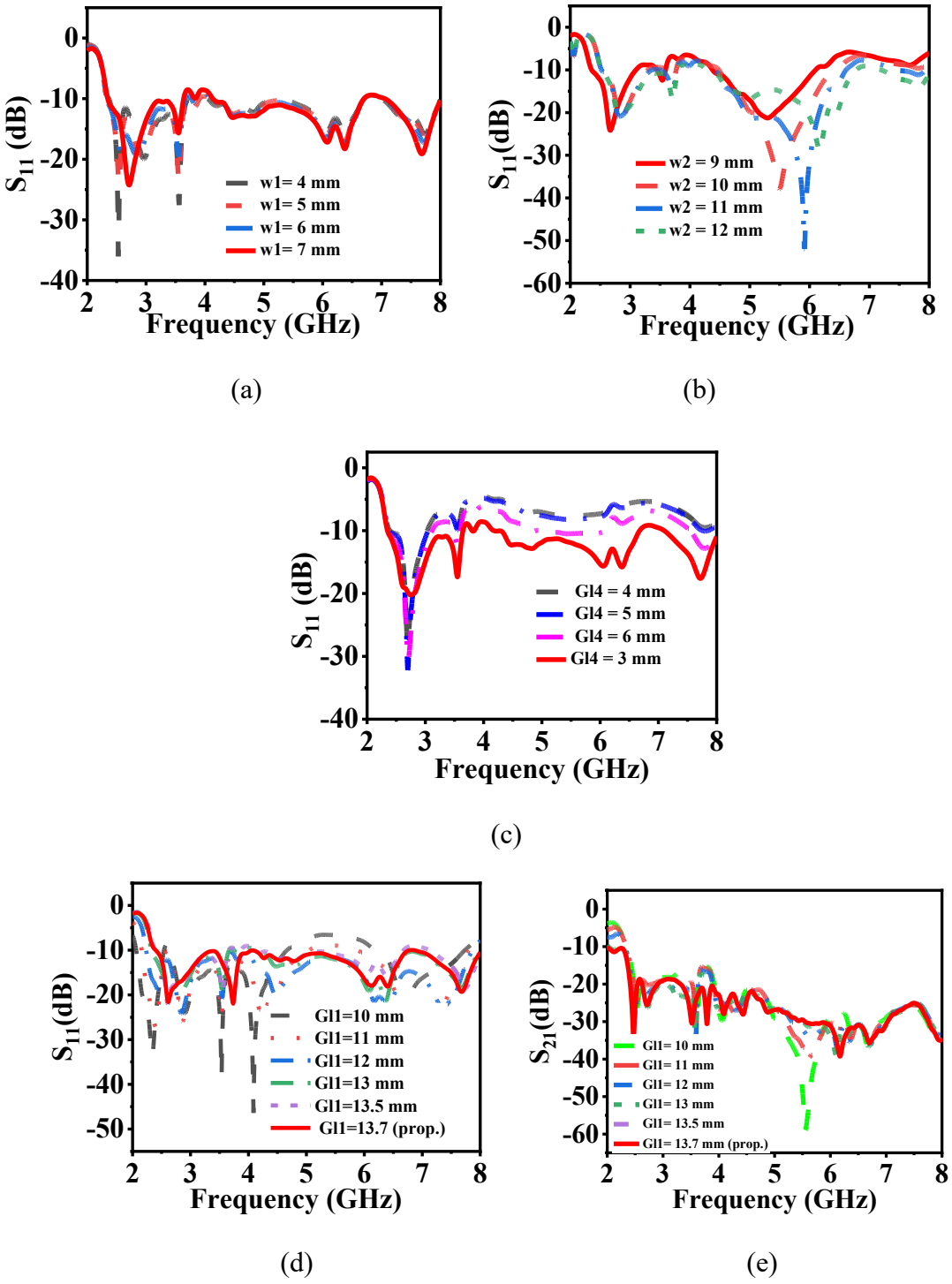

Fig. 3.8: Parametric Analysis: (a) S_{11} for Side arm width (w1), (b) S_{11} for Protruding stub width (w2), (c) S_{11} for Protruding stub length (Gl4), (d) S_{11} for ground plane length (Gl1), and (e) S_{21} for ground plane length (Gl1).

The antenna parameters w1, w2, Gl1, and Gl4 were found to have a significant impact on impedance matching; hence, a parametric analysis of these variables was carried out, as shown in Fig. 3.8. The analysis suggested that the optimum values of w1, w2, Gl1, and Gl4 are 6.3 mm, 8 mm, 13.7 mm, and 2.72 mm, respectively, which results in UWB impedance BW and maintain high isolation. A separate parametric analysis was carried out on the height 'h' between the antenna and the AMC reflector in order to optimise and verify UWB impedance matching and high isolation. The corresponding S11, S21, and gain plots for different values of h are shown in Fig. 3.9 (a), (b) & (c), respectively. The parametric results indicate that the optimum height for the proposed antenna is h = 0.11 λ_o, i.e., 15 mm. Therefore, Ant. D is chosen as a proposed antenna design.

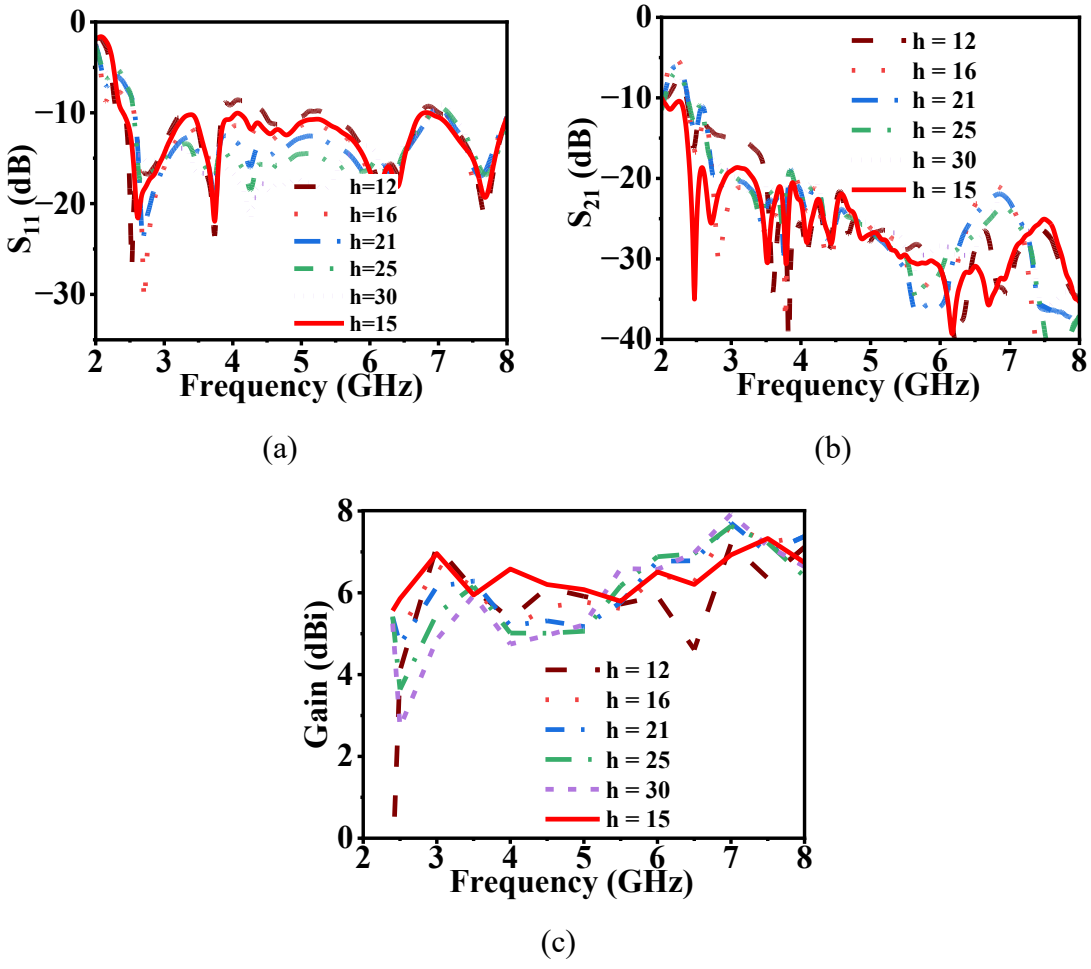

Fig. 3.9: Parametric analysis of height 'h' for the Proposed antenna design (a) S_{11}, (b) S_{21}, and (c) Gain.

3.3 Measured Results and Discussion

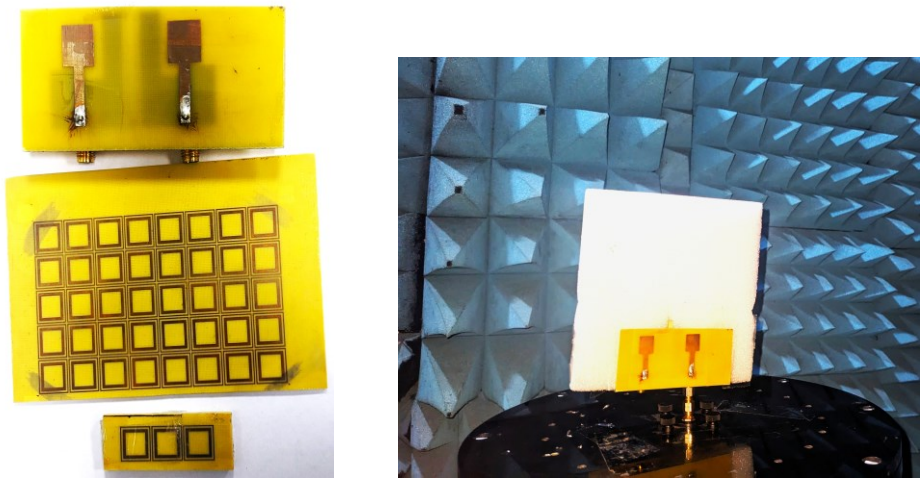

(a) (b)

Fig. 3.10: (a) Fabricated prototype of the proposed antenna structure, (b) Radiation Pattern testing.

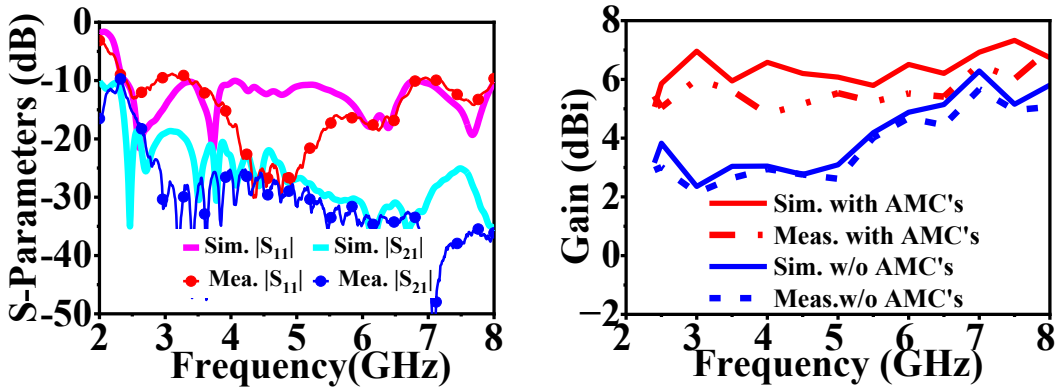

(a) (b)

Fig. 3.11: Comparison of simulated and measured results of the proposed antenna (Ant. D) (a) S-parameters plot, (b) Gain plot.

Post simulation, the proposed MIMO antenna prototype is fabricated, which consists of three parts: the MIMO antenna, DRDB-AMC reflector and walls, as shown in Fig. 3.10 (a). The assembled proposed MIMO antenna is tested in the anechoic chamber. To maintain a height 'h' of 15 mm, a foam spacer is used. This foam spacer also holds the vertical DRDB-AMC walls at the centre beneath the MIMO antenna. The measured S-parameters of the proposed MIMO antenna are compared with the simulated S-parameters and are shown in Fig. 3.11 (a). The measured antenna resonates from 2.34

GHz to 8 GHz, and the isolation is found to be greater than 20 dB from 2.56 GHz. The isolation affected around 2.4 GHz is due to human errors and fabrication tolerance. Another reason for the deviation in the measured results is the misalignment of the AMC walls while carrying out measurements. Due to this, measured S-parameters could be affected as compared to the simulated S-parameters over the operating BW. In Fig. 3.11 (b), the Gain plot for the proposed MIMO antenna is compared with the simulated results. As mentioned measured gain for the proposed MIMO antenna with AMC reflector and walls has a variance from the simulated gain. This is due to the misalignment errors during measurements.

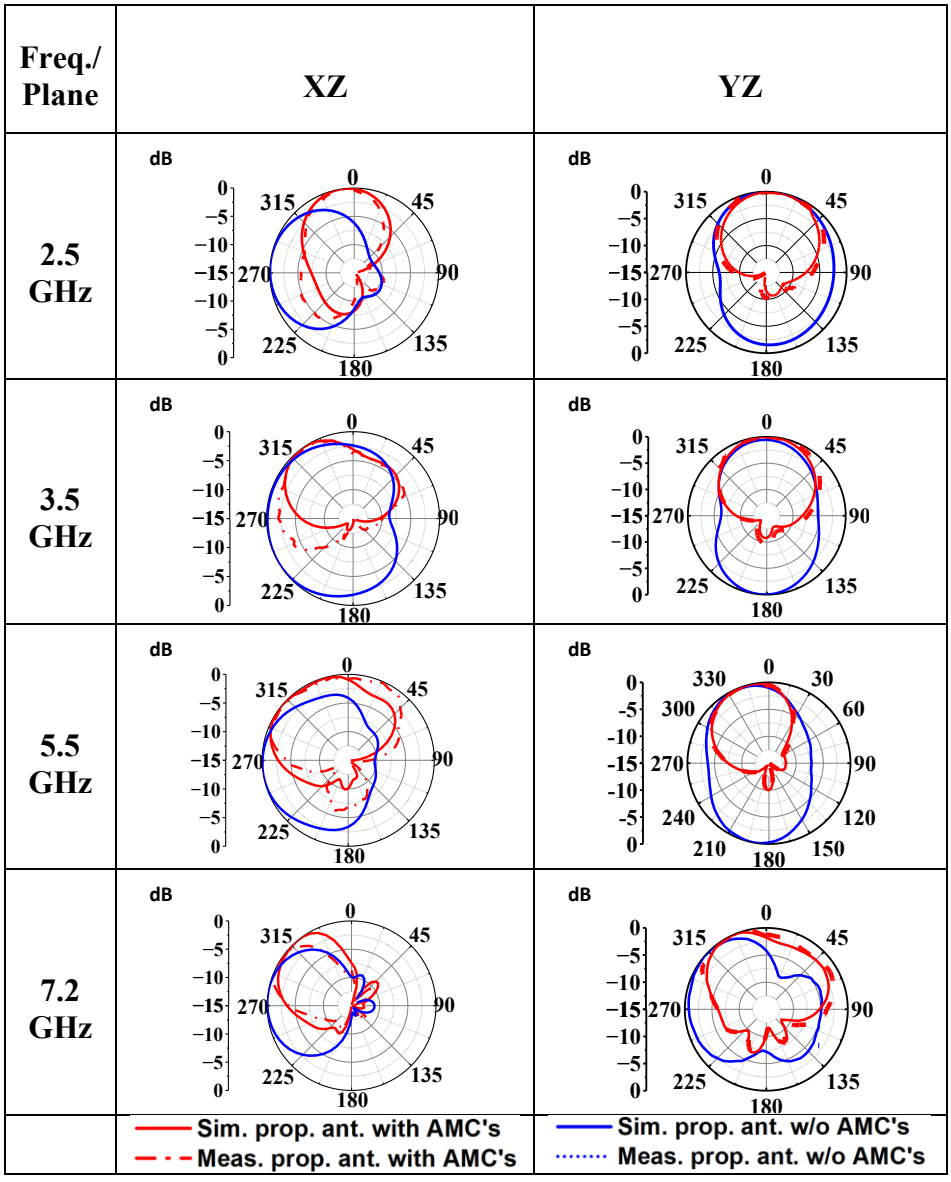

Fig. 3.12: 2D-Radiation patterns for the proposed MIMO antenna in XZ and YZ planes.

The fabricated prototype of the proposed MIMO antenna radiation patterns are measured in the anechoic chamber as shown in Fig. 3.10 (b). Since the proposed MIMO antenna is symmetric, Ant. 1 radiation patterns are presented in Fig. 3.12, which are measured in the XZ plane and YZ plane. The Ant. 2 radiation pattern will be identical to Ant. 1 radiation patterns because of the symmetric structure. However, the beam direction of Ant. 2 will be in the opposite direction of Ant. 1. A 5×8 DRDB-AMC array employed as a reflector reflects radiation in the broadside direction. The in-phase reflected waves with the original waves result in constructive interference and hence, enhancing the gain of the MIMO antenna. It is observed that at 2.5 GHz, 3.5 GHz, 5.5 GHz, and 7.2 GHz, the beams are directed at 4º, 36º, 53º and 45º, with respect to broadside radiation in the XZ plane. This is due to the use of the sidearm in the ground plane, which deflects E-fields away from the adjacent port. These tilted beams are called quasi-directional beams. The 3 dB angular beam widths are 79.3º, 72.2º, 128º and 71.4º at 2.5 GHz, 3.5 GHz, 5.5 GHz, and 7.2 GHz, respectively, in the XZ-plane. This shows that the beams are wider yet quasi-directive. The quasi-directional provides better coverage and reduces multipath losses with the MIMO configuration [153]. Therefore, quasi-directional beams at 2.5 GHz, 3.5 GHz, 5.5 GHz, and 7.2 GHz are beneficial for 5G communication.

3.4 Integration of the Proposed MIMO Antenna with the Vehicle

To verify radiation characteristics for IoT/IoV applications, the proposed antenna is integrated with the vehicle as a VBS antenna, as suggested in [152] and [153] and shown in Fig. 3.13. The 3D radiation patterns in Fig. 3.14 show no adverse effect when the proposed MIMO antenna is integrated with the vehicle; it is crucial for the VBS antenna to preserve its radiation characteristics [113] and [154]. Fig. 3.14 shows that the proposed MIMO antenna has preserved its quasi-directional radiation patterns at different frequencies, such as 2.5 GHz, 3.5 GHz, 5.5 GHz and 7.2 GHz. As depicted in Fig. 3.1(b), the proposed antenna may serve as a VBS antenna as shown in Fig. 3.13.

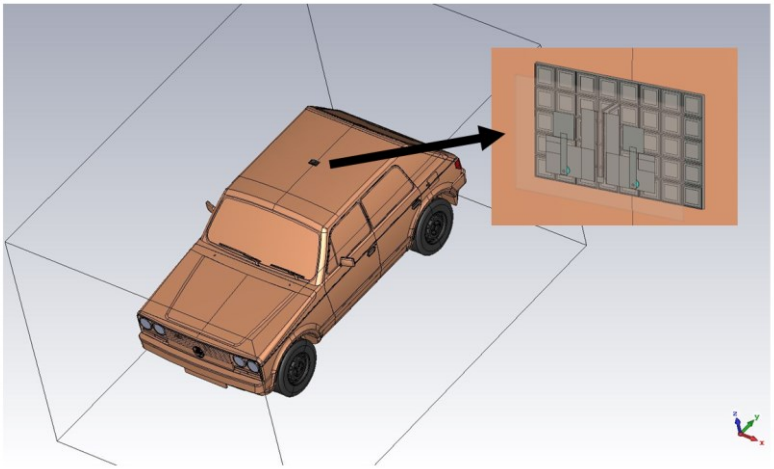

Fig. 3.13: Simulation setup for the proposed antenna as a VBS antenna.

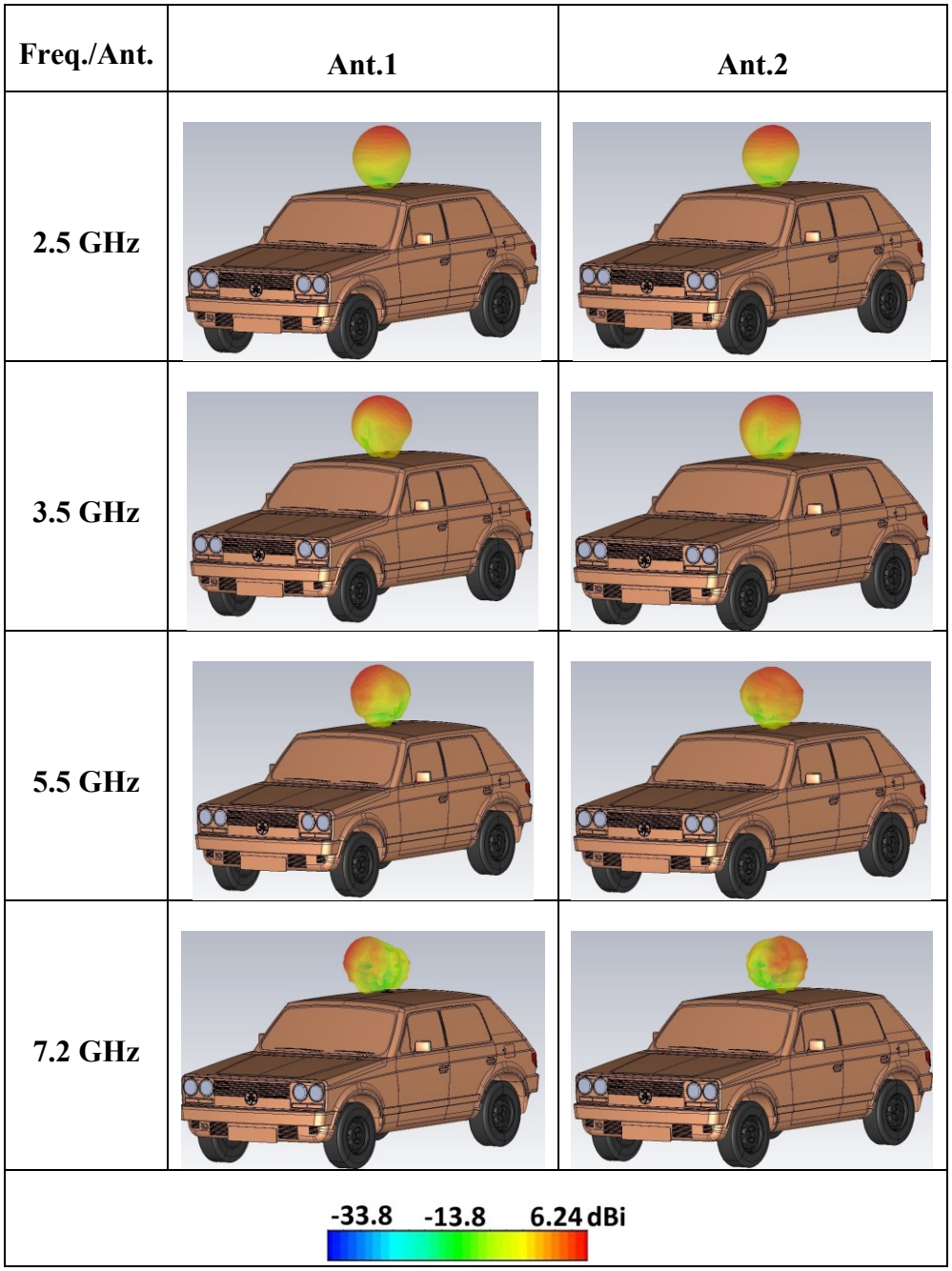

Fig. 3.14: 3D radiation patterns for the Proposed antenna integrated with the vehicle.

3.5 Proposed MIMO Antenna Diversity Performance

To study the diversity performance of the proposed MIMO antenna, Envelop Correlation Coefficient (ECC), Diversity Gain (DG), Channel Capacity Loss (CCL), and

Total active reflection coefficient (TARC) were calculated, referring to equations from [150], [159]. For the MIMO proposed antenna, the ECC < 0.0037 and DG is found to be ~10 dB. The CCL is < 0.12 bits/s/Hz, and TARC is below -10 dB. The ECC, DG, CCL and TARC are shown in Figure 15 (a), (b) and (c), respectively.

Table 3.1 compares this work with existing studies to highlight features such as impedance bandwidth, antenna size, isolation, ECC, and gain. The comparison indicates that the proposed antenna design supports a MIMO configuration, which presents additional challenges in achieving optimal values for all these parameters. The proposed antenna exhibits a wide impedance BW that envelops WiFi, WiMax, Bluetooth, and LTE frequencies (2.4 GHz - 2.4832 GHz, 2.1 GHz - 3.5 GHz, 2.2 GHz - 3.8 GHz), Mid-band (3.3 GHz - 3.6 GHz), the 5 GHz band (5.3 GHz - 5.8 GHz), and WiFi-6E (5.9 GHz-7.2 GHz). It also has high measured isolation exceeding 20.87 dB and ECC less than 0.0037, with a gain variation of 2.5 dB for the operating BW from 2.37 GHz to 8 GHz.

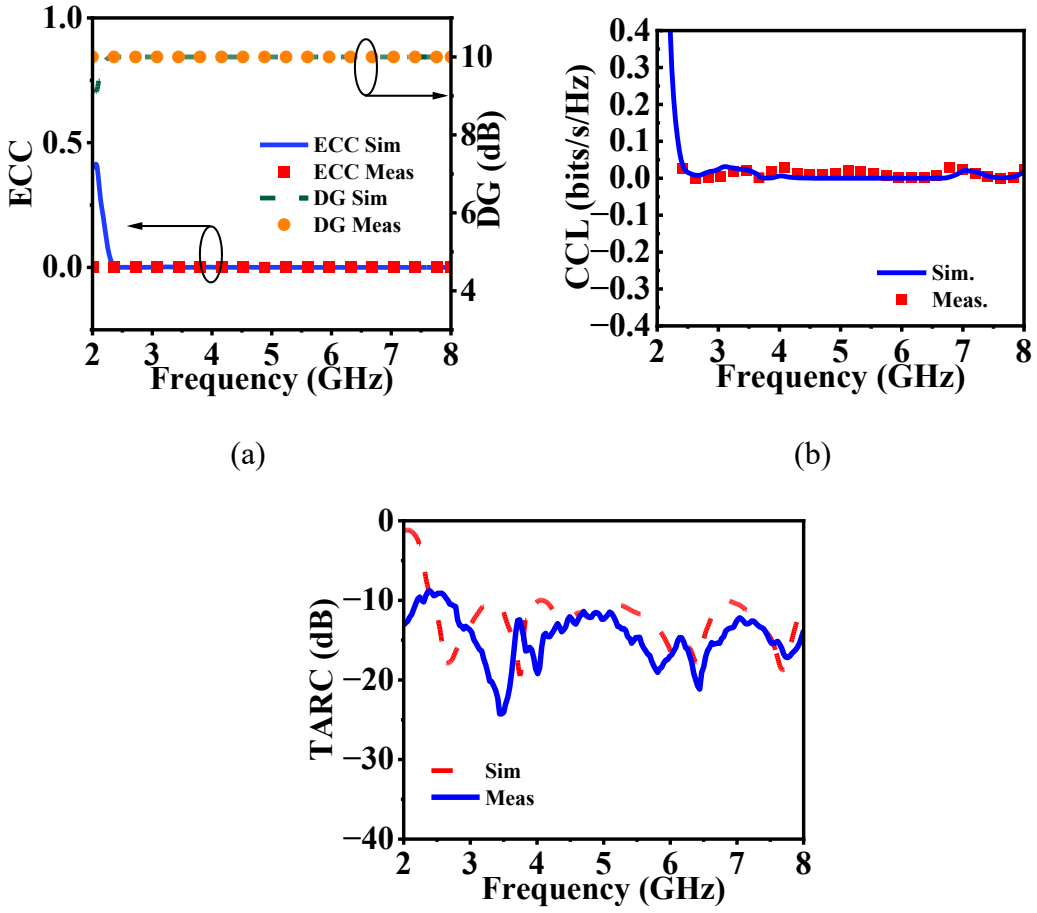

(a) (b)

(c)

Fig. 3.15: MIMO diversity performance (a) ECC and DG, (b) CCL, and (c) TARC.

Table 3.1: Performance comparison of the previous antenna design Vs. Proposed antenna.

Ref.	Year	Freq. (GHz)	%BW	Ant. size (mm^3)	Isolation meas. (dB)	Gain (dBi)
[143]	2021	0.617-5 (@5.6dB)	156.06	38.5 × 14.9 × 60	Single ant.	< 2
[146]	2022	10-30	115.5 mm (focal-length) 129 mm (dia. of ref. array)	Rogers RO 4003 C	Single (horn ant.)	14.11 dBi~ 27.51
[148]	2023	2.45, 3.5, 4.6, 5.9,7.4	< 10	90 × 90 × 21.2	Single ant.	2.26-7.3
[149]	2023	2.45, 3.5, 6.5, 8.1	11.81, 50.92, 5.38, 1.18	95 × 101 × 21.2	Single ant.	3.6-8
[152]	2020	1.95-6.25	105.13	50 × 50 × 33.3	>16.5	3.3-6.16
[153]	2022	2.35-2.65, 3.25-3.8, 5-6.1, 7.15 - 8.5, 23-31	11.15, 16.9, 19.8, 17.2, 29.6	57 × 57 × 57	15-20	1-4, < 7
[113]	2021	7.55-22.85	100.65	138.2 × 69.6 × 37.7	>18.05	6.98-11.54
[154]	2022	2.85-10.9	117.09	300 × 300 × 1.524	> 22.4	10.37 - 14.82
[156]	2021	2.16-3.96	58.8	125.2 × 125.2 × 18	> 28	8.34-10.96
[109]	2022	3.7-10.8	97.93	55.05 × 55.05 × 19.2	< 18	4.2-6.5

[158]	2024	810-920, 2.35-2.5	12.71, 6.18	277.45 × 277.45 × 277.45	>30	7, 6.33 (max)
[67]	2017	5-5.5	9.5	100 × 50 × 45.5	NA	< 7
[160]	2023	9.3-11.2	18.53	80 × 80 × 16.62	NA	9.7-12.3
[161]	2023	4.7-5.33	12.56	180 × 100 × 37	NA	7.5-12.6
This work	**2025**	**2.37 to 8**	**108.52**	**80 × 50 × 18.1**	**> 20.87**	**5-7.5**

3.6 Summary

In this chapter, BW limitations arising due to the narrowband, multiband or wideband antennas in the MIMO system for the 5G communication are overcome by designing a 5G UWB MIMO antenna for Sub-6 GHz frequencies, targeting IoT/IoV applications that demand high data rates at lower frequency ranges. An AMC reflector and walls are incorporated to enhance antenna gain and port isolation, respectively. The structural simplicity enables ease of analysis, fabrication and testing. The Sub-6 GHz antenna proposed in this chapter, resonates from 2.37 GHz to 8 GHz, effectively covering all major Sub-6 GHz 5G frequencies such as Wi-Fi, WiMax, Bluetooth, LTE, mid-band 5G, Wi-Fi 6E, and the downlink satcom band. The antenna achieves a wide fractional bandwidth of 108.58% (2.37 GHz to 8 GHz) with a peak gain enhancement from 2.3 dBi to 7 dBi at 3 GHz using a 5×8 DRDB AMC array reflector. The port isolation of more than 19.66 dB is achieved using two 1×3 DRDB AMC walls. The antenna exhibits excellent MIMO diversity performance with ECC < 0.0037, CCL < 0.12 bits/s/Hz, and TARC < -10 dB. The size of the proposed antenna is only 0.39 λ_o × 0.63 λ_o × 0.14 λ_o at 2.37 GHz. This makes it compact with high gain and isolation. Moreover, the proposed antenna is integrated with a vehicle in the simulator to verify its radiation characteristics for IoT/ IoV applications. It was found that the antenna retains its radiation patterns when placed on the vehicle.

Chapter 4

Design of Partially Reflective Surfaces to enhance Gain and ARBW of the CP antenna

4.1 Introduction

Recent studies have revealed that around half of the world's population has no access to the internet. It will be expensive to provide terrestrial coverage with increasing capacity for remote, rural and urban areas as well. Hence, Satellite communication will have an important role as a parallel solution for the coverage problem. Moreover, it will open new avenues for the 5G antennas [162]. To prevent polarisation mismatch and multipath effects between transmitting antennas and receiving antennas, CP antennas are employed in the wireless communication system for seamless p2p communication [163]. Small CP antennas with high and small profiles can be installed on the small 1U cube-satellites (CubeSat) of size 100×100×100 mm^3 for p2p communication [164]. Therefore, high gain CP antennas with a low profile have caught the attention of researchers for 5G and CubeSat applications. To fulfil this requirement for CP antennas, several techniques have been adapted by the researchers to attain CP, such as trimmed edges patch [76], a 90º phase shift feed [165], slots or combinations of trimmed edges and slots [166], [167], defected ground structures [168], [169], [170], Dielectric resonators (DR) with slots [171], [172], 3D printed polarisation converters [173], [112]. These techniques easily enable CP and emit CP waves from the antenna. Although most antenna structures are CP, the ARBW did not match the impedance BW. It means ARBW is narrower than impedance BW, and polarisation compatibility is found for a small fraction of impedance BW. Which is not suitable for any practical communication. However, the ARBW matching with impedance BW was found in [169], [170], but these antennas don't have sufficiently high gain. To attain CP in the low profile antenna, MMTs/ MSs have played an important role for different applications such as 5G communication and wearable antennas [174], [175].

The MMTs/MSs received special attention because of their ability to manipulate EM waves to generate CP and high gain with the periodic and non-periodic placement of UCs while keeping the antenna profile low [176], [177], [178] and [179]. Although these antennas are CP with a low antenna profile but they have narrow ARBW. The MS are used to convert LP to CP; when an MMT/ MS is incident with an EM wave, the reflected wave consists of two E-field components, one component has the same polarisation as the EM wave, called co-polarised, and the other is the orthogonal component to the incident

polarisation, called cross-polarisation. When the MMT/MS cross-polarisation has a high magnitude and the co-polarisation has a low magnitude, with a phase difference between them is 90º, then LP is converted to CP [180], [181]. However, these polarisation converters are relatively large in size, and when combined with an antenna, they further increase the overall structural profile. A dipole antenna with high gain and CP having a wide axial beamwidth is achieved using an AMC [182]. However, narrow ARBW is obtained.

The techniques mentioned above have complicated and large structures. Although MMT integrated CP generating antennas have a large profile, yet there is an MMT antenna known as the Fabry-Perot Cavity antennas (FPCA). This antenna configuration can have a low profile and size of the 1U-CubeSat [183]. The FPCA is an excellent structure to generate CP with high efficiency. The FPCAs are mainly divided into four categories. First, CP radiators are used as feed, and a partially reflective surface (PRS) forms an FP cavity, which enhances the gain of the CP radiator. The PRS are designed in such a way that they do not affect the ARBW [184], [185], [186]. The second category is PRSs are designed to convert LP to CP. The feed emits an LP wave, which is converted to a CP wave as mentioned earlier. These PRS structures are also responsible for the gain enhancement [187], [188], [189], [190]. The third category is feed networks/techniques that are employed to feed the patch, which generate orthogonal modes to result in CP waves.[33] and [34]. In the last category, an anisotropic medium is filled between the PRS layer and the radiator to generate CP waves, while the PRS layer is responsible for gain enhancement [111], [193], [194]. However, the anisotropic media should not lower the radiation efficiency and increase antenna complexity while measuring the antenna.

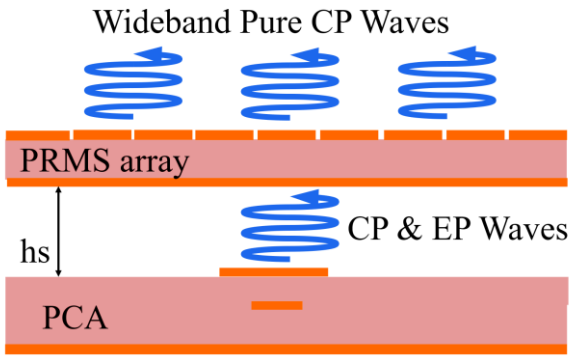

Fig. 4.1: Schematic for the proposed CP-FPCA.

The above mentioned CP generating FPCA has a high gain, but the ARBW is smaller than the impedance BW. It can be noticed that obtaining ARBW matching with impedance BW is challenging while maintaining a high gain with a low antenna profile

[183]. It is also observed that EP and how to convert EP waves into CP waves is not addressed in the FPCA mentioned above. Ideally, for pure CP, the ARBW ≤ 3 dB, for EP, the ARBW lies between 3.1 dB to 15 dB and for LP, ARBW ≥ 15 dB [195], [196].

In this chapter, the stated challenges are resolved by designing a high-gain, wideband CP-FPCA, as shown in Fig. 4.1. A 9 × 9 array of partially reflective MS (PRMS) UCs are employed to construct an FP cavity, which significantly improves both the gain and ARBW of the feeder, i.e., proximity-coupled antenna (PCA) for the operating BW. The proposed antenna has an ARBW from 9.9 GHz to 12.21 GHz, which overlaps the impedance BW from 9.9 GHz to 12.31 GHz. Within this band, the PCA inherently produces EP, which is effectively converted into wideband CP by modifying the PRMS layer. This polarisation conversion mechanism enhanced the 3 dB ARBW from 790 MHz to 2.31 GHz and improved the peak gain from 7.3 dBi to 17.1 dBi at 10 GHz. The following section discusses the design and analysis of the PRMS UC and PCA as a feed.

4.2 Design of PRMS UC and PCA

4.2.1 Design and Analysis of PRMS UC

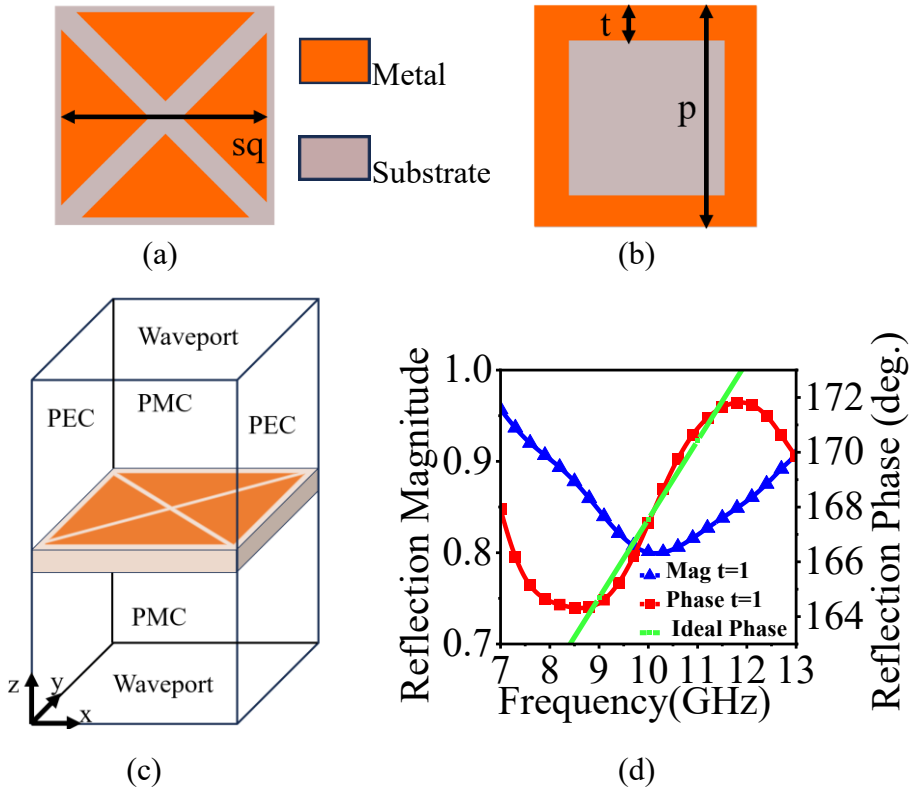

Fig. 4.2: Proposed PRMS UC and its response at t =1 mm, (a) Top view, (b) Bottom view, (c) Simulation setup, (d) Reflection magnitude & phase plot.

A PRMS UC is designed with a size of 8 × 8mm^2 and a thickness of 1.5 mm on Rogers RT duroid 5880 substrate with a dielectric constant of 2.2. On the top layer of the UC, the square patch of length sq = 7.8 mm has a cross slot with a width w1 = 0.6 mm, as shown in Fig. 4.2 (a). The bottom layer of the PRMS UC has a square ring of size 8 × 8 mm^2 and thickness of t = 1 mm in the x and y directions, as shown in Fig. 4.2 (b). The boundary conditions PEC and PMC are applied in the x-direction and y-direction, respectively. The UC is excited via waveports in the z-direction, as shown in Fig. 4.2 (c). To achieve high reflectivity within the PRMS FP cavity and a positive phase gradient, the reflection magnitude of the PRMS UC is optimised between 0.82 and 0.88 for frequencies from 9 GHz to 12.5 GHz. For the resonance, the following condition needs to be satisfied [197],

$$(\Phi + \phi) - 2\beta hs = \pm 2n\pi, \text{ and } n = 0, \pm 1, \pm 2, \ldots \quad (4.1)$$

where Φ is a ground plane phase, ϕ is the PRMS simulated reflection phase, and 'hs' is the height of the FP cavity. As per Eqn. 4.1, the departing EM waves from the cavity have the same phase, resulting in constructive interference and a high gain. Whereas some EM waves will reflect into the cavity. Therefore, Eqn. 4.1 can be rewritten as [198],

$$\phi = \frac{4\pi hsf}{c} - \Phi + 2n\pi, \text{ and } n = 0, \pm 1, \pm 2, \ldots \quad (4.2)$$

To maintain a low profile of the FP cavity, n = 0 is preferred. For the fixed operating frequency, the height of the cavity 'hs' can vary with the variation of ϕ. In this way, a low-profile FPCA can be achieved. The directivity (D) of FPCA can be calculated from the Eqn. 4.3 given below,

$$D = 10log\frac{1+R}{1-R} \quad (4.3)$$

where 'R' denotes the reflection magnitude of the PRMS UC. A larger reflection magnitude enables higher gain, but at the expense of a narrower BW. Therefore, to achieve a wider bandwidth, a moderate reflection magnitude—typically in the range of 0.80 to 0.88—is chosen. The square ring at the base of the PRMS UC contributes to high reflectivity, whereas the upper patch with a cross-slot introduces a positive reflection phase gradient. The magnitude and phase responses of the PRMS are shown in Fig. 4.2 (d). The ideal phase is calculated from Eqn. 4.2 is also plotted in Fig. 4.2, which depicts that the simulated phase obtained for the PRMS UC matches the ideal phase.

4.2.2 Design of the FPC feeder PCA

As discussed earlier, CP can be commonly generated in rectangular patch antennas by trimming or chamfering the diagonal edges [76]. The E-field vector ($\boldsymbol{E}$) of this CP antenna is decomposed into two equal magnitude but orthogonal components $\boldsymbol{E_\theta}$ and $\boldsymbol{E_\phi}$. The phase difference between these two orthogonal components is 90º. The Eqn. 4.4. and 4.5 describes how E-field components are decomposed,

$$\boldsymbol{E} = (\boldsymbol{x}.\boldsymbol{E_\theta} + \boldsymbol{y}.\boldsymbol{E_\phi})e^{-jk_0 z} \quad (4.4)$$

$$|E_\theta| = |E_\phi| \text{ and } \measuredangle E_\theta - \measuredangle E_\phi = \pm 90^o \quad (4.5)$$

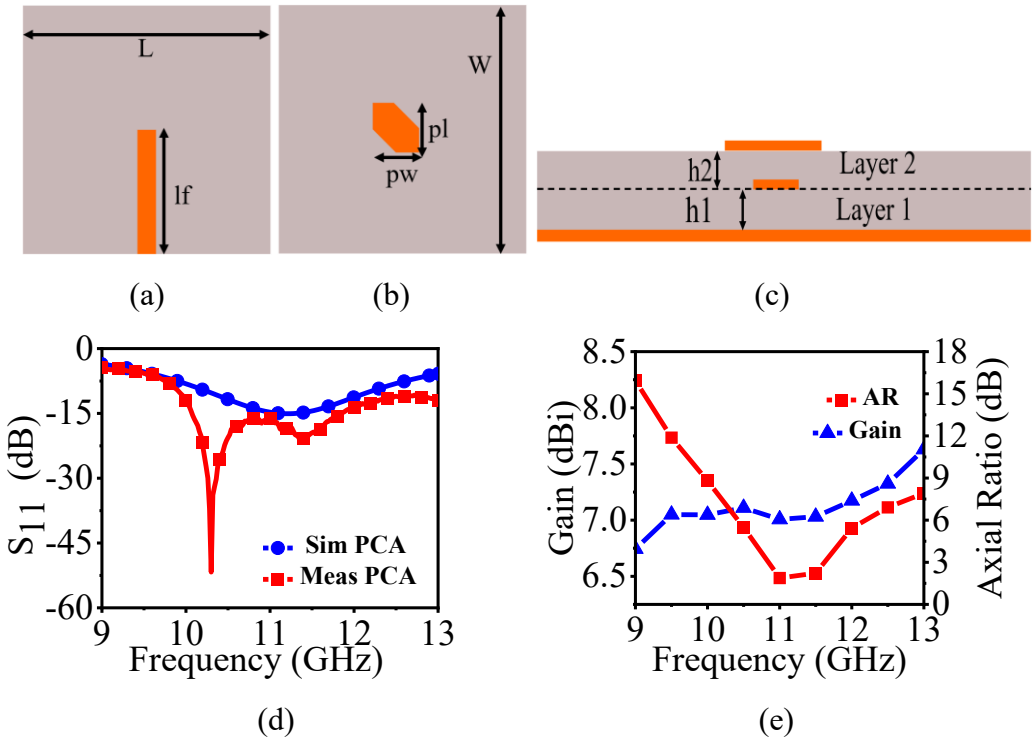

Fig. 4.3: Design of PCS (a) feedline, (b) patch, (c) Side view, (d) S_{11} plot for PCA and (e) Gain & AR plot for PCA. (L = W = 80, lf = 40, pl = 9, pw = 7.5; all dimensions are in mm).

The designed PCA with chamfered or trimmed diagonal edges generates RHCP waves, is shown in Fig. 4.3 (a) & (b). The designed PCA has two layers of Rogers 5880 substrate with a dielectric constant of 2.2. The height of layer 1, h1 = 1.55 mm, a feedline is designed on the top side to excite a chamfered patch, present on the top side of layer 2. Layer 2 has a substrate height, h2 = 0.79 mm, which only contains a patch on the top side and the copper on the bottom side is etched out. The layer 2 is placed on top of layer 1, as shown in Fig. 4.3 (c). The designed PCA resonates from 10.26 GHz to 12.19 GHz. The simulated and measured S_{11} for the PCA are compared in Fig. 4.3 (d), which depicts the simulated and measured S_{11} are in good agreement. The simulated gain of the PCA is approximately 7 dBi for the operating frequencies, as shown in Fig. 4.3 (e). The 3dB ARBW of the PCA is 790 MHz from 10.84 GHz to 11.63 GHz, as shown in Fig. 4.3 (e). As it is known, the EP waves occur either due to the orthogonal components of the E-field with a phase difference of 90º having unequal magnitudes or equal magnitudes of orthogonal components with a phase difference not equal to 90º. The AR plot in Fig. 4.3 (e) shows that the designed PCA at frequencies 10 GHz and 12 GHz have AR 9 dB and 6

dB, respectively, which is greater than 3 dB but less than 15 dB, indicating the presence of EP in the impedance BW [195].

4.2.3 Design and Assembly of FPC

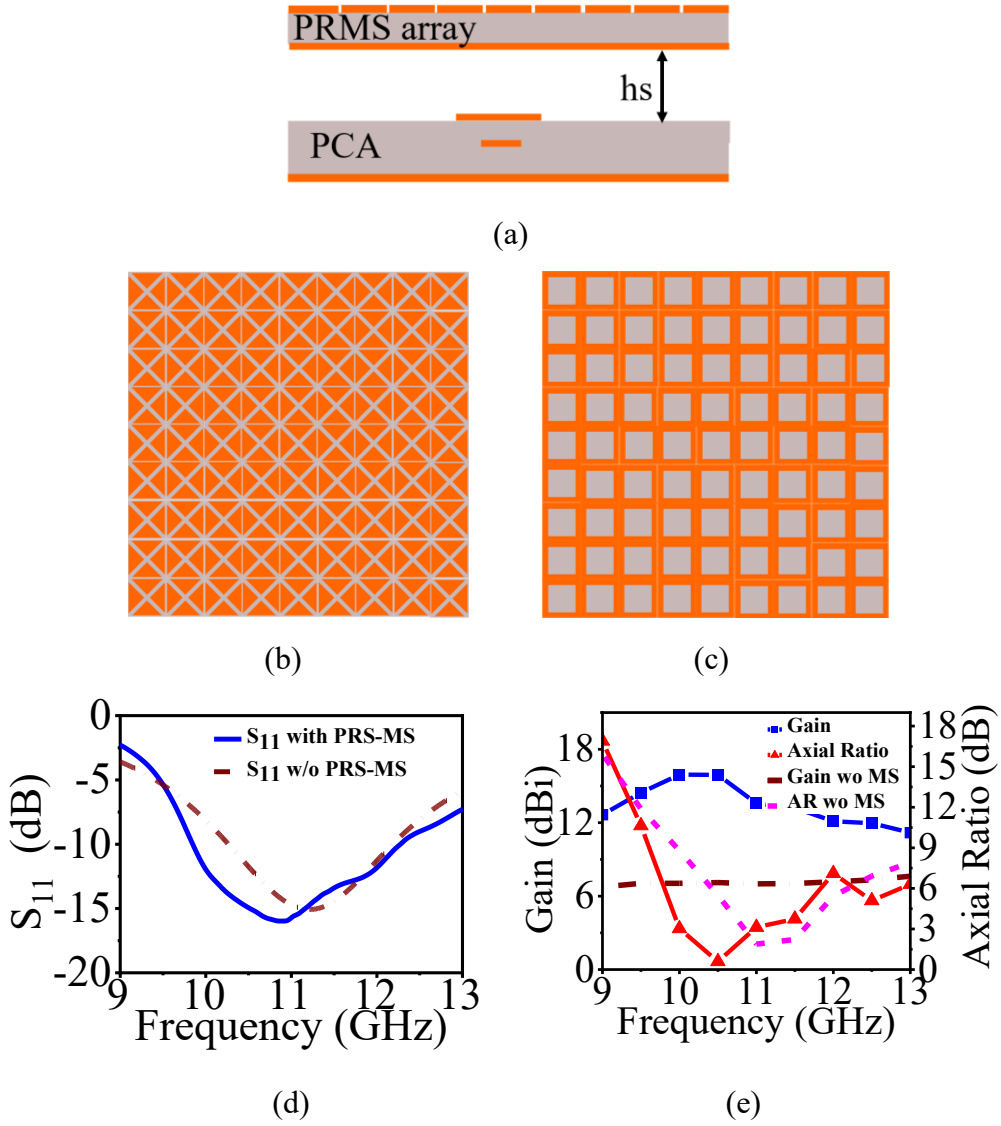

Fig. 4.4: PRMS-PCA when t = 1mm (a) FPCA assembly, (b) Top view of 9×9 PRMS array, (c) Bottom view of 9×9 PRMS array (d) S_{11} Plot and (e) Gain & AR Plot.

An array of 9 × 9 PRMS UC is constructed and placed at a height (hs) of 12 mm above the proposed PCA, forming a FP cavity called PRMS-PCA, as shown in Fig. 4.4, to enhance its gain. The dimensions of the PRMS UC are set to sq = 7.8 mm, w1 = 0.6 mm and t = 1 mm. The designed PRMS-PCA resonates from 9.8 GHz to 12.27 GHz, as shown in Fig. 4.4 (d), which almost covers resonant frequencies of the PCA. Since

designed PRMS have high reflectivity, i.e., its magnitude is between 0.80 and 0.88. The emanating CP waves from the PCA bounce back and forth in the formed cavity and depart the cavity with an equal phase, resulting in gain enhancement in the broadside direction. The enhanced gain for the designed PRMS-PCA is between 11.8 dBi and 16.4 dBi over the operating BW of 2.47 GHz. For the frequencies between 10 GHz and 10.8 GHz, a flat enhanced gain is observed. Overall, the gain has significantly enhanced for the operating BW of 2.47 GHz, as depicted in Fig. 4.4 (e).

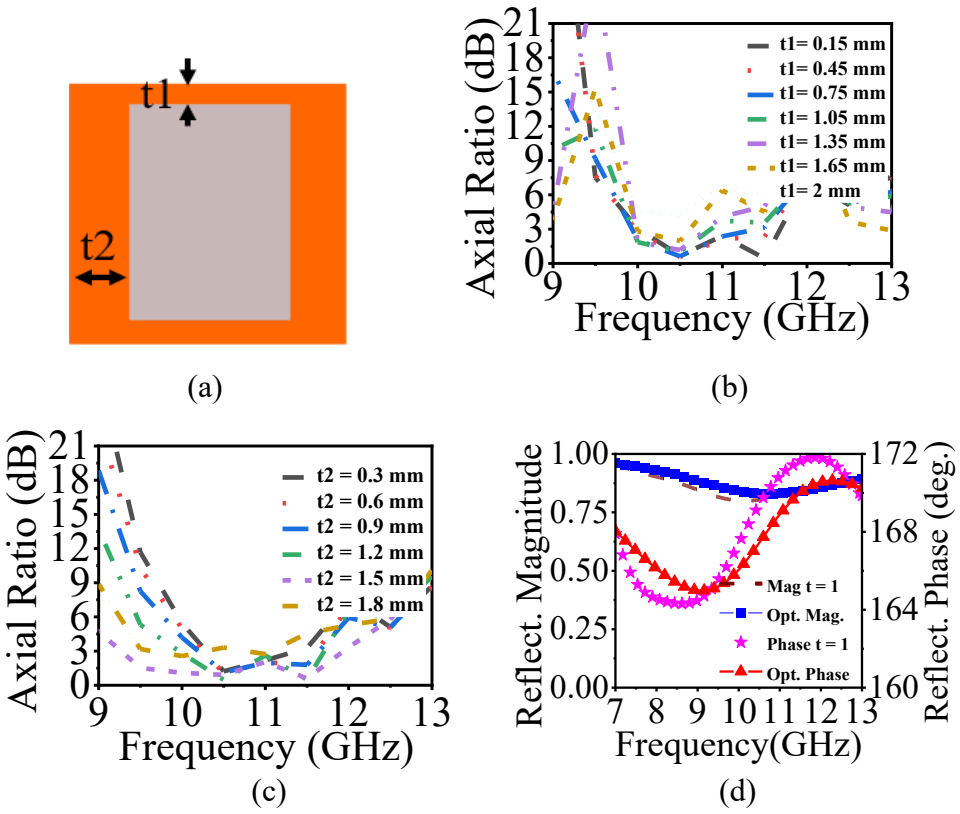

Fig. 4.5: (a) Optimised PRMS UC, (b) parametric analysis of t1 when t2 = 1 mm and (c) Parametric analysis of t2 when t1 = 0.18 mm, (d) Optimised Reflection Magnitude & Phase.

The ARBW of the PRMS-PCA is observed to be wider than that of the conventional PCA without the 9×9 PRMS array. The obtained ARBW below 3 dB, which corresponds to pure CP, is from 10 GHz to 11 GHz. This indicates an enhancement of 210 MHz of ARBW in addition to the PCA original ARBW, 790 MHz, thereby summing a total ARBW of 1 GHz for the designed PRMS-PCA. Moreover, within the frequency range of 11.1–11.5 GHz, the AR remains below 3.8 dB, while at 12 GHz it is 5.8 dB, as can be seen from Fig. 4.4 (e). These results verify that the incorporation of the proposed PRMS array not only substantially improves the gain of the PCA but also brings existing EP in the impedance BW closer to the pure form of CP. However, it is important to note that the ARBW below 3 dB does not fully envelop the entire impedance BW. Thus, further

design improvements are required to achieve a wideband pure CP across the complete impedance BW.

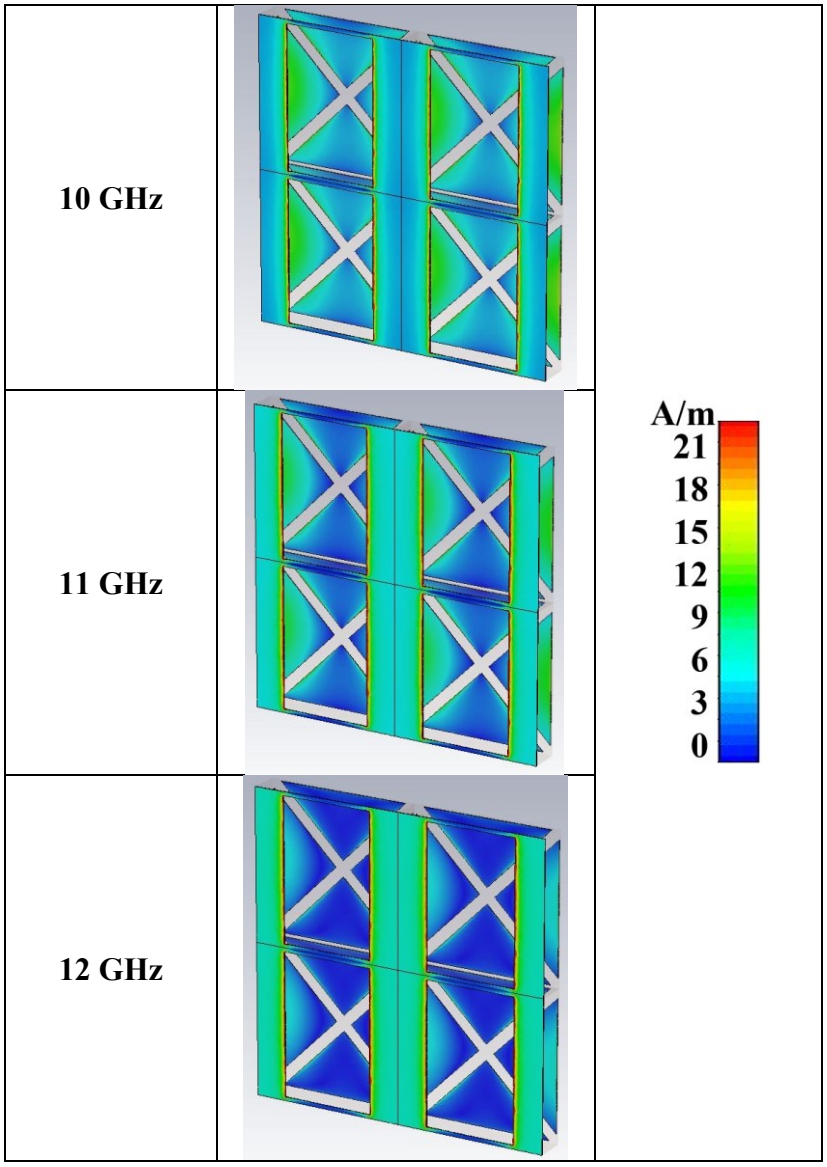

Fig. 4.6: Surface current distribution on the bottom side of optimised PRMS UC at frequencies 10 GHz, 11 GHz and 12 GHz.

To achieve the 3 dB ARBW enveloping or matching impedance BW, the PRMS UC needs to be modified. As mentioned earlier, the top layer of the PRMS is responsible for the positive phase gradience, and the bottom layer is responsible for the high reflectivity. This is the case where the orthogonal components' magnitudes are unequal, but the phase difference between them is 90º. Therefore, the bottom layer thickness (t) of

PRMS UC is optimised in the y and the x directions as t1 and t2, respectively. Consequently, the E-field components, E_θ and E_ϕ, magnitude is adjusted, resulting in their ratio equaling 1 and obtaining a pure form of CP.

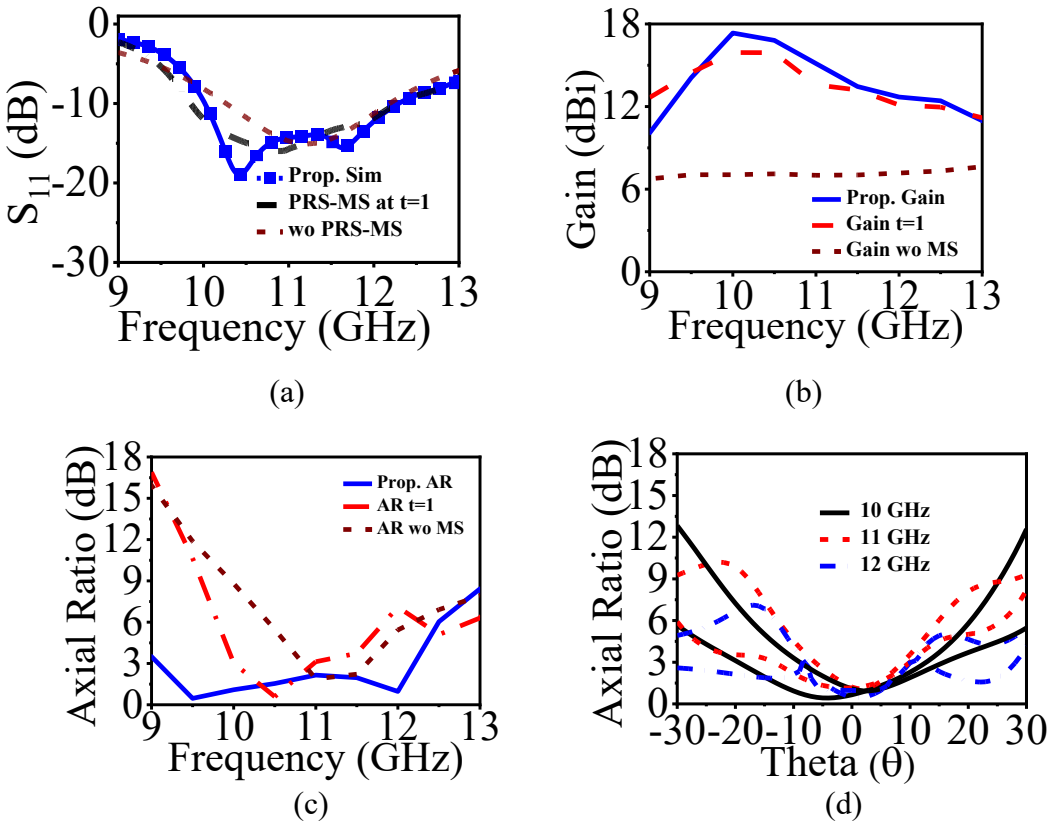

Fig. 4.7: Simulated results of the proposed PRMS-PCA when t1 = 0.2 mm, t2 = 1.6 mm (a) S11 plot, (b) Gain plot, (c) AR plot, and (d) Axial beamwidths at ϕ = 0º and 90º.

The optimised PRMS UC is shown in Fig. 4.5 (a). As UC is optimised, it becomes polarisation sensitive to the E-field components, E_θ and E_ϕ. To study and analyse it, the parametric analysis was conducted as shown in Fig. 4.5 (b) & (c). At first, t2 is set to 1 mm, and t1 is varied from 0.15 mm to 2 mm, then t2 is varied from 0.3 mm to 1.8 mm while t1 is set to 0.5 mm. Post parametric analysis, to result in 3 dB ARBW overlapping impedance BW, the optimum values for t1 & t2 are found to be 0.2 mm & 1.6 mm, respectively. To ensure that with this optimisation, the magnitude and phase response of the PRMS UC is not affected, hence, PRMS UC (t1 = 0.2 mm & t2 = 1.6 mm) with its initial stage, PRMS UC (t = 1 mm) responses comparison are shown in Fig. 4.5 (d). This plot shows that both responses are almost similar. As mentioned in the earlier section 4.2.1, the bottom layer provides high reflectivity; the outer dimension of the PRMS UC is responsible for maintaining the reflection magnitude between 0.82 and 0.88, which signifies that enhanced gain will not be adversely affected. The inner ring dimensions are

responsible for the polarisation sensitivity. Hence, the inner ring will constitute a higher amount of surface current, as depicted in Fig. 4.6, and the AR can be optimised as required, as shown in Fig. 4.5 (b) & (c).

The simulated results of the modified PRMS-PCA are shown in Fig. 7. The modified antenna resonates from 9.9 GHz to 12.31 GHz, and the maximum enhanced gain is 17.1 dBi at 10 GHz. Fig. 4.7 also shows the comparison of the modified antenna with its previous stage, depicting that the resonance is not affected and the gain is improved because the cross polarisation levels are reduced at 10 GHz.

The optimised 3 dB ARBW is obtained from 9.3 GHz to 12.21 GHz, i.e., 2.91 GHz. The ARBW is significantly increased from 790 MHz to 1 GHz when PRMS UC have t = 1 mm and from 1 GHz to 1.91 GHz for the modified PRMS UC. This implies that optimised ARBW from 9.3 GHz to 12.21 GHz almost overlaps the impedance BW 9.9 GHz to 12.31 GHz, as shown in Fig. 4.7 (c). The axial beamwidths are presented in Fig. 4.7 (d), which shows that the axial beamwidths are ±15° at ϕ = 0° and 90°.

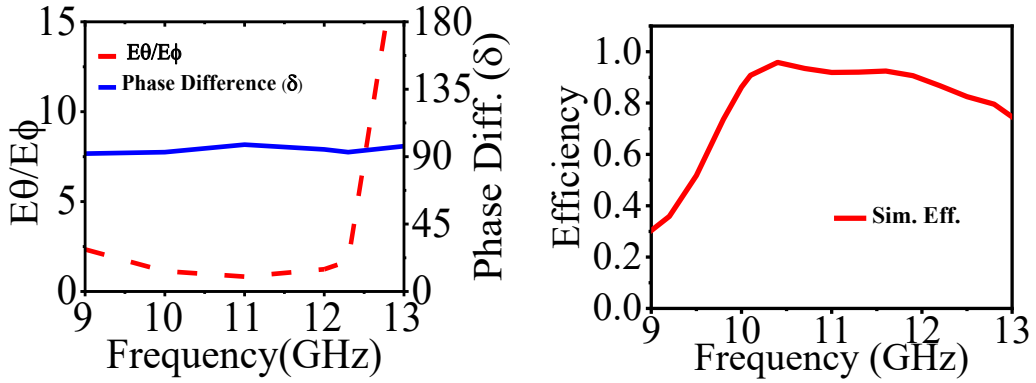

(a) (b)

Fig. 4.8: (a) E-fields components magnitude ratio and phase difference plot, and (b) Simulated Total efficiency.

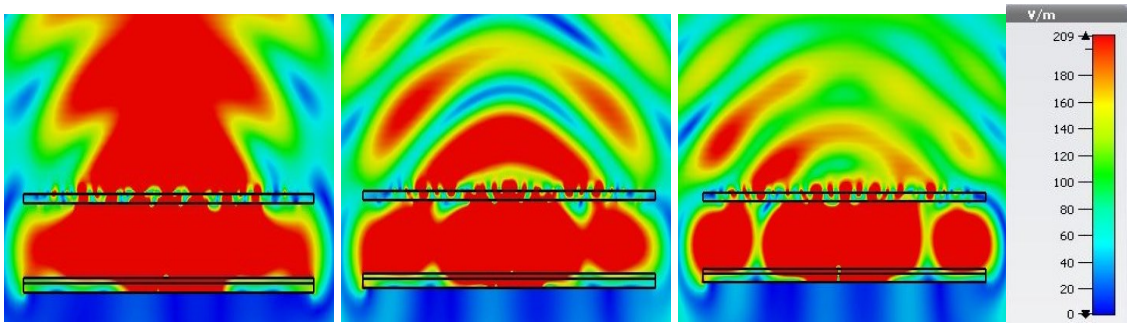

(a) (b) (c)

Fig. 4.9: E-Field plots for modified PRMS-PCA (a) 10 GHz, (b) 11 GHz, and (c) 12 GHz.

To verify ARBW overlapping impedance BW, as per Eqn. 4.5, the ratio of magnitudes of E-field components should be 1 or closer to 1, and the phase difference between them will be + 90º for RHCP waves and − 90º for LHCP waves. Fig. 4.8 (a) shows that the mag (E_θ)/mag (E_ϕ) is 1 and $\measuredangle E_\theta - \measuredangle E_\phi = +90^\circ$ for the frequencies from 9.9 GHz to 12.21 GHz. The positive phase difference of 90º between the two E-field components indicates that the modified FPCA is indeed RHCP. The simulated total efficiency is shown in Fig. 4.8 (b). The E-field plots for the modified PRMS-PCA at frequencies 10 GHz, 11 GHz, and 12 GHz are shown in Fig. 4.9.

A parametric analysis for the height 'hs' is carried out for the modified PRMS-PCA. The height 'hs' is varied from 8 mm to 20 mm, and it is found that the predetermined height of 12 mm, which corresponds to 0.39 λ_0 at 9.9 GHz (the lowest resonating frequency) has resulted in optimum gain and wide ARBW. The parametric analysis results are shown in Fig. 4.10 (a), (b) & (c). Therefore, modified PRMS-PCA is considered the proposed CP antenna with high gain and ARBW overlapping impedance BW.

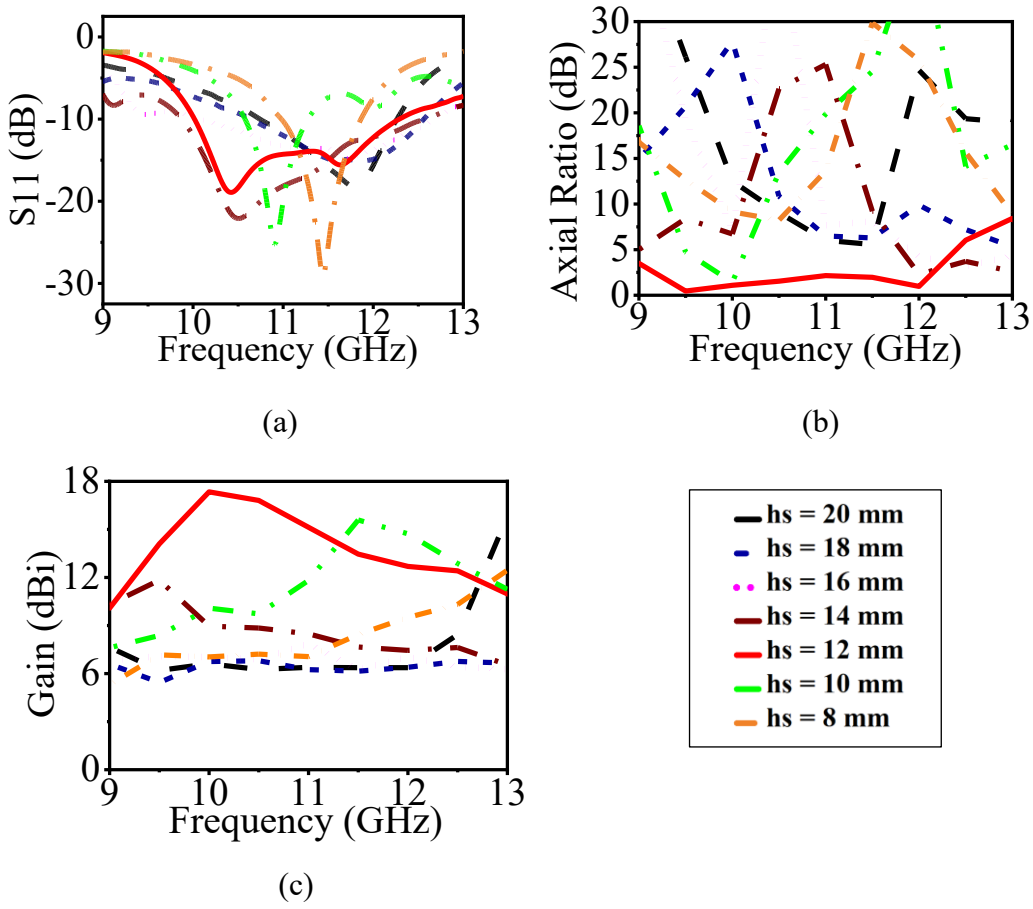

Fig. 4.10: Results for the parametric analysis of height 'hs': (a) S_{11} Plot, (b) AR Plot, and (c) Gain Plot.

4.3 Measured Results and Discussion

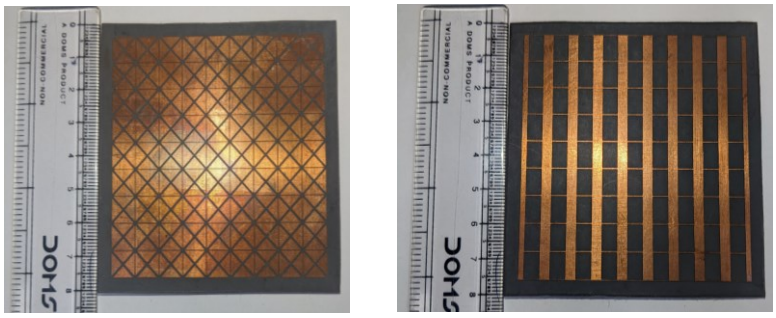

(a) (b)

(c)

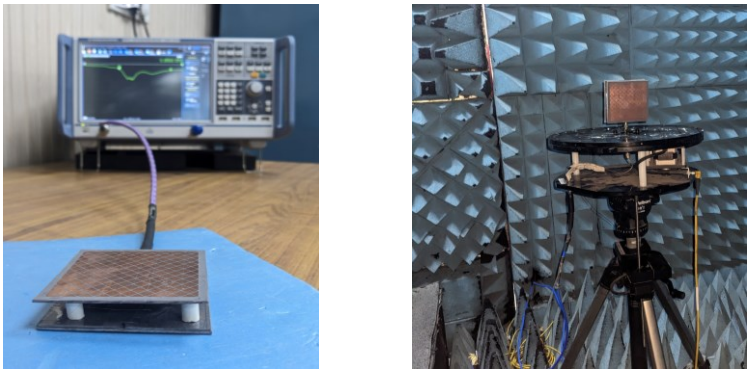

(d) (e)

Fig. 4.11: Fabricated prototype of PRMS-PCA (a) Top view of the PRMS array, (b) Back view of the PRMS array, (c) Top view of the PCA, (d) S_{11} testing, (e) Radiation patterns measurement.

With satisfactory results, the proposed antenna's prototype is fabricated. Substrate Rogers RT duroid 5880 with a dielectric constant of 2.2, of two thicknesses, h1 = 1.55 mm and h2 = 0.79 mm, are used. The chamfered edge patch is on the top side of layer 2,

and the feed line is on the top of layer 1, which is backed by copper ground. The 9×9 PRMS array is also fabricated using Rogers RT duroid 5880 of height 1.55 mm. The PRMS array is placed on the fabricated PCA using four air spacers of height hs = 12 mm as shown in Fig. 4.11 (a) to (d). The prototype of PRMS-PCA is tested on the VNA, as presented in Fig. 4.11 (d) and radiation patterns are measured in the anechoic chamber as depicted in Fig. 4.11 (e).

The measured and simulated S_{11} of the proposed PRMS-PCA are plotted in Fig. 4.12 (a), which shows that the fabricated prototype resonates from 9.85 GHz to 12.4 GHz, which is in good agreement with the simulated resonating frequencies 9.9 GHz to 12.31 GHz. The measured and simulated gain & AR are compared in Fig. 12 (b). The maximum measured gain is 15.2 dBi, and the measured 3dB ARBW is attained from 9.35 GHz to 12.3 GHz as shown in Fig. 4.12 (c). The mismatches in the simulated and measured results are attributed to fabrication tolerance and human error while carrying out measurements. From these results, it can be seen that measured ARBW is from 9.35 GHz to 12.3 GHz, which overlaps the impedance BW from 9.85 GHz to 12.4 GHz.

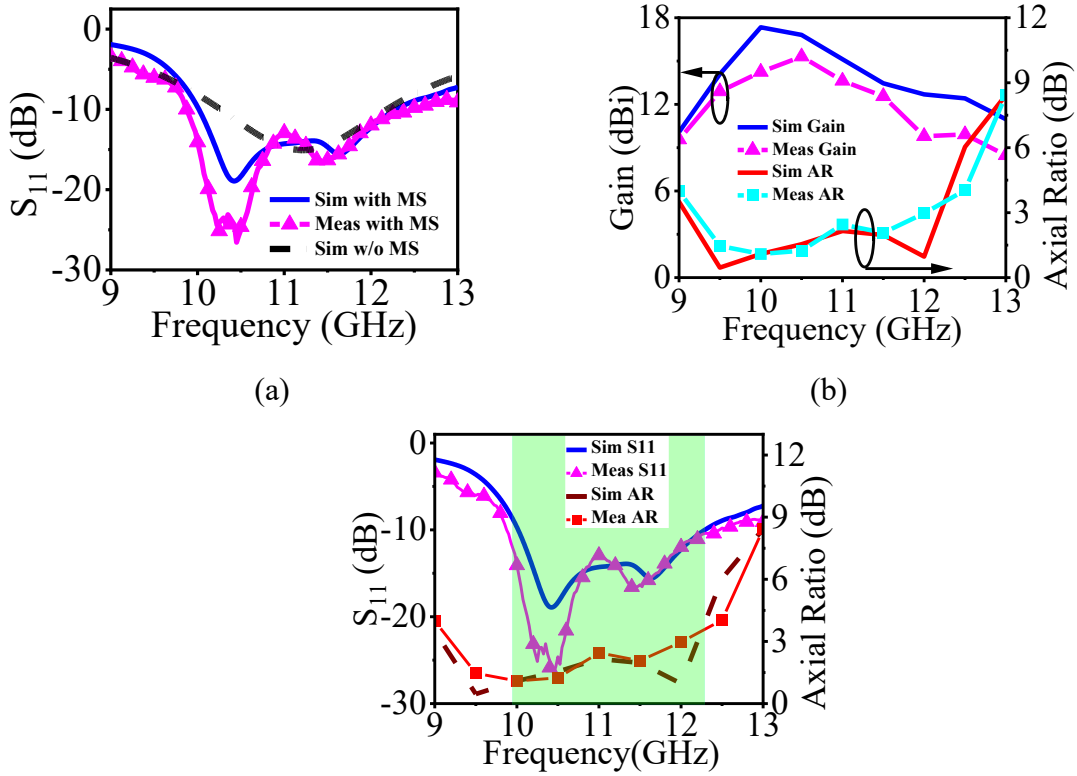

Fig. 4.12: Comparison of simulated and measured results of the proposed antenna, PRMS-PCA, (a) S_{11}, (b) Gain and AR plot, (c) ARBW and S_{11} plots.

The Radiation patterns of the proposed PRMS-PCA are measured in the XZ-plane and YZ-plane at 10 GHz, 11 GHz and 12 GHz, as shown in Fig. 4.13. The prototype antenna has a high gain at 10 GHz, and the cross-polarisation levels are below -15 dB. From 11 GHz onwards, side lobes are attained with a high magnitude, which leads to a lower gain at 11 GHz and 12 GHz than at 10 GHz. The measured patterns are almost identical to simulated patterns, implying good agreement between simulated and measured results.

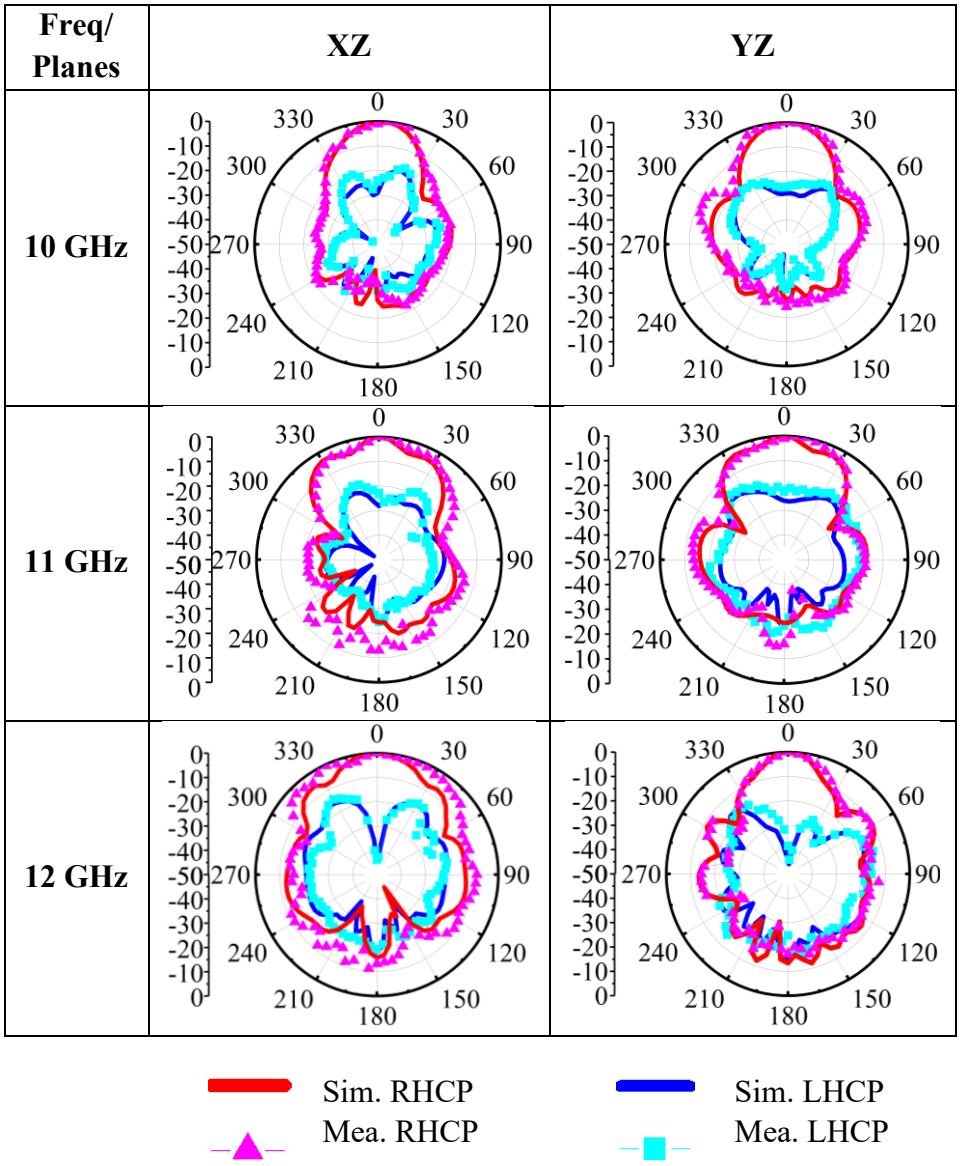

Fig. 4.13: Radiation patterns for the proposed PRMS-PCA in XZ and YZ planes.

Table 4.1: Comparison of reported FPCA with proposed PRMS-PCA.

Ref.	Tech.	Size (λ_0^2)	Ant. Prof. (λ_0)	Freq (GHz)	% IBW	3 dB ARBW (GHz)	% AR BW	Max Gain (dBi)
[199]	PRS	2.4× 2.4	0.45	5.23-7.2	31.7	5.45-6.25	13.7	13.3
[200]	PRS	1.65× 1.65	0.6	8-9.8	20	8.35-8.95	6.7	14.6
[201]	PRS	2.7× 2.7	0.5	9.3-11.2	18.5	9.6-10.2	9.8	12.3
[188]	PC-FPC	2.9× 2.9	0.4	9.6-10.8	14.92	9.4-10.8	13.86	18.2
[189]	PC-FPC	2.62× 2.62	0.6	6.29-6.71	6.46	6.55-6.76	3.16	9.26
[190]	PRS	1.64× 1.64	0.6	11.55-14.8	24.7	11.97-12.6, 14.09-14.63	5.58, 2.95	12.4-13.8
[191]	PC-FPC	2.62× 2.62	0.58	10.5-10.78	2.63	10.65-10.74	1.1	11.5
[193]	FPC-Anisotropic medium	Radius =1.6	1.1	9.65-10.46	8	9.6-10.27	6.74	19
[202]	MS	1.45× 1.45	0.08	8.7-9.8	11.9	8.51-9.68	12.86	8.9
[203]	MS	1.45× 1.45	0.057	6.1-7.2	16.5	6.26-6.94	10.3	9.36
[204]	PC-FPC	1.02× 1.02	0.44	10.7-15.8	38.5	11.5-14.3	21.7	11.7
[205]	PC-FPC	2.89× 2.89	0.43	9.85-10.12	2.70	9.65-10.5	8.43	13.1
[206]	PC-MS	0.91× 0.86	0.11	4.48-8.39	60.76	4.43-6.52	38.17	8.5

[207]	MS	0.79× 0.77	0.02 3	8.76-10.74	20.3 0	8.9-10.48	16.3 0	8.8
[208]	PC-MS	1.75× 0.67	0.07	9-11.5	24.3 9	10.1-10.7	5.77	14.1
This work	**PRS**	**2.6× 2.6**	**0.52**	**9.9-12.31**	**21.7**	**9.9-12.21**	**20.9**	**17.1**

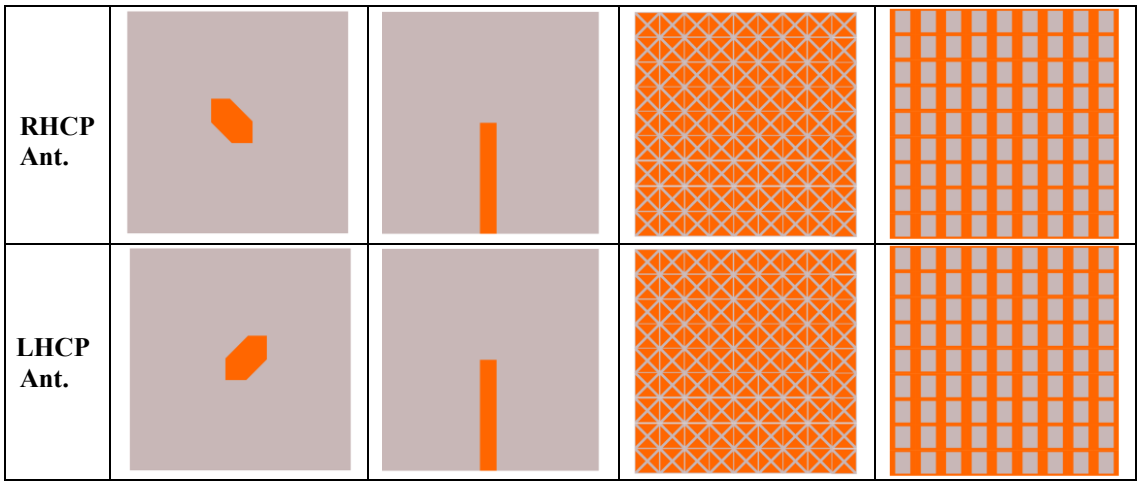

Fig. 4.14: Structural difference between the proposed RHCP and new LHCP PRMS-PCA.

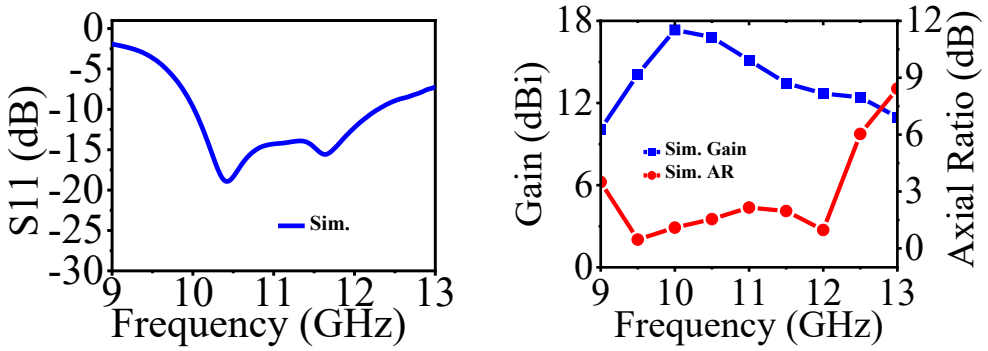

(a) (b)

Fig. 4.15: Simulated results for the LHCP PRMS-PCA (a) S_{11} plot, (b) Gain and AR plot.

Table 4.1, compares the proposed PRMS-PCA and reported CP antennas in terms of techniques utilised, size of antenna, impedance BW, ARBW, and maximum gain. The table presents the proposed PRMS-PCA, which provides impedance BW of 2.41 GHz and ARBW of 2.31 GHz, overlapping it, which is challenging. Nonetheless, the proposed

antenna design structure is relatively less complex than the reported CP antennas. The proposed RHCP PRMS-PCA have a maximum enhanced gain of 17.1 dBi at 10 GHz. The antenna has a compact size of 80 × 80 × 15.89 mm³, which corresponds to 2.6 λ_0 × 2.6 λ_0 × 0.52 λ_0 (λ_0 is free space wavelength at 9.9 GHz).

Lastly, the design and analysis of RHCP PRMS-PCA are presented. With a small structural change, PRMS-PCA can emit LHCP waves instead of RHCP waves. To design an LHCP antenna, chamfering needs to be done on the opposite diagonal corners, as with the RHCP PCA, as shown in Fig. 4.14. The PRMS FP cavity for the LHCP PRMS-PCA will remain the same as the RHCP PRMS-PCA. The LHCP PRMS-PCA is simulated, and Fig. 4.15 shows the S_{11} of the new LHCP antenna with gain and ARBW. Fig. 4.14 shows the simple design approach to attain RHCP or LHCP in the antenna with high gain and wide ARBW overlapping the impedance BW. It also makes the designed RHCP or LHCP antenna a strong candidate for satellite and 5G communication applications.

4.4 Summary

In this chapter, A PRMS array is designed and experimentally validated to enhance both the gain and the ARBW of an RHCP PCA. The wide ARBW is realised through the conversion of EP waves into CP waves by optimising the PRMS unit cell. The implemented FP cavity has a height of 12 mm and incorporates a 9 × 9 PRMS array, which is integrated with the PCA. The overall antenna size is only 80 × 80 × 15.89 mm³. The proposed PRMS-PCA exhibits a resonant frequency range from 9.9 GHz to 12.31 GHz, maintaining an AR below 3 dB from 9.9 GHz to 12.21 GHz. This shows ARBW of 2.31 GHz, which closely matches its 2.41 GHz impedance BW. Compared to the simple PCA, the ARBW improves from 790 MHz to 2.31 GHz, while the gain has enhanced from 7.3 dBi to 17.1 dBi at 10 GHz. Furthermore, the proposed structure enables both RHCP and LHCP operation with minor modifications in the PCA structure. These parameters suggest the proposed RHCP or LHCP antenna design may be suitable for 1U CubeSat applications.

Chapter 5

Phase Gradient Metasurface Lens Antenna for 12 GHz 5G Communication

5.1 Introduction

In the previous chapter, Satellite Communication (SatCom) for non-terrestrial 5G communication and the development of the SatCom antenna with wide ARBW were discussed. In this chapter, the FCC in 2021 recommended the 12 GHz band (12.2 GHz to 12.7 GHz) for terrestrial 5G communication. This band is called the Multichannel Video *Distribution Service (MVDDS)*, which provides TV broadcast and internet connectivity from terrestrial transmitters to consumers [209]. Therefore, for p2p terrestrial communication, a directive antenna could be required. These antennas are supposed to have a low profile with high directivity. Focusing lenses (FL) play an important role in the gain enhancement of the low-frequency and high-frequency antennas, as they provide directive beams, a wide impedance bandwidth (BW) and support multiple polarisations [69]. Due to this, extensive research is carried out on MMTs/MSs lenses to generate focused beams, and Phase Gradient Metasurfaces (PGMS) lenses have proved their potential multi-purpose functionality such as multi-beams [210], beam steering/scanning [211], [129], wireless power transfer [212], reflector [213] and gain enhancement [76].

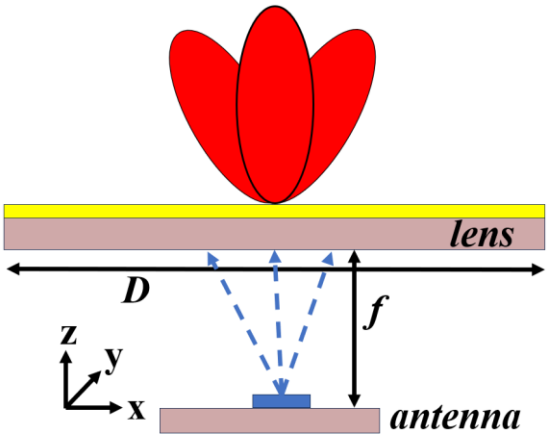

Fig. 5.1: Schematic diagram of the focusing lens with a fed source (antenna).

Strategically placed PGMS UC in the form of an array provides a distinct phase shift or time delay to the incoming EM-waves from the source or antenna, which then forms a desired radiation beam [214], as shown in Fig. 5.1. Higher frequencies as mm-Wave frequencies are an inherent provider of large impedance BW with their

compact size. To address low gain and high propagation losses in the mm-Wave frequencies, PGMS-FL are utilised to enhance the gain of the antenna. Due to the small wavelengths at mm-Waves, the size of the PGMS-FL with the antenna is also compact [129], [76], [215]. However, lower frequencies offer better coverage than mm-Waves, and they have high propagation characteristics. Therefore, in recent years, researchers have been exploring using the 12 GHz band for terrestrial 5G communication [209].

A PGMS array is utilised for beam scanning of the wideband antenna, and the maximum gain reaches up to 14 dBi. To scan or steer the beam, the PGMS array is moved in the x-direction to scan the beam in the x-direction, and later the array is moved in the y-direction to scan the beam in the y-direction [216]. Two different MSs are designed and analysed to achieve a phase gradience of more than 360º with a high transmission coefficient. Although the reported MSs have wide BW and high efficiency, but the source antenna impedance BW is only 400 MHz [217]. A multilayered PGMS array is reported, which results in a 3 dB gain variation [218]. A CP antenna with a PGMS lens has a wide impedance BW, ARBW is 789 MHz. However, dual layer lens have an air gap of 9.5 mm between the two layers of substrate. Also, the dual layer MS has attained a phase variation is just 46.2º, which leads to phase quantisation error and results in low gain and efficiency [219]. Similar to a Metal dish as a reflector, a PGMS reflectarray is used for gain enhancement and to change the polarisation from LP to EP at 5 GHz, and at 11 GHz, the MS design widens the ARBW. However, the need to convert LP to EP at 5 GHz is not justified, and at 11 GHz, the impedance BW is 620 MHz with a gain of 18 dBi [220]. Another PGMS reflectarray antenna has an impedance BW of 1 GHz, and the maximum gain attained at 14.5 GHz is 17.47 dBi. However, the gain variation is more than 2.5 dBi [221]. A PGMS UC have the BW of 1.2 GHz, and a phase variation of more than 360º is achieved through five distinct designs of MS. However, the impedance BW is 850 [222]. The *f/D* is maintained ≤ 0.5, which ensures a low profile, where f and D are the focal length and Diameter, respectively. Different PGMS-FL are fed with horn antennas; horn antennas have a large size and built-in high directivity. In these antennas, *f/D* is maintained ≤ 1 [214], [223], [224], [225], and [226]. A large *f/D* leads to a large profile and a bulky antenna structure. Also, a small value of *f/D* may not be applicable since multiple reflections or coupling between the antenna and lens should be considered while designing the antenna. The above structures either have narrow impedance BW, since the source antenna has narrow BW, or the antenna size is too large to install as a small 5G terrestrial base station.

After identifying limitations in the existing literature, it is essential to design a low profile, high gain antenna with wide ARBW to link the terrestrial base to the satellite, and it can also be conveniently integrated into compact 5G base station units. In this chapter, above mentioned limitations are addressed by designing a thin profile PGMS-FL to enhance the gain of the CP antenna. The lens profile is 0.124 λ_0, and *f/D* is maintained to 0.2 to ensure low height structure. To build the PGMS-FL, five variants of the proposed PGMS UC are chosen to attain a phase gradience of 0º-182.68º, i.e, 0 to π in radians. By incorporating a lens to the antenna, for the impedance BW from 10.42 GHz to 13.26 GHz,

the enhanced gain ranges from 15.63 dBi to 17.7 dBi with a gain variation of 2.07 dBi, resembling almost flat gain. The 3 dB AR is observed from 10.51 GHz to 11.7 GHz.

5.2 Design and Analysis of the PGMS UC and CP Antenna

5.2.1 Design of PGMS UC

The proposed PGMS UC is a dual layered Complementary Single Circular Ring Resonator (CSCRR), designed on the top side of the substrate with a dielectric constant of 2.2, having a dielectric thickness of 0.79 mm. Both layers have identical designs on the top side substrate to attain high efficiency and polarisation compatibility. An air gap of 2 mm is maintained between UC layers to result in a UWB transmission BW of 8 GHz from 7 GHz to 15 GHz. The design of CSCRR is shown in Fig. 5.2 (a) to (c).

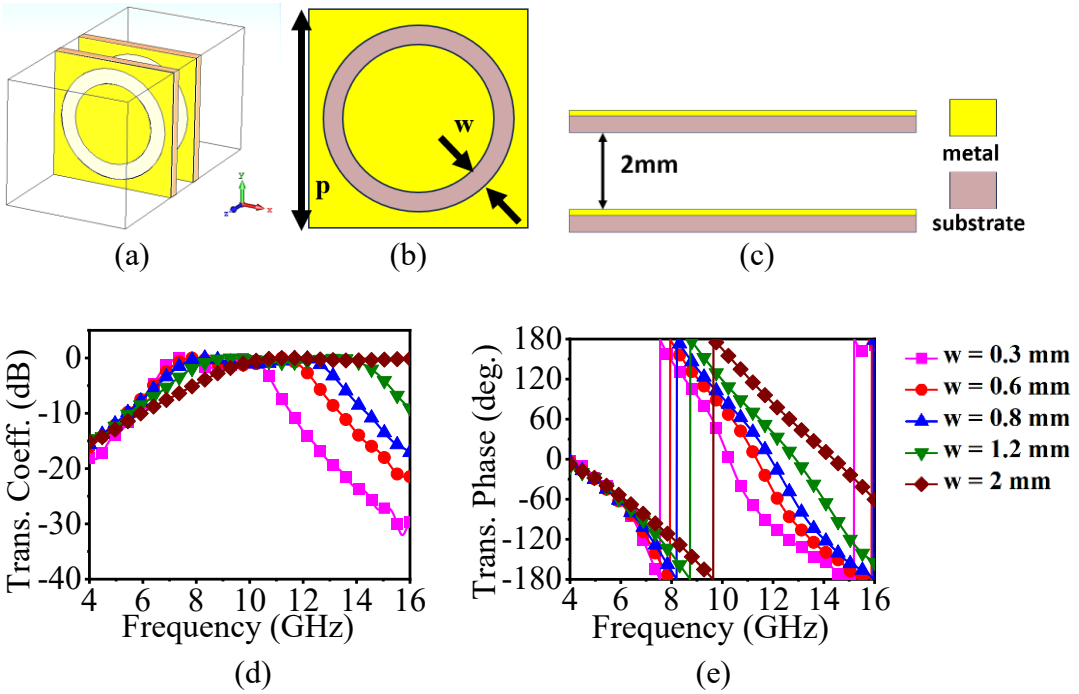

Fig. 5.2: Design and responses of the CSCRR UC, (a) Simulation setup, (b) Front view, (c) Side view, (d) Transmission coefficient and (e) Transmission phase.

To simulate CSCRR PGMS UC, the boundary conditions are applied in the x and y-directions as PEC and PMC, respectively. As the UC is symmetric, the boundary condition directions can be switched between the x and y directions. The UC is excited in the z-directions using two waveguide ports to analyse the S_{11} and S_{21} responses. The CSCRR has inductance due to the metal circular patch and metal boundary, and capacitance generated from the complementary circular ring slot; both can be changed with respect to the change in width '*w*' and the '*air gap*'. This means the S-parameter response can be affected by a change in the UC dimensions. Accordingly, the phase response of the CSCRR UC 'Φ' is also a function of the linear change of dimension of

the UC, i.e., with the change in the complementary ring width '*w*', the resonance of the PGMS UC is changed, and so does the '*Φ*', as presented in Fig. 5.2 (d) & (e).

To obtain the transmission phase gradience of 180º, the '*w*' is varied from 0.3 mm to 2 mm of the CSCRR UC. As a result, at 11 GHz, the transmission phase gradience ($d\Phi/dr$) of 0º-182.68º is attained, as shown in Fig. 5.2 (e). The size of the proposed UC is 8×8 mm², which is equivalent to 0.34 λ_0×0.34 λ_0 (lowest resonating frequency). The small UC size is chosen to avoid large grating lobes. As mentioned earlier, the transmission phase is a function of a linear change in the dimension. Fig. 5.3 (a) depicts an almost linear phase response for varying complementary ring width 'w' of the UC at the different frequencies. To verify the incidence stability of the UC, the UC is incident with the EM wave with different angles (θi), as shown in Fig. 5.3 (b).

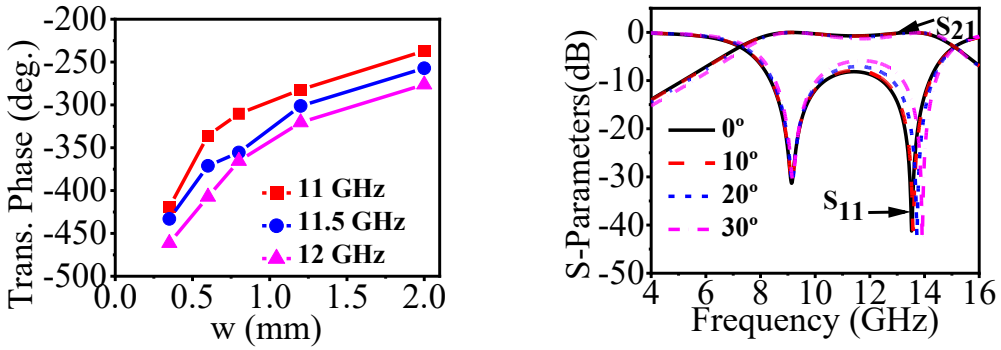

Fig. 5.3: (a) phase variance with the change in 'w' and (b) The TE and TM responses at different incident angles where w = 1.2 mm.

Different angles of incidence (θi) are also studied on the CSCRR UC, as shown in Fig. 5.3 (b). It depicts that the S11 and S21 responses are not affected by different angles of incidence. The TE and TM responses of the UC are going to be identical due to the symmetric geometry of the CSCRR UC. The TE and TM responses will be the same for different angles of incidence as shown in Fig. 5.3 (b). The proposed PGMS-FL supports any polarisation; this means, the proposed PGMS-FL is *polarisation-insensitive*. This feature of the proposed CSCRR UC is crucial for the circularly polarised waves, and it is leveraged for incident CP waves, as discussed in the further sections.

The spherical EM waves are transformed into plane waves as they pass through PGMS-FL. A phase discontinuity 'ϕ (x, y)' is introduced by each CSCRR UC, which results in the phase compensation in the planar PGMS-FL array. Thus, planar EM waves are emitted. Using Fermat's principle, the phase discontinuity 'ϕ (x, y)' can be calculated from Eqn. 5.1 given below [76],

$$\phi\,(x,y) \;=\; -\frac{2\pi}{\lambda}\left(\sqrt{(x^2+y^2)+f^2}-f\right)\pm 2\pi n \qquad (5.1)$$

where x and y are the UC coordinates on the planar array, and n = 0, 1, 2 … . Following Eqn. 5.1, a planar array for 15 × 15 UCs is formed of size 5.21 λ_0 × 5.21 λ_0, which acts as PGMS-FL, as shown in Fig. 5.4. In Table 5.1, the transmission phase at 11 GHz associated with the width 'w' of the proposed CSCRR UC is presented.

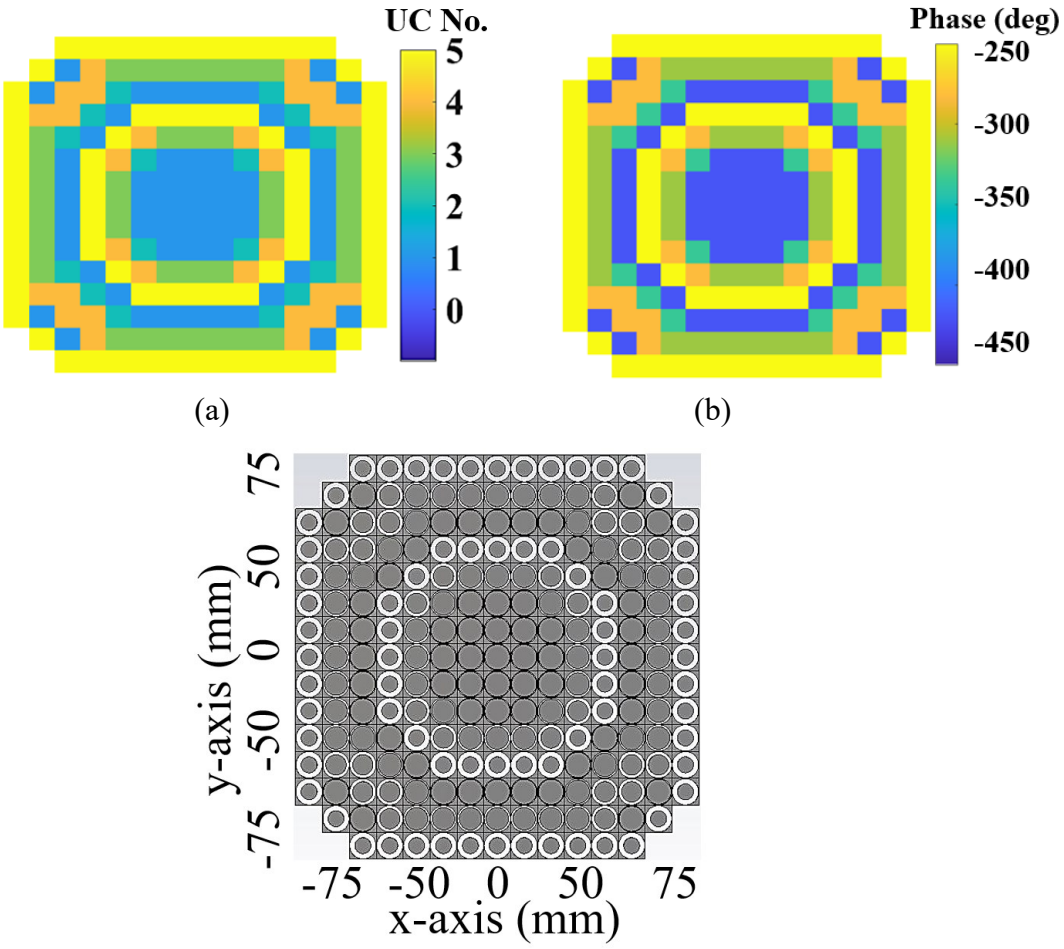

Fig. 5.4: A 15 × 15 proposed CSCRR lens array (a) Phase distribution, (b) Transmission phase distribution, (c) Top view of lens in the simulation setup.

The radial placement of CSCRR UCs produces a time delay (ΔT) through phase gradience for the incoming EM waves, as shown in Fig. 5.4. As the EM wave encounters the proposed PGMS-FL, the EM wave is deflected by an angle 'θ' forming a beam at the desired direction; here, the desired direction is the broadside direction at the centre of the lens. By altering only one dimension 'w' of the proposed CSCRR UC distinct phase shift from 0º to 182.68º is obtained, which introduces time delay (ΔT), calculated from Eqn. 5.2 and Eqn. 5.3 [227], [228],

$$Sin(\theta) = \frac{\lambda_0}{2\pi p}\Delta\phi \quad (5.2)$$

$$Sin(\theta) = \frac{\Delta T}{\Delta S}C_0 \quad (5.3)$$

where λ is calculated at 11 GHz, $\Delta\phi$ is a phase difference, ΔS is the centre-to-centre distance between two adjacent CSCRR UC. While C_0 is the speed of light and ΔS is 10 mm, which is constant for the proposed PGMS-FL. The time delay produced between the proposed UC is given in Table 5.2

Table 5.1: Transmission phase of the CSCRR UC at 11 GHz for different values of '*w*'.

Width 'w' (mm)	**Unit Cell**	**Trans. Phase (deg)**
0.3	UC1	-58.93
0.6	UC2	23.55
0.8	UC3	50.52
1.2	UC4	79.22
2	UC5	123.75

Table 5.2: Time delay generated by single CSCRR UC.

Phase difference between CSCRR PGMS-UC	**Phase difference (Δϕ) (deg)**	**Time delay (ΔT) (*p*s)**
UC2 – UC1	82.82	20.91
UC3 – UC2	26.97	6.76
UC4 – UC3	28.7	7.24
UC5 – UC4	44.53	11.24
UC5 – UC1	182.68	46.13

5.2.2 Design of CP Antenna

A CP antenna is chosen as the source to feed the proposed CSCRR PGMS-FL to verify the established hypothesis of source antenna compatibility. Similar to the source antenna in *Chapter 4*, A PCA of size 50 × 47 mm^2 with a patch whose diagonal edges are chamfered by 2.5 mm to produce RHCP waves is a source to the proposed PGMS-FL.

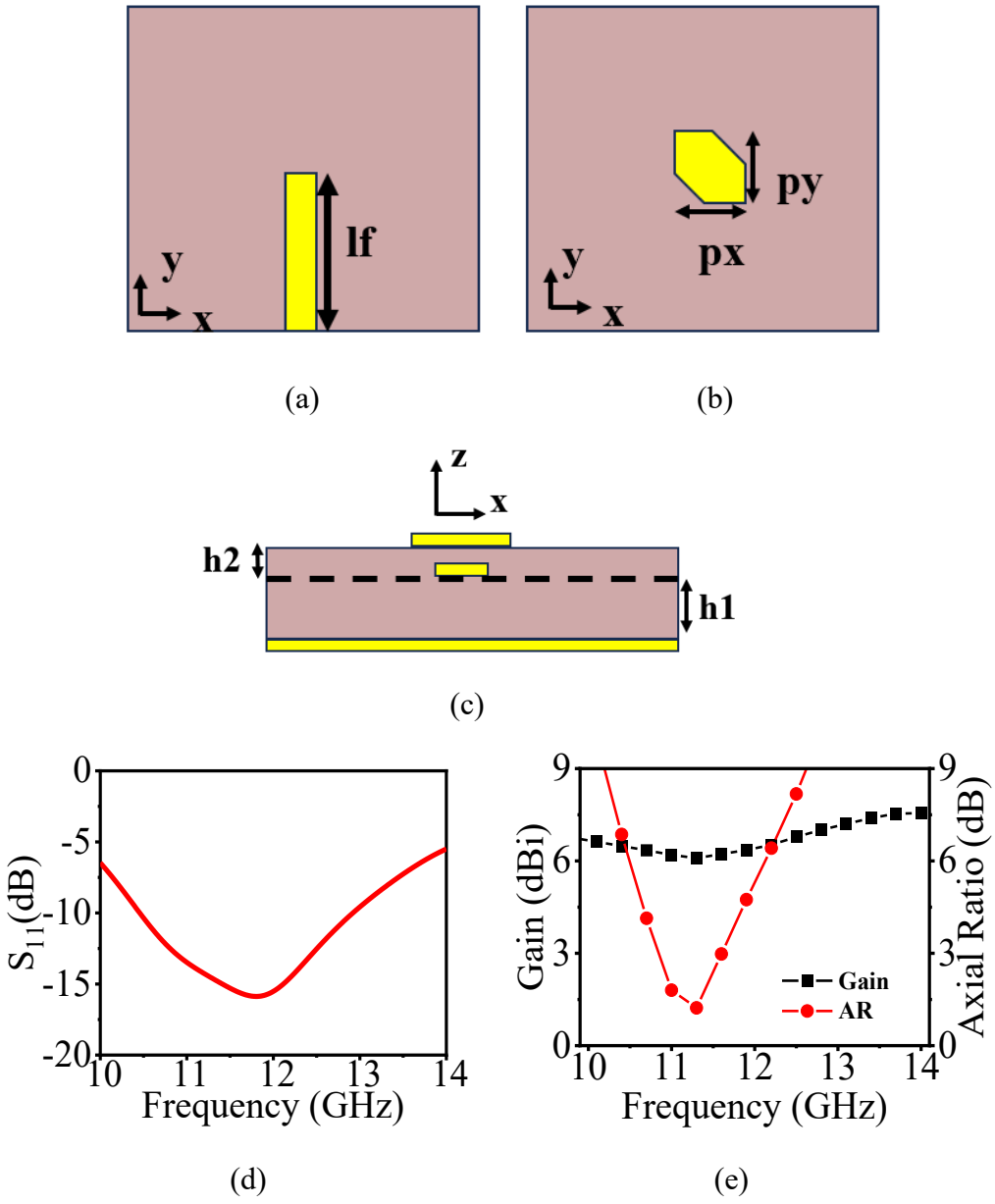

Fig. 5.5: CP source antenna (a) Patch, (b) Microstrip line, (c) Side view, (d) S_{11} plot, (e) Gain plot & AR plot, (f) (px = py = 8 mm and lf = 25.5, all dimensions are in mm).

The PCA is designed on the substrate RT Rogers 5880 with two heights h1 = 1.55 mm and h2 = 0.79 mm as shown in Fig. 5.5 (a) to (c). Both heights have the same substrates with an identical dielectric constant to maintain high efficiency in the antenna structure. The designed PCA has a resonance from 10.42 GHz to 12.92 GHz as shown in Fig. 5.5 (d), covering MVDDS frequencies. The ARBW is 770 MHz, from 10.83 GHz to 11.60 GHz, and the gain of the CPA is between 6.09 dBi and 6.7 dBi, as shown in Fig. 5.5 (d). The radiation patterns in the XZ-plane and YZ-plane at 11 GHz are shown in Fig. 5.6 (a) & (b). The HPBW in the XZ-plane and YZ-plane are 105º and 114.8º, respectively. This shows that the CPA has a wide HPBW in both planes. To generate focused beams and directive patterns, the proposed PGMS-FL needs to be integrated with the designed CPA.

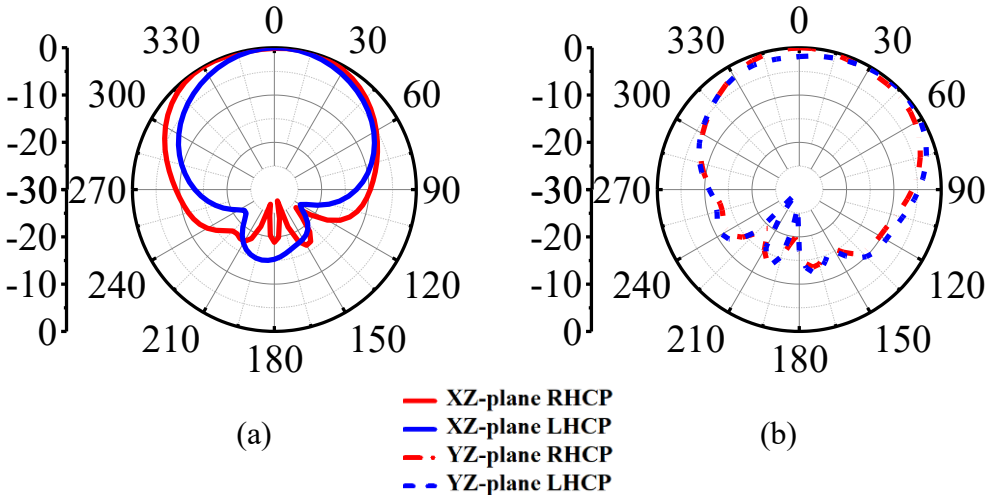

Fig. 5.6: (a) Normalised gain patterns in XZ-plane at 11 GHz, and (b) Normalised radiation pattern in YZ-plane at 11 GHz.

5.3 Proposed PGMS-FL Antenna

The proposed PGMS-FL is integrated with the CP-PCAS for gain enhancement and directive beams. The assembly of the proposed gain enhanced antenna is shown in Fig. 5.7 (a). The FL array is placed at a height or focal distance (f) of 30 mm from the CP-PCA. This distance is equivalent to 0.124 λ_0, and the arrangement results in the *f/D* as 0.2, making this design a compact antenna. The proposed PGMS-FL PCA resonates from 10.42 GHz to 13.26 GHz as shown in Fig. 5.7 (b). The dimensions of the patch, px, py and chamfered edges were optimised to 7.8 mm, 8 mm, and 2.8 mm, respectively, to achieve the desired resonance and ARBW. The reason for the optimisation was the coupling between the PGMS lens and source CP-PCA [80].

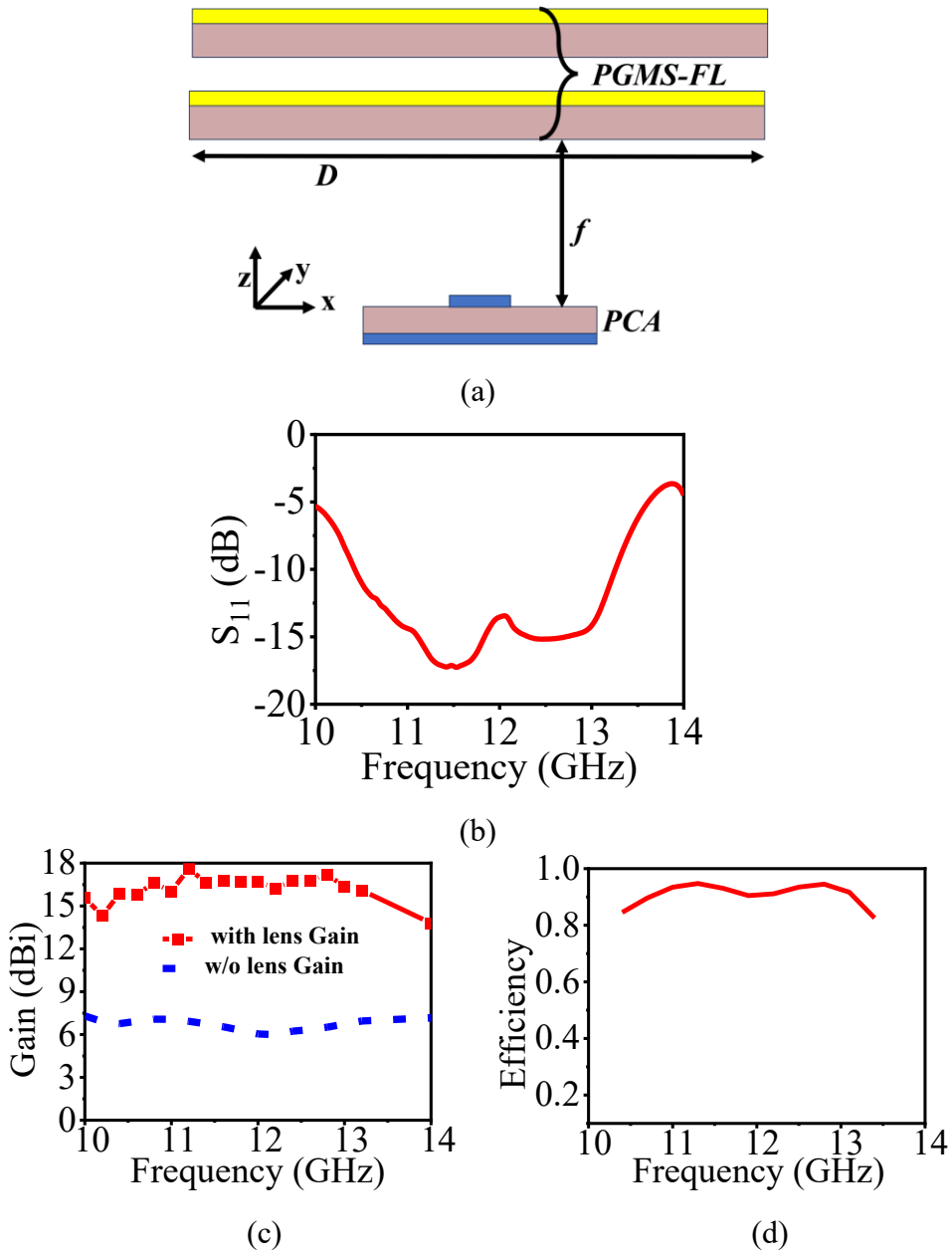

Fig. 5.7: Proposed gain enhanced PGMS-FL antenna (a) Assembly side view, (b) S_{11} plot, (c) Gain plot, and (d) Total efficiency plot.

Since the PCA is the RHCP antenna, the E-field components in the x-direction and y-direction may be equated from the Eqn. 5.4 & Eqn. 5.5 given below,

$$\boldsymbol{E}(t)=\frac{E_0}{\sqrt{2}}[E\hat{x}+E\hat{y}] \tag{5.4}$$

$$\boldsymbol{E}(t)=E_0[\hat{x}+j\hat{y}]e^{-i(kz+\omega t)} \tag{5.5}$$

Assuming PGMS-FL with '$N \times N$' array can add phase gradience to incoming RHCP waves from the PCA to deflect waves by the angle 'θ' for desired beamforming. Therefore, from Eqn. 5.2, the Eqn. 5.5 may be rewritten as [229], [230],

$$\boldsymbol{E}(t) = \boldsymbol{E}_{RHCP}(t) \sum_{n=0}^{N} e^{-in\left(\frac{d\Phi}{dr} - \Delta\phi\right)} \tag{5.6}$$

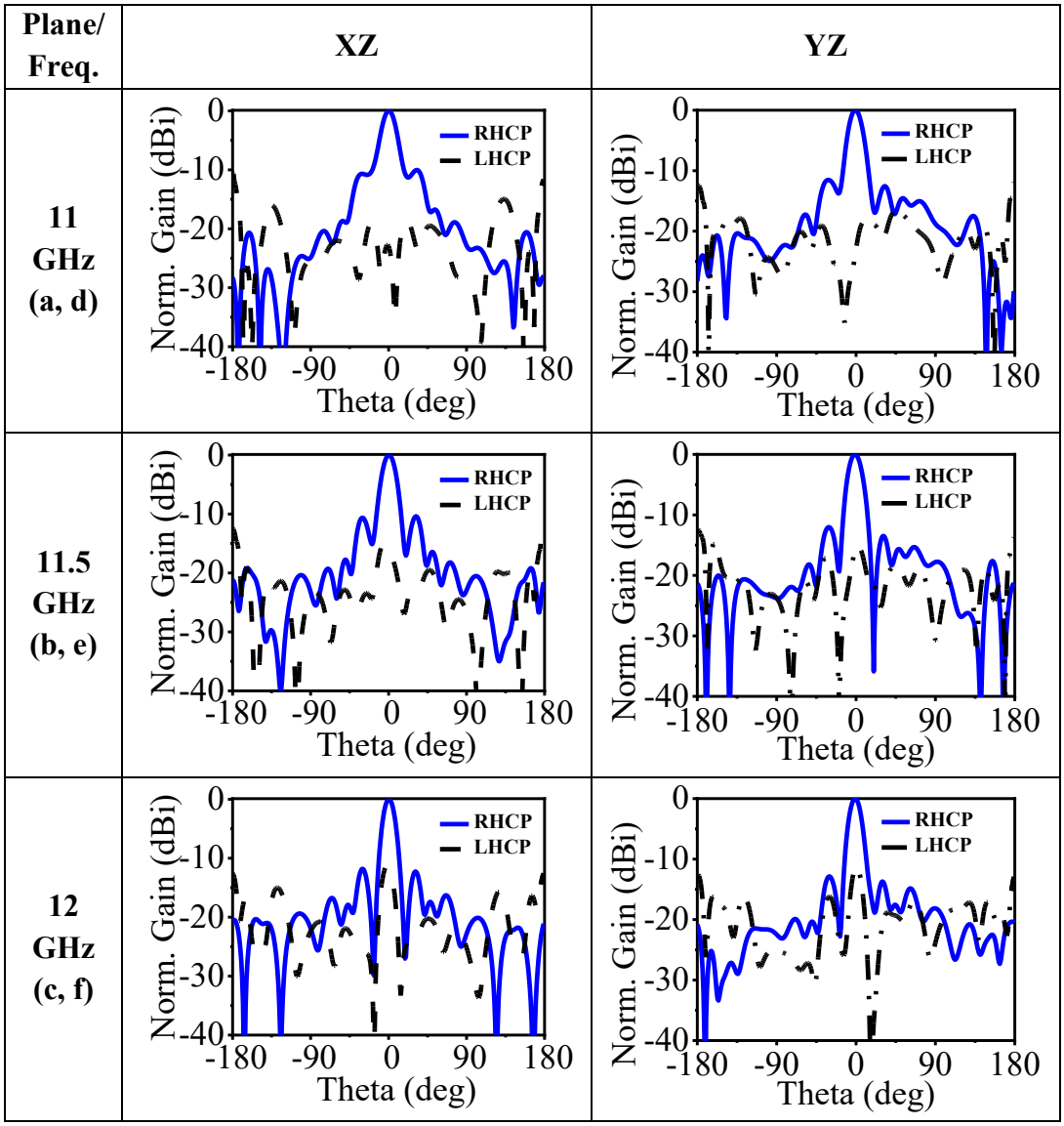

Fig. 5.8: 2D radiation patterns at 11 GHz, 11.5 GHz, and 12 GHz in the xz-plane (a, b, & c) and yz-plane (d, e, & f).

The gain of the CP-PCA is enhanced dramatically by utilising PGMS-FL, as shown in Fig. 5.7 (c). For the operating frequencies 10.42 GHz to 13.26 GHz, the gain has increased by almost 10 dB. The proposed PGMS-FL PCA has a maximum gain attained is 17.7 dBi, from 6.09 dBi at 11.2 GHz. The enhanced gain resembles a flat gain with a gain variation of only 2.07 dB; the enhanced gain varies between 15.63 dBi and 17.7 dBi. The simulated total efficiency is plotted in Fig. 5.7 (d), which depicts the efficiency for the resonating frequencies that lie between 87% and 92%.

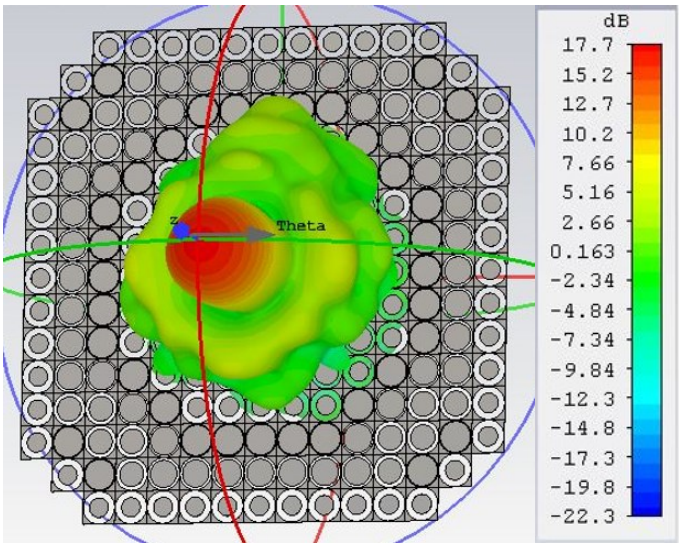

(a)

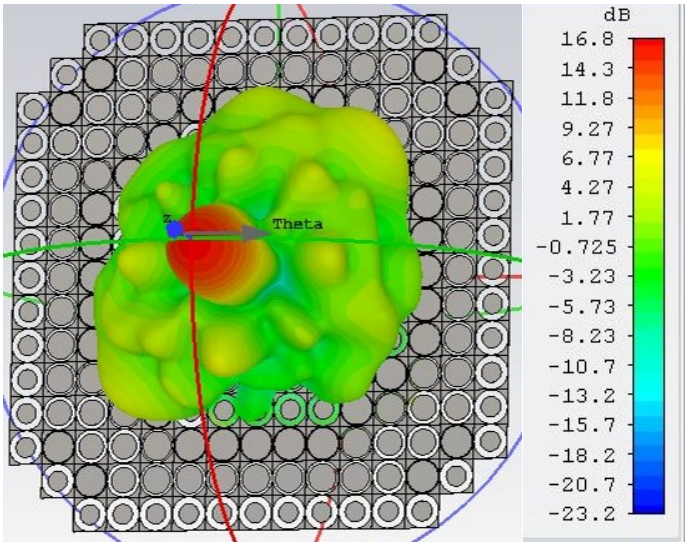

(b)

Fig. 5.9: 3D Polar plots for the proposed PGMS-FL PCA at (a) 11.2 GHz and (b) 12 GHz.

As mentioned earlier, the proposed CSCRR UC would be beneficial for the CP waves. The Fig. 5.7 (c) shows the substantial gain enhancement. The radiation patterns at 11 GHz, 11.5 GHz and 12 GHz in xz-plane and yz-plane are shown in Fig. 5.8 (a) to (c) & (d) to (f), respectively. These figures show that narrow and directive beams are obtained when PGMS-FL is utilised. The HPBW at 11 GHz, 11.5 GHz and 12 GHz are 16.5º, 15.7º and 13.2º & 15.7º, 16.4º and 13.5º, in the xz-plane & yz-plane, respectively. The 3D polar plots at 11.2 GHz and 12 GHz are presented in Fig. 5.9, which shows directive beams and low side lobes levels due to the small size of the PGMS UC. Fig. 5.10 (a) to (c) have power flow plots in the xy-plane, which demonstrate that focused and narrow beams are attained at the centre of the PGMS-FL at 11 GHz, 11.5 GHz and 12 GHz. It is empirical from Fig. 5.7 to Fig. 5.10 that the proposed PGMS-FL is indeed a focusing lens generating directive beams.

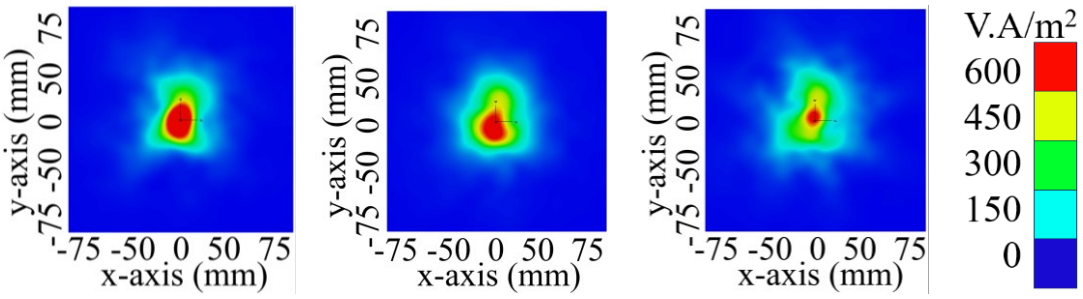

Fig. 5.10: Power flow in xy-plane displaying focused beams on the proposed PGMS-FL at (a) 11 GHz, (b) 11.5 GHz and (c) 12 GHz.

The AR plot of the proposed PGMS-FL CPA is shown in Fig. 5.11 (a). A wide ARBW of 1.19 GHz is obtained from 10.51 GHz to 11.7 GHz. The ARBW is increased from 770 MHz to 1.19 GHz, CSCRR PGMS UCs have improved the ARBW. This also proves the importance of the symmetrical designs for CP waves, and it is insensitive to the polarisation. The 3 dB axial beamwidth is shown in Fig. 5.11 (b) at 11 GHz between $\pm$13.7º, which is almost equal to the HPBWs (16.5º and 13.2º) at 11 GHz. This is crucial for the CP antenna with directive beams to have matching axial beamwidth and HPBW, which reduces the polarisation mismatch losses at 50% of power. Ideally, CP has electric field vector components E_θ and E_φ of equal magnitude and phase difference between them is 90º as shown in Eqn. 7. To solidify the proposed PGMS-FL CPA CP results, as per Eqn. 7, the magnitude ($|E_\theta||E_\varphi|$) and phase difference $(\angle E_\theta - \angle E_\varphi)$ for the obtained ARBW is approximately 1 and + 90º, respectively as shown in Fig. 5.11 (c). The positive phase difference of (+ 90º) means that the proposed PCA is an RHCP antenna.

$$|E_\theta| = |E_\varphi| \text{ and } \angle E_\theta - \angle E_\varphi = \pm 90^\circ \quad (5.7)$$

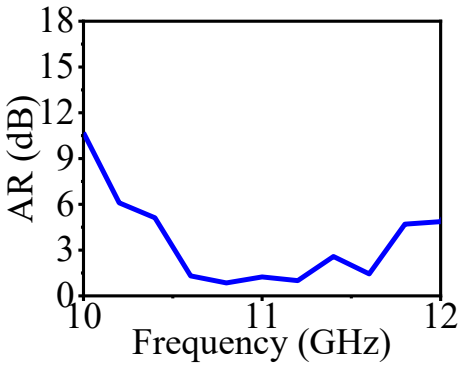

(a)

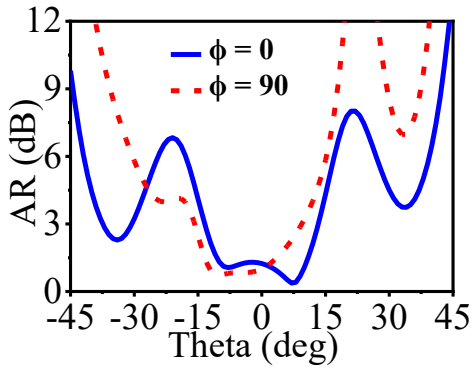

(b)

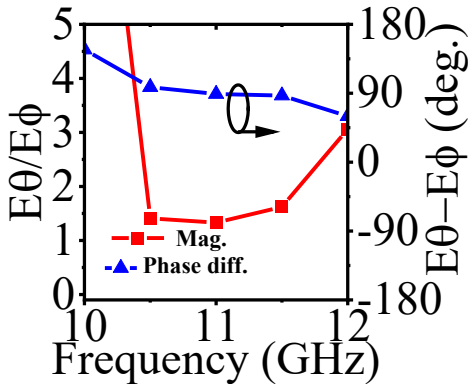

(c)

Fig. 5.11: (a) AR plot, (b) Theta vs. AR at 11 GHz, and (c) E-field component Magnitude ratio and Phase difference plot.

To analyse the performance of PGMS-FL side lobes suppression for the proposed gain enhanced antenna, the effective angular range (EAR) is studied [225]. The proposed antenna assembly in the xz-plane is shown in Fig. 5.7. The effective EAR for the proposed PGMS-FL [± θ] is calculated using Eqn. 5.8, where θ is the angle between the normal and the emitted ray from the focal point of the source antenna to the edge of the PGMS-FL and f = 30 mm and D = 150 mm.

$$\theta = arctan\,(D/2f) \tag{5.8}$$

The EAR for the proposed FL is found to be ± 68.2º; when the emitted rays from the source antenna placed at the focal point exceed ± 68.2º, the emitted rays shall not pass through the PGMS-FL, as shown in Fig. 5.12. This effectively suppresses the magnitudes of side lobes; the side lobes levels are ~ -15 dB in the xz and yz planes, as shown in Fig. 5.8.

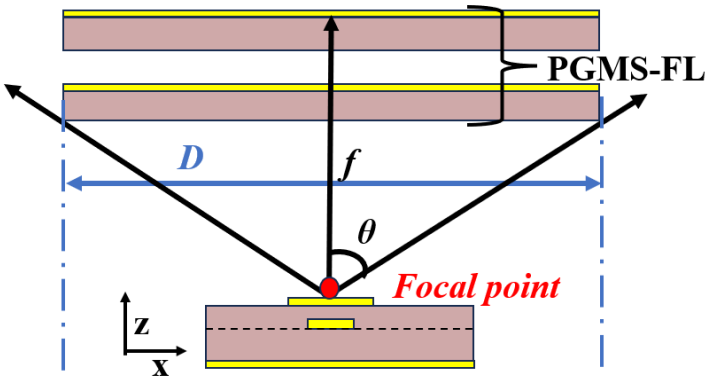

Fig. 5.12: The effective angular range (EAR) for the proposed PGMS-FL PCA.

5.4 Measured Results for PGMS-FL PCA

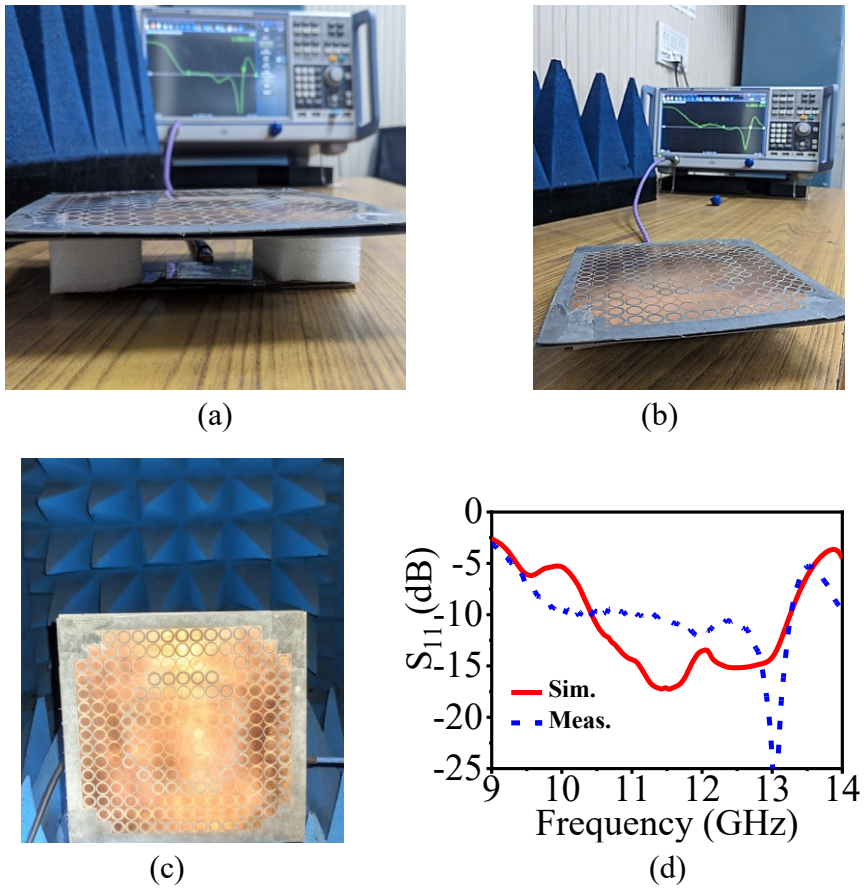

Fig. 5.13: (a) Fabricated prototype assembly, (b) S_{11} measurement set-up, (c) Pattern measurement set-up, (d) Comparison of simulated and measured S_{11}.

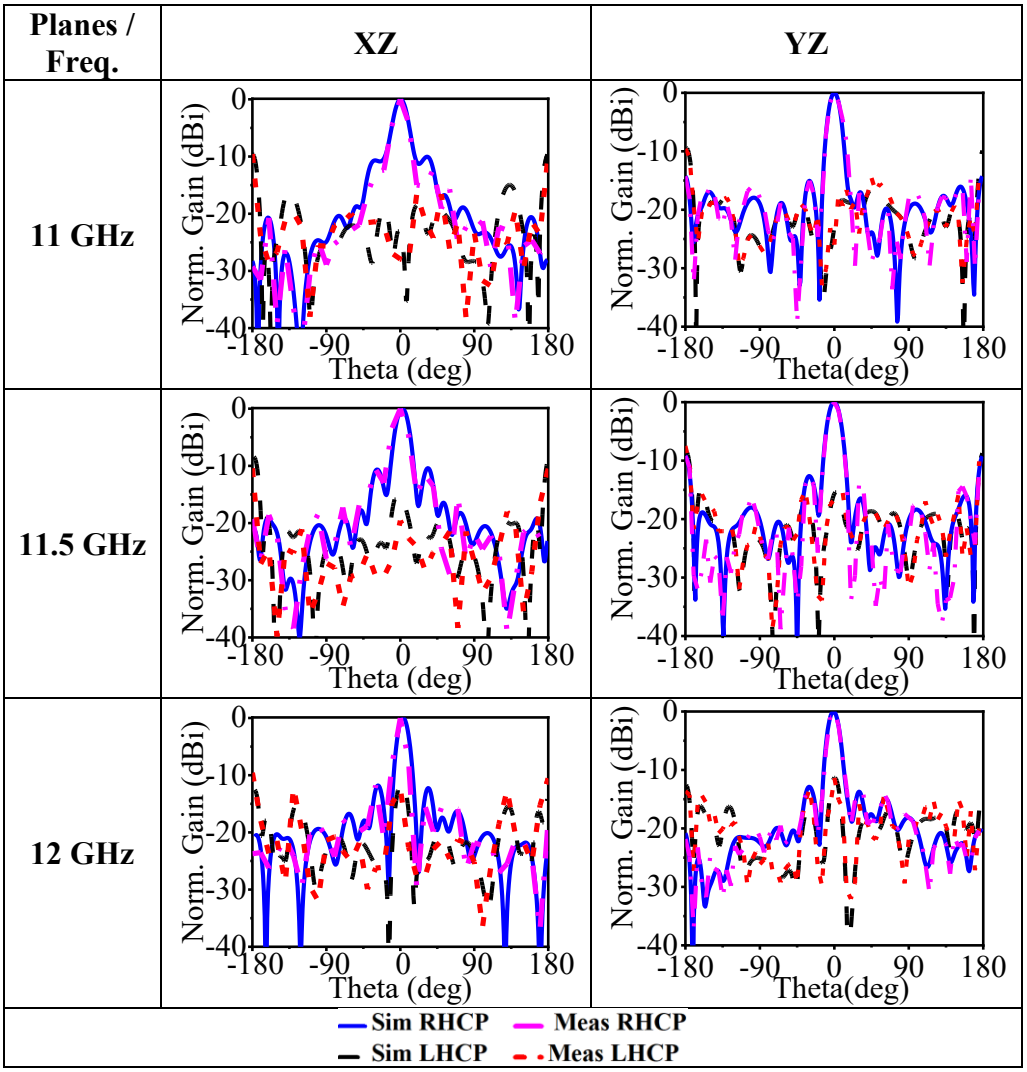

Fig. 5.14: Measured radiation patterns of the proposed antenna at 11 GHz, 11.5 GHz, and 12 GHz in the XZ-plane & YZ-plane.

A prototype was fabricated of the simulated proposed PGMS-FL PCA using RT Rogers 5880 substrate with the mentioned heights and dimensions in *Section 5.2*. To maintain the height between the source PCA and PGMS-FL, two Rohacell foam spacers are used. Similarly, to maintain a 2 mm air gap between PGMS-FL, Rohacell foam was used, as shown in Fig.5.13 (a). The aperture of PGMS-FL is 150 × 150 mm², and the thickness of the lens is 3.58 mm. The prototype is measured on the VNA and anechoic chamber as shown in Fig. 5.13 (b) & (c), respectively. The S_{11} plot in Fig. 5.13 (d) depicts resonance from 10.24 GHz to 13.27 GHz, and it almost matches with the simulated S_{11} from 10.42 GHz to 13.26 GHz. This also shows that the prototype is fabricated and well assembled.

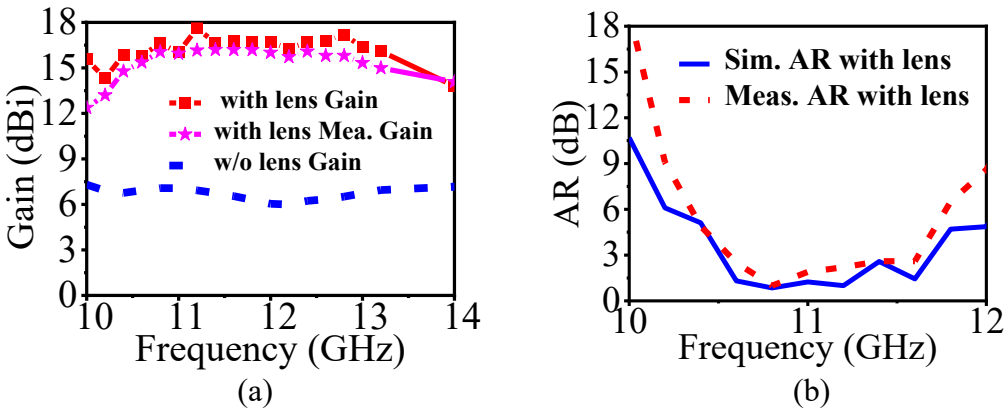

Fig. 5.15: Measured Vs. Simulated (a) Gain plot and (b) AR plot.

Table 5.3: Comparison of the proposed PGMS-FL PCA with reported PGMS antenna.

Ref.	Freq. (GHz)	Ant. Size (λ_0^3)	f (λ_0)	f/d	Gain (dBi)	ARBW (GHz)	AR Freq. (GHz)	Ant. type
[217]	9.9-10.2	3.43 × 3.43 × 1.14	0.99	0.29	1.67	No	No	Single patch
[218]	9.4-10.6	4.07 × 4.07 × 1.38	1.06	0.26	19	No	No	Dual layer
[219]	5-6.3	-	-	-	13.4	0.789	4.9-5.6	3×1 patch array
[220]	4.95-5.06, 10.68-11.3	4.52 × 4.52 × 1.61	1.4	0.3	17.9	0.62	10.68-11.3	Single patch
[221]	14.09-14.84, 22.27-23.11	7.51 × 7.51 × 2.04	1.87	2.5	12.01, 14.7	No	No	Dual layer patch
[222]	9.31-10.16	4.03 × 4.03 × 1.1	0.95	0.23	19	No	No	Single patch
This work	**10.42-13.26**	**5.21 × 5.21 × 1.12**	**1.04**	**0.2**	**17.7**	**1.19**	**10.51-11.7**	**Single patch**

The radiation patterns are measured in the xz plane and yz plane at 11 GHz, 11.5 GHz and 12 GHz as shown in Fig. 5.14. It depicts that the measured and simulated normalised radiation patterns are almost identical. However, some mismatches in the results are due to the misalignment of the focal point between FL and PCA. It also proves the established theory about polarisation-insensitivity for the proposed lens; otherwise, gain enhancement would not have been achieved. The measured and simulated gain and AR are plotted in Fig. 5.15 (a) and (b), respectively. The simulated gain is found between 15.63 dBi and 17.6 dBi, and the measured gain varies between 14.58 dBi and 16.6 dBi, as shown in Fig. 5.15 (a). The measured 3dB AR is from 10.58 GHz to 11.66 GHz, which is also almost identical to the simulated ARBW from 10.51 GHz to 11.7 GHz, as shown in Fig. 5.15 (b). The mismatch in the measured gain and ARBW are due to the fabrication tolerance and alignment error while carrying out the measurements.

Table 5.3 presents a comparative study between the proposed gain enhanced antenna with PGMS-FL and the reported PGMS-FL antenna. The table compares resonant frequencies, antenna profile, maximum gain, 3 dB ARBW and the type of source used as a feed. Table 5.3 distinguishes proposed antenna is better performing with low profile, high gain, wide ARBW than the reported antennas embedded with PGMS-FL. Furthermore, the proposed antenna provides a high gain, which appears almost flat. These aspects make the proposed CP PGMS-FL PCA suitable for 12 GHz 5G terrestrial communication.

5.5 Summary

In this chapter, an antenna is developed for the terrestrial 5G communication at 12 GHz since it has long distance propagation, and 700 MHz BW from 12.2 GHz to 12.7 GHz is sufficient for 5G communication compared to its counterparts, Sub-6 GHz frequencies. A high gain enhancement is achieved through a polarisation insensitive PGMS-FL with a planar array size of $5.21\lambda_o \times 5.21\lambda_o$. The antenna demonstrates around 10 dBi gain enhancement across frequencies 10.42GHz to 13.26 GHz, maintaining a nearly flat response with gain values between 15.63 and 17.7 dBi. Radiation patterns remain consistent, with beamwidths in the xz-plane of 16.5°, 15.7°, and 13.2° and in the yz-plane of 15.7°, 16.4°, and 13.5° at 11, 11.5, and 12 GHz, respectively. Due to CSCRR PGMS UC symmetric structure, the design was polarisation insensitive, supporting multi-polarisation. A CP is achieved with a 3 dB ARBW from 10.51 GHz to 11.7 GHz. The PGMS-FL have $\pm$ 68.2° EAR and side-lobe levels are suppressed by approximately 15 dB. The antenna maintains a low-profile configuration with an f/D ratio of 0.2 and overall dimensions of $5.21\lambda_o \times 5.21\lambda_o \times 1.12\lambda_o$.

Chapter 6

Gain Enhanced UWB and Wideband mm-Waves Antennas for 5G Communication

6.1 Introduction

In the previous *chapters*, 5G communication relied on the lower frequencies, such as the Sub-6 GHz, 10 GHz and 12 GHz bands. In this *chapter*, the requirements of mm-Wave antennas with unique antennas and MMT/ MS geometry are discussed thoroughly. Although lower frequencies (Sub-6 GHz and 12 GHz bands) offer long distance propagation and stability in the signal, when it is reflected off the surfaces but mm-Waves offer high spectral efficiencies through its large BW. Large BW means high data rates. The mm-Wave frequency bands at 28 GHz and 38 GHz have high potential for 5G cellular systems, because they have negligible atmospheric attenuation, i.e., 0.06 dB/km and 0.08 dB/km, respectively [231]. However, mm-Wave suffers from the path loss, human blockage loss, material penetration loss, etc.

$$C = Blog_2(1 + \frac{P}{N_0 B}) \quad (6.1)$$

The above mentioned losses can be compensated by *beamforming*. Thus, multiple antennas are key for mm-Wave communication. Since link capacity increases with directional high gain antennas. To attain multiplexing gain, multiple antennas are employed at the transmitter and receiver for parallel data stream transmission and reception, where these streams are independent. This reduces bit error rate, SNR, and co-channel interference. As per Eqn. 6.1, the channel capacity (C) is calculated, where P is the signal power, which is in real-time limited by regulation, and N_0 is the noise spectral density. If powers are regulated, then as per *Friis* transmission equation in Eqn. 6.2, where P_r is the received power, Pt is the transmit power, Gt is the transmitting antenna gain, Gr is the receiving antenna gain, and d is the distance between the two antennas; increasing the gain of the antennas is suitable for mm-Wave wireless communication. To maintain a high SNR, the transmit power needs to be increased. However, transmit power cannot exceed the set limit. Therefore, a multi-antenna arrangement system in the form of directive antennas or MIMO antennas. The MIMO/ beamforming is crucial for the mm-Wave communication. Due to the short wavelengths at mm-Waves, multiple antennas can be fit into a compact communication device.

$$P_r = P_t G_t G_r \left(\frac{\lambda}{4\pi d}\right)^2 \quad (6.2)$$

Thus, high gain MMT/MS mm-Wave antennas with MIMO configurations are being researched. To enhance the gain of the antenna, a High Refractive Index (HRI) MMT UC are employed, and a PGMS lens to deflect EM radiation. Although high gain and beam deflection are achieved, the MIMO configuration is not reported, and three layers of the PGMS lens increase the antenna profile [227]. An FSS array of size 3 × 5 is used as a reflector to deflect the beam to +23º and if FSS is rotated by 90º then beam is deflected to −29º. The gain is enhanced by a small fraction, 10 dBi to 11 dBi [232]. Five slabs of 1 × 4 HRI MMT structures are used to tilt the radiation to 35º from end-fire direction, and the gain is enhanced by 5 dBi [233]. Similarly, 4 slabs of 1 × 3 of HRI materials were utilised for beam deflection and gain enhancement [234]. The HRI material behaves as a metalens, which effectively increases the aperture size, resulting in gain enhancement. [235]. An ENG 'H' shaped MS are incorporated in the Vivaldi antenna aperture for the gain enhancement. With the large MS B, gain enhancement with less gain variation is observed for the impedance BW of 16 GHz [236]. Yet these antenna structures are deprived of the MIMO configuration. The PGMS-FL lenses are employed to enhance the gain of the three-port MIMO antennas [76], [237]. The offset ports from the centre encounter phase variation, which leads to beam tilts. To achieve beam tilts in the EM radiation, MMTs are usually modified. The purpose of the beam tilt is to maintain the link in the non-line-of-sight (NLOS) regions as well [238]. The ZIM is loaded onto the 2-port end-fire dipole MIMO antenna. The gain is enhanced by 2 dBi to 2.5 dBi for the operating BW of 3 GHz [75]. An anisotropic MS are utilised for phase correction and gain enhancement of the Vivaldi antenna; a high gain with low variation is attained, but to maintain high isolation the ground planes are kept disconnected [239].

For the broadside radiation for the mm-Wave antennas, an FSS reflector is used for the gain enhancement of the single mm-wave antenna with a BW of 4 GHz. The FSS UC have -6 dB BW, replicating the impedance BW of the antenna. At 28 GHz gain is enhanced from 5 dBi to 10.3 dBi [240]. The AMC reflector has a wide phase BW of approximately 2 GHz, measured at ±90º. The mm-Wave antenna has an impedance BW from 25.9 GHz to 35.5 GHz and enhanced gain varies between 5 dBi and 9 dBi. Also, a single antenna configuration is reported in [241]. A narrow band EBG reflector is integrated with a MIMO antenna; however, due to the narrow EBG BW, a high gain variation is observed across the operating BW and port isolation is maintained at 20 dB [133]. A 5 × 5 array of EBG structure is used as a reflector for a wearable application to reduce back radiation [242]. An AMC reflector for the gain enhancement of the MIMO antenna with a BW of 6 GHz. In this antenna, also, the grounds of all four ports are not connected [243]. A similar case of disconnected grounds, in a four port gain enhanced MIMO antenna [244]. Although gain enhancement and high isolation are achieved but disconnected grounds have reduced coupling between ports. A narrow BW MS is employed as a superstrate for the MIMO antenna, and a high gain is achieved in [31].

Achieving wide or UWB for MS is challenging, especially for the AIS [156]. However, an attempt is made to achieve a wide BW for AIS or AMC in [156], [245], [246], but a wide phase BW for AMC is achieved by maintaining an air gap between the

patch on the substrate and its ground in the UC [137]. It is observed that the MMT/MS structures mentioned above are confined to MMT/ MS BW ≤ 8 GHz. The wideband / UWB response of the MMT/ MS needs to be explored. Also, the MIMO antennas with a common ground are equally crucial for the communication system, with a common voltage reference for all the antenna elements that need to be studied. In this *chapter*, multiple MMT/MS are studied for different antenna structures to enhance the gain of the mm-Wave antennas. Therefore, 4 distinct antenna structures, of which two are MIMO antennas and two are single antennas, are studied in the upcoming sections.

6.2 UWB mm-Wave MIMO Antenna

In this section, a UWB AMC is designed and analysed to enhance the gain of the UWB mm-Wave MIMO antenna with its findings and results.

6.2.1 Design of UWB MIMO Antenna

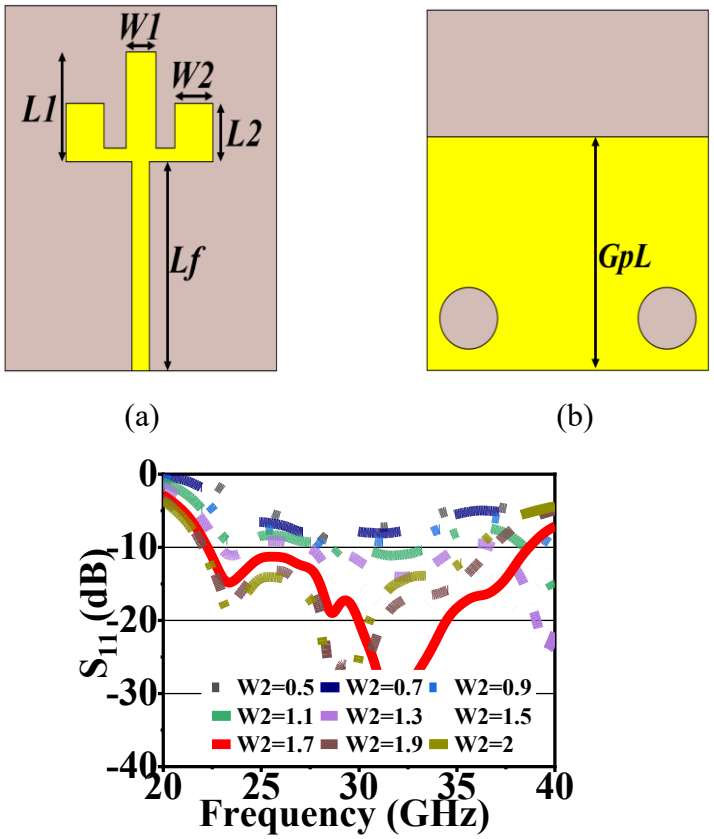

Fig. 6.1: Design of single Antenna (a) Front view, (b) Back view, (c) Parametric analysis for *W2* (*Lf* = 8.99, *L1* = 5, *L2* = 2, *W1* = 1.7, *W2* = 1.7, *GpL* = 9.65, *h1* = 0.254, ε_r = 2.2 all dimensions are in mm.).

At first, a single UWB antenna is designed with a size of 15×13 mm² on a substrate with a dielectric constant 2.2. The geometry of the single patch antenna is shown in Fig. 6.1 (a) & (b), respectively. The patch has a middle arm and two side arms. These have the width W2, which is responsible for enhancing or widening the impedance BW with a partial ground plane. The parametric analysis of width W2 is illustrated in Fig. 6.1 (c). To attain UWB impedance matching at −10 dB partial ground plane length (GpL) is chosen to be 9.65 mm. The designed single mm-Wave antenna resonated from 22.30 GHz to 38.90 GHz at W2 = 1.7 mm, as shown in Fig. 6.1 (c). The design dimensions are given below, Fig. 6.1.

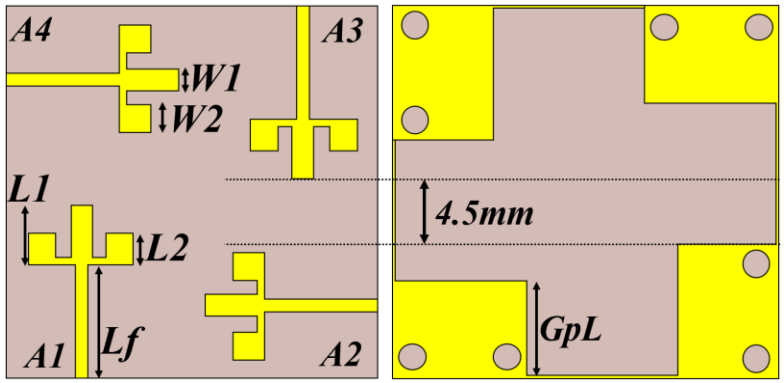

(a) (b)

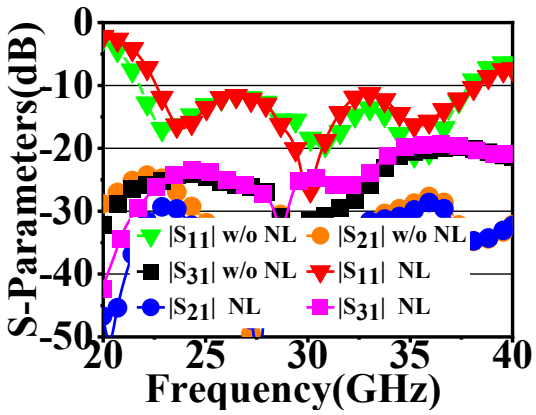

(c)

Fig. 6.2: MIMO Antenna design with NL (a) Top view, (b) Bottom view, Simulated S-Parameters without and with NL. (All dimensions of the MIMO antenna are the same as those of the single antenna.)

With the satisfactory impedance BW of the single antenna shown in Fig. 6.1, the single antenna is transfigured into a 4 × 4 MIMO antenna, as shown in Fig. 6.2 (a) & (b). The four antennas are placed orthogonally with a space of 4.5 mm between these antenna elements (A1, A2, A3 & A4). This configuration of the MIMO is chosen to achieve port

isolation of 20 dB, as the electric fields are orthogonal to each other. This makes the size of the MIMO antenna measuring 31.5×31.5 mm^2. Initially, the ground planes of all four antenna elements are disconnected to avoid direct ground current, thus improving ports isolation as suggested in [239]. For the MIMO configuration, antenna A1 has resonance from 21.78 GHz to 37.89 GHz, and antennas A1, A2 & A3 have isolation more than 20 dB, as shown in Fig. 6.2 (c). As the ground planes of the MIMO elements are disconnected, high port isolation is attained, but to maintain the same reference potential between the four ground planes, a neutralising line (NL) of width 0.2 mm is incorporated in the MIMO design. The NL runs across the perimeter of the substrate of size 31.5×31.5 mm^2. The common ground plane MIMO antenna has -10 dB impedance matching from 22.59 GHz to 38.31 GHz and high isolation of more than 20 dB, as shown in Fig. 6.2 (c).

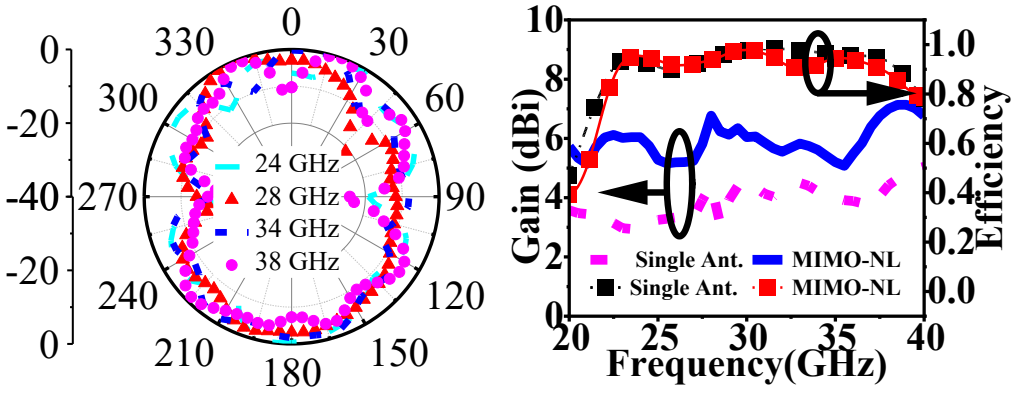

(a) (b)

Fig. 6.3: Simulated results for MIMO antenna with NL (a) Radiation patterns at 24 GHz, 28 GHz, 34 GHz, and 38 GHz, (b) Gain and Efficiency plot.

As the partial ground plane is utilised to achieve the UWB impedance BW, at the expense of back radiation with back lobes. The radiation patterns in the xz-plane are shown in Fig. 6.3 (a). The Fig. 6.3 (a) depicts that, at 24 GHz, 28 GHz, 34 GHz, and 38 GHz, back lobes are present. The Gain and Efficiency of the single antenna and the design MIMO antenna with NL are plotted in Fig. 6.3 (b). It is observed that a single antenna has a gain between 3.8 dBi and 6.6 dBi, and the efficiency lies between 77% and 91%. However, the MIMO antenna with NL has a gain between 5.08 dBi and 7.14 dBi, and efficiency lies between 86.77% and 97.92%.

6.2.2 Design of UWB AMC UC

The in-phase reflection property at ± 90º of the AMC and reflection magnitude close to 1 or 0 dB; reduces the space between the antenna and the AMC reflector to $\lambda_0/4$, which results in a reduction of antenna profile or volume. The proposed UWB AMC UC with its design dimensions is shown in Fig. 6.4 (a). In Fig. 6.4 (b), the simulation setup for the proposed AMC is shown. The AMC UC is excited in the +z-direction, replicating

back radiation from the MIMO antenna due to the partial ground plane. The boundary conditions are applied in the x-direction and y-direction as PEC and PMC, respectively.

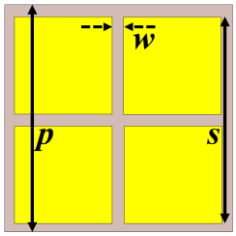

(a)

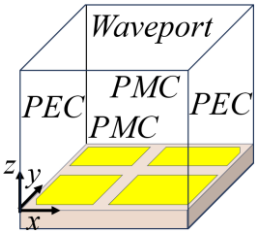

(b)

Fig. 6.4: Proposed UWB AMC UC (a) top view, (b) Simulation setup. (p = 4, s = 3.7, w = 0.35, $h2$ = 0.79, ε_r = 2.2, all dimensions are in mm.)

The proposed UWB AMC UC is embedded with a '+' shaped slot in a square patch, maintaining symmetry in the x-direction and y-direction. This exclusively excites the TM20 mode and enables the UWB phase BW for the proposed AMC. The proposed AMC has a phase BW of 14.08 GHz measured at $\pm$ 90º from 23.49 GHz to 37.57 GHz. The proposed AMC is designed in three steps, as shown in Fig. 6.5 (a) to (c). The resonant frequency (f_0) of the is calculated from Eqn. 6.3 [247],

$$f_0 = \frac{1}{2\pi\sqrt{L_T C_T}} \tag{6.3}$$

where C_T and L_T are the total capacitance and inductance of the metallic patches and substrate of the unit cell, respectively.

At the first step, AMC-I, the assembly of the AMC UC is simple; the RT Rogers 5880 substrate with a dielectric constant of 2.2 is sandwiched between a square patch and ground. When AMC-I is excited, the E-fields vary in the x-direction, resembling two half-wavelengths, but the fields are evenly distributed along the y-direction, implying TM10 mode is excited in the AMC-I, as shown in Fig. 6.5 (a). The E-fields are tightly coupled, which oscillates between adjacent AMC UC and resemble a capacitor (Ca) between two UC. The patch behaves as an inductor (L1), and the dielectric behaves as an inductor (L_d) in the Equivalent Circuit Model (ECM) [132]. The resultant phase BW +90° to -90° for the AMC-I is undesired for the frequencies from 22 GHz to 38 GHz. The Fig. 6.5 (d)

shows the phase BW for the AMC-I. The TM10 mode is responsible for the narrow phase BW. To UWB phase, BW higher mode needs to be excited, such as the TM20 mode.

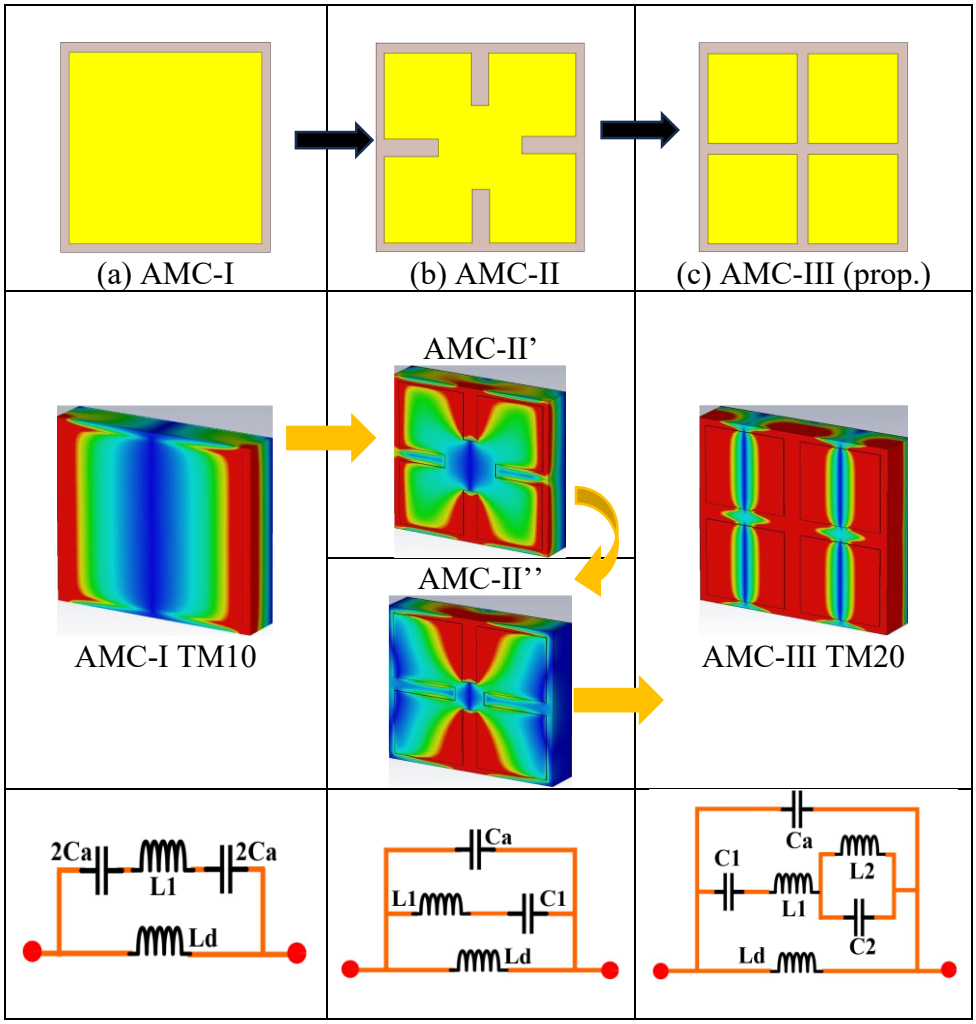

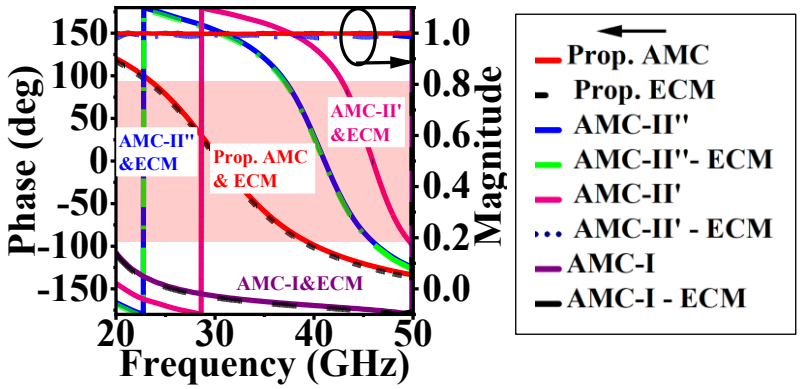

(d)

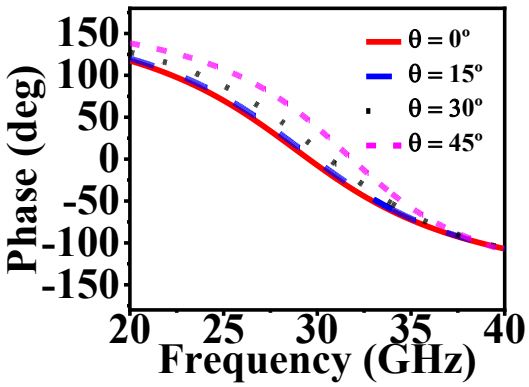

(e)

Fig. 6.5: E-fields at 30 GHz and ECM for respective AMC (a) AMC-I, (b) AMC-II, (c) AMC-III, and (d) Simulated Phase and Magnitude response for AMC-I, AMC-II, & AMC-III, & (e) Analysis of AoI for proposed AMC-III.

For the second step, AMC-II, symmetrical slots have been made in the AMC-I patch. The size of these slots is 1.2×0.35 mm^2. To analyse AMC-II, two iterations have been done AMC-II' and AMC-II''. In the first iteration of AMC-II, i.e., AMC-II's owning slot size 1.2×0.35 mm^2 generates capacitance (C1) in the ECM as shown in Fig. 6.5 (b). The capacitor (C1) is connected in series with L_1, and both of these are connected in parallel with C_a; as the inherent fringing capacitance produced by the patch is connected in parallel [247]. For the AMC-II', the E-fields can be seen between the newly added slots, as shown in Fig. 6.5 (b). As a result, the phase BW response is shifted between ±180º, and the magnitude is maintained close to +1, as shown in Fig. 6.5 (d). However, AMC-II' also does not have the desired phase BW. Therefore, the length of the added slot is increased by 1.5 mm from 1.2 mm; this iteration of AMC-II is referred to as AMC-II''. Post slot optimisation, the E-fields observed between the slots have a higher magnitude, resulting in C1 >> Ca, and the phase response is shifted in the lower spectrum as shown in Fig. 6.5 (d). However, spurious modes are obtained for both iterations of the AMC-II, and the transition between mode TM10 and TM20 is observed in Fig. 6.5 (b).

In the third step, AMC-III, to achieve the UWB phase BW response and to excite the TM20 mode, the slot length is increased to 18.5 mm from 1.5 mm (AMC-II''). Doing so, the AMC patch is divided into four adjacent patches in the AMC UC, as shown in Fig. 6.5 (c). The E-fields are shown in Fig. 6.5 (c), which depicts a large and equal magnitude of the E-fields across adjacent patches of the AMC UC and adjacent AMC UC, resulting in mode TM20. A clear transition of modes from TM10 to TM20 can be observed in Fig. 6.5 (a) to (c). In the ECM of the AMC-III, inductance (L_2) and capacitance (C_2) are introduced, which are formed by the four adjacent square patches in the AMC UC [156].

The AMC-III and its ECM resulted UWB phase response measured at ±90º. Finally, AMC-III dimensions s and w were optimised to 3.65 mm and 0.4 mm, respectively, to match the impedance BW from 22.59 GHz to 38.31 GHz of the designed

mm-Wave MIMO antenna. The proposed AMC-III phase BW is obtained from 23.49 GHz to 37.57 GHz at + 90º and - 90º, respectively, as shown in Fig. 6.5 (d).

$$CT = C1 + C2 + Ca \quad (6.4)$$

$$LP = L1 \,||\, L2 \quad (6.5)$$

$$LT = LP \,||\, Ld \quad (6.6)$$

For the ECM of the proposed AMC-III, since the E-field magnitude is equal for adjacent patches and adjacent UCs. The capacitors C_1, C_2 and C_a will have almost identical values. The EMC values for L_d, L_1, L_2, C_1, C_2 and C_a are 0.536 nH, 0.477 nH, 0.07 nH, 0.151 pF, 0.149 pF, and 0.152 pF, respectively. To study the incidence stability of the proposed AMC-III, the angle of incidence (AoI), i.e. θ, is varied from 0º to 45º, and the phase response is plotted in Fig. 6.5. (e). It shows that the AMC-III phase is affected as the incidence angle is increased to 45º. This shows the proposed AMC-III is stable for higher angles of incidence. The polarisation insensitivity of the AMC-III is verified through TE-polarised and TM-polarised waves will have identical responses.

The values for capacitors C_1, C_2 and C_a are almost similar since the E-field magnitude across adjacent small patches and unit cells is almost equal. The equivalent values for L_d, L_1, L_2, C_1, C_2 and C_a are 0.536 nH, 0.477 nH, 0.07 nH, 0.151 pF, 0.149 pF, 0.152 pF, respectively. The angle of incidence (AoI), i.e. θ, is varied to study its effect on the AMC phase, as shown in Fig. 5 (e); it shows that the AMC phase is affected after AoI is increased to 45º; due to the symmetric AMC design, TE and TM polarisation response will be identical for different AoI as shown in Fig. 6.5 (e).

6.2.3 AMC Array and MIMO Antenna Integration for Gain Enhancement

As the designed MIMO antenna exhibits low gain, which is seen in Fig. 6.4, a 10 × 10 array of proposed AMC UC is designed, which measures 50 × 50 mm^2 and is placed at a height 'ht' beneath the MIMO antenna for the gain enhancement. The geometry of the proposed gain enhanced MIMO antenna is shown in Fig. 6.6. In the AMC array, AMC UCs are 1.2 mm apart from adjacent UCs. This is done to maintain the desired impedance BW of the MIMO antenna, without changing its dimensions. The height 'ht' is chosen to be 5 mm, which is equivalent to 0.38 λ_0 (λ_0 at 23.27 GHz). The height 'ht' of 5 mm is chosen considering the design and dimensions of the connector to feed the MIMO antenna [248]. The simulated S-parameters for the proposed gain enhanced antenna are plotted in Fig. 6.7 (a). The proposed antenna resonates from 23.27 GHz to 39.3 GHz, and the ports isolation is more than 19.84 dB.

A significant gain enhancement is found for the proposed antenna; the enhanced gain is between 8.7 dBi and 12.21 dBi for the impedance BW 16.03 GHz from 23.27 GHz to 39.3 GHz. The gain is enhanced from 6.02 dBi to 8.7 dBi at 24 GHz, 6.74 dBi to 10 dBi at 28 GHz, and 6.96 dBi to 11.2 dBi at 38 GHz. Different sizes of AMC arrays are

also used as a reflector for the gain enhancement, including a PEC reflector. Different sizes, such as 6 × 6, 8 × 8, 10 × 10 (prop.) and PEC reflector placed are at a height of 0.38 λ_0 from the MIMO antenna. It was found that the proposed AMC array size of 10 × 10 UCs results in better gain, maintaining a compact size of 50 × 50 mm^2, as shown in Fig. 6.7 (b).

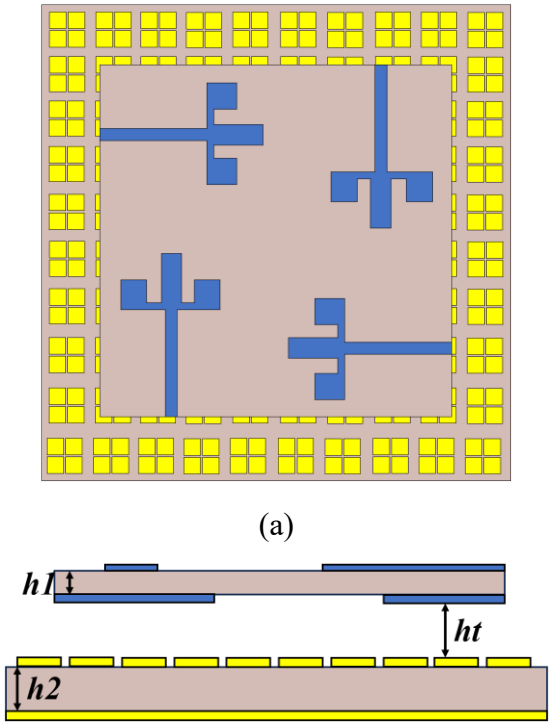

(a)

(b)

Fig. 6.6: Assembly of the proposed antenna (a) Top view, (b) Side view.

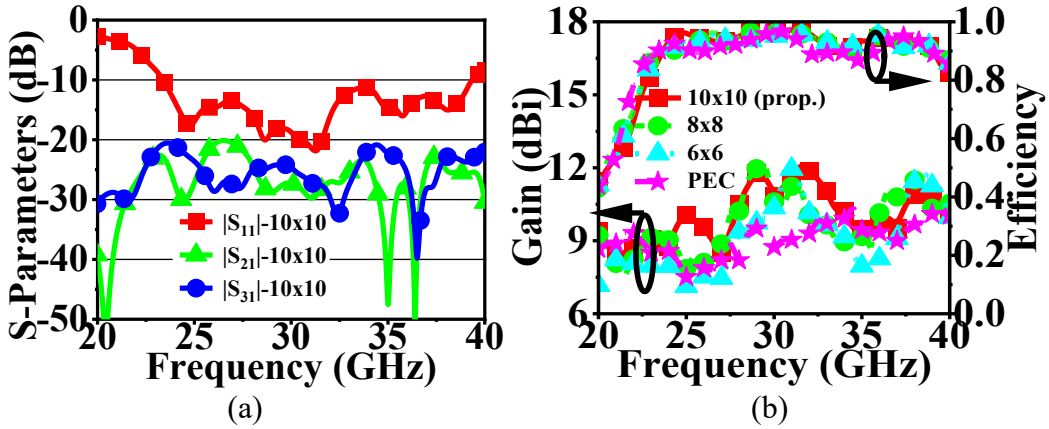

(a) (b)

Fig. 6.7: Proposed Antenna responses (a) Simulated S-parameters (b) Simulated Gain and Efficiency.

6.2.4 Measured Results of the UWB mm-Wave MIMO Antenna

The proposed mm-Wave MIMO prototype is fabricated, and S-parameter measurements were carried out on the VNA as shown in Fig. 6.8 (a) & (b). A Rohacell foam spacer is used to maintain the established height of 5 mm. The measured S-parameters are compared with simulated S-parameters in Fig. 6.8 (c). It shows a fabricated antenna resonates from 22.56 GHz to 39.14 GHz with a BW of 16.58 GHz, and the achieved isolation is more than 20.1 dB. The measured and simulated almost match each other. The measured gain is plotted with the simulated total efficiency in Fig. 6.8 (d). The maximum gain has enhanced from 5.66 dBi to 12.21 dBi at 31.5 GHz, and total efficiency is found between 89.14% and 96.13%.

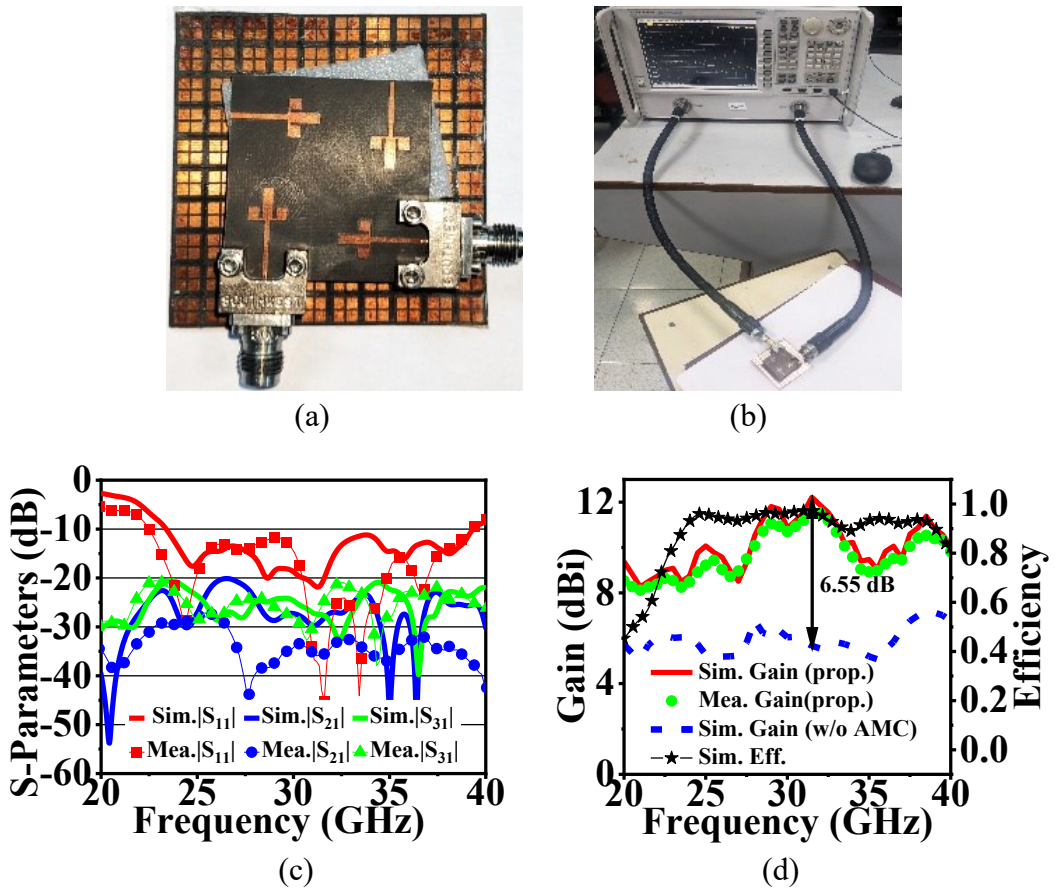

Fig. 6.8: Proposed gain enhanced MIMO antenna (a) Fabricated prototype, (b) VNA measurements, (c) S-Parameters, (d) Gain and Efficiency plot.

Fig. 6.9 shows the radiation patterns measured in the XZ-plane and YZ-plane at 24 GHz, 28 GHz, and 38 GHz. In Table 6.1, the proposed antenna is compared with the reported antenna in the literature. It shows the proposed antenna has UWB impedance, BW and UWB phase BW for the proposed AMC, which is an MS. The proposed antenna

measures 3.8 λ_0 × 3.8 λ_0, which is the length × width of the proposed AMC array, and the side profile stands at 0.38 λ_0. The fractional impedance BW is 49.52% (16.03 GHz), and the AMC UC phase BW is 46.11% (14.08 GHz).

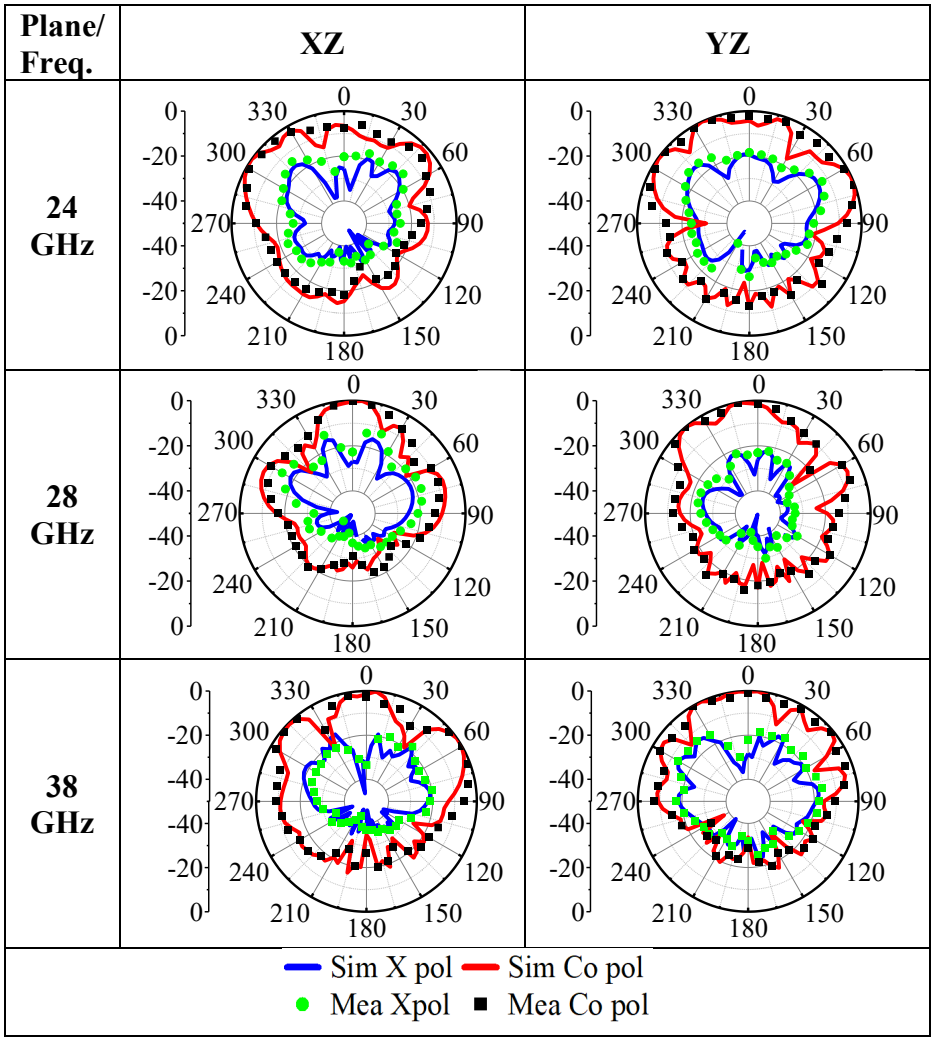

Fig. 6.9: Comparison of measured and simulated radiation patterns.

The diversity performance analysis of the proposed MIMO antenna is conducted by referring [150], [249]. The Envelope Correlation Coefficient (ECC) and Diversity gain (DG) are plotted in Fig. 6.10 (a). It is found that ECC < 0.005 and DG > 9.9 dB. The Channel Capacity Loss (CCL) and Total active reflection coefficient (TARC) are plotted in Fig. 6.10 (b). The CCL < 0.26 b/s/Hz and TARC < -10 dB. These parameters ensure that the proposed antenna can work efficiently as a 5G mm-Wave MIMO antenna.

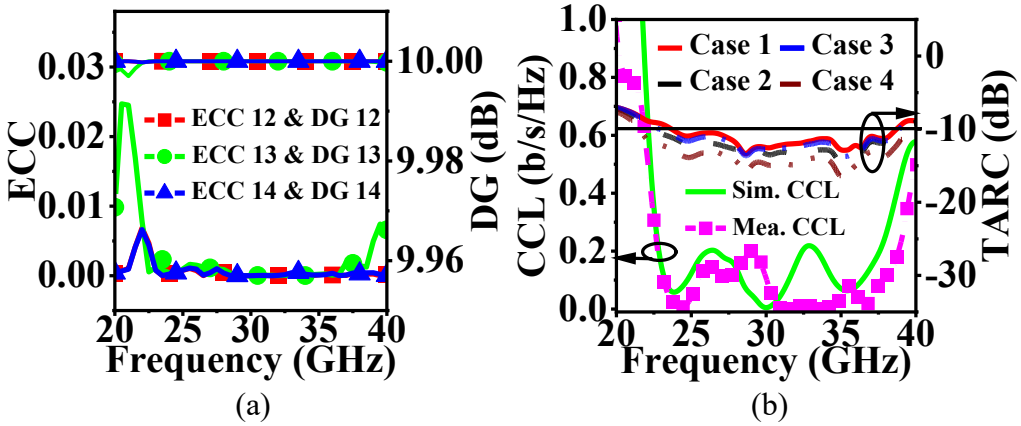

Fig. 6.10: MIMO Diversity Parameters (a) ECC & DG, (b) CCL & TARC. Cases are (Case 1: θ_0=0º, θ_1=30º, θ_2=60º, θ_3=90º, Case 2: θ_0=0º, θ_1=30º, θ_2=60º, θ_3=180º, Case 3: θ_0=0º, θ_1=30º, θ_2=60º, θ_3=270º, Case 4: θ_0=0º, θ_1=60º, θ_2=120º, θ_3=180º, where θ_i is the phase of the incoming signal at (i+i) th antenna).

Table 6.1: Comparison of the proposed UWB mm-Wave antenna with the antennas in the literature.

Ref.	Freq (GHz)	% BW Ant.	Isolat. (dB)	Peak Gain (dBi)	UC-BW (GHz)	Ant. ht. (λ_0)	Ant. Size (λ_0^2)
[240]	25.5-30.8	18.82	NA	11	5	0.42	4.45
[250]	24-28	15.38	NA	9.8	10	0.06	2.43
[239]	24-32	28.57	>15	10.2	8	0.04	8.3
[75]	27-30	10.52	>22.25	9.6	6	0.04	7.78
[243]	26-31.5	19.13	> 21	10.1	< 0.5	0.42	16.56
[244]	23.41-28.91	21.02	>22.25	10.42	9.5	0.33	2.92
[31]	24.55-26.5	7.63	>30	10.27	< 0.8	0.48	8.57
Pro. ant.	**23.27-39.3**	**49.52**	**>19.84**	**12.21**	**14.08**	**0.38**	**14.44**

6.3 Beam tilting MIMO Antenna using PGMS lens

A mm-Wave MIMO antenna is designed to resonate at 28 GHz, and a PGMS lens is utilised to deflect the radiation of the antenna elements and to enhance the its gain.

6.3.1 Design of MIMO Antenna

A Quarter Wave Transformer (QWT) Antenna is designed to resonate at 28 GHz. The feed is matched to 50 ohms, and substrate RT Rogers duroid 5880, which has a dielectric constant of 2.2 and a thickness of 0.254 mm, is used. The design of the MIMO antenna is shown in Fig. 6.11. The design dimensions are as follows, Ls = 15.5 mm, |Ws = 21.25 mm, Lp = 3.25 mm, Wp = 5.5 mm, Lqwt = 2mm, Fl = 6 mm.

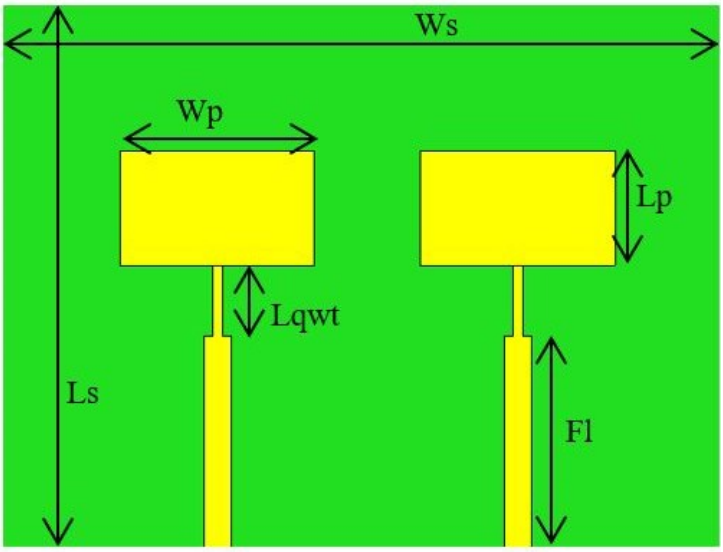

Fig. 6.11: Design of QWT MIMO Antenna.

6.3.2 Design of Beam Tilting PGMS Lens

The Beam Tilting PGMS UC comprises three layers of identical design etched on the top of the substrates. The design has 'T' shaped arms whose length is responsible for the phase variation. The PGMS UC is designed on the RT Rogers 5880 with a thickness of 0.254 mm, as shown in Fig. 6.12. Three layers of substrate were chosen to maintain high transmission magnitude (> 0.5), as shown in Fig. 6.13. The wide transmission BW is obtained because of the air gap of 0.8 mm between the substrate layer [76]. The dimensions of the PGMS UC are L = 1 mm, L_1 = 1.7 mm, t_1 = 0.1 mm, t_2 = 0.15 mm, d = 4 mm. The total UC profile is the tri-layered lens profile, which is 0.29 λ_0 (λ_0 at 28 GHz).

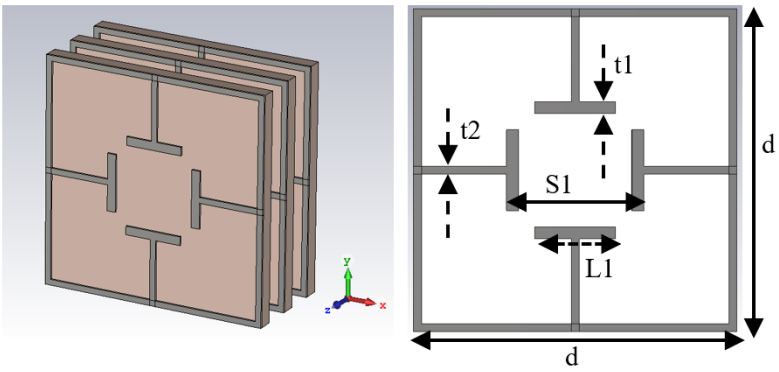

(a) (b)

Fig. 6.12: Tri-layer PGMS UC, (a) Isometric for simulation view, (b) Top view.

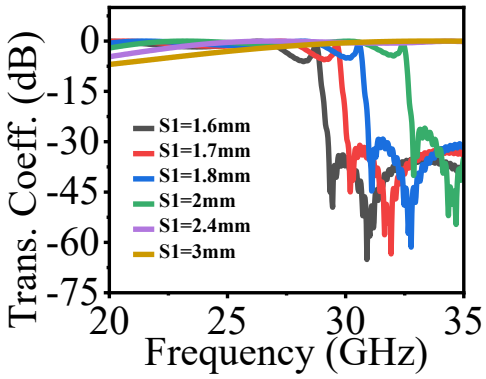

Fig. 6.13: Simulated Transmission magnitude for the designed PGMS UC at different values of 'S1'.

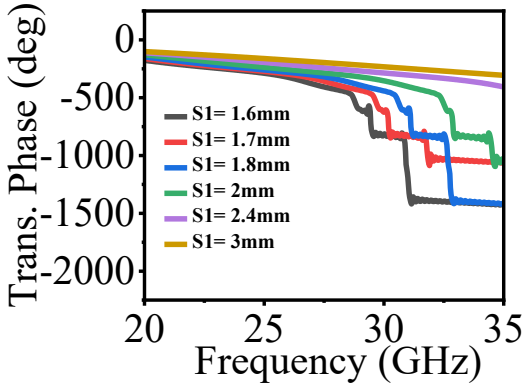

Fig. 6.14: Simulated Transmission phase for the designed PGMS UC at different values of 'S1'.

The magnitude and phase of the designed PGMS UC vary with the change in the Space S1 between the 'T' shaped arms, as shown in Fig. 6.13 & Fig. 6.14. Post analysis

of the designed PGMS UC, six UC were chosen with transmission magnitude > 0.7 to cover the phase from 0º to 226.25º. High transmission will result in better radiation characteristics.

The phase difference (Δφ) of 45º is kept between these six PGMS UC. Each of these UC introduces a controlled phase delay, and the antenna beam is deflected to an angle 'θs' with respect to broadside radiation, which is calculated from Eqn. 6.7 [238],

$$Sin(\theta s) = \frac{\lambda}{2\pi d}\Delta\varphi \tag{6.7}$$

6.3.3 Results of the Proposed Beam Tilting MIMO Antenna

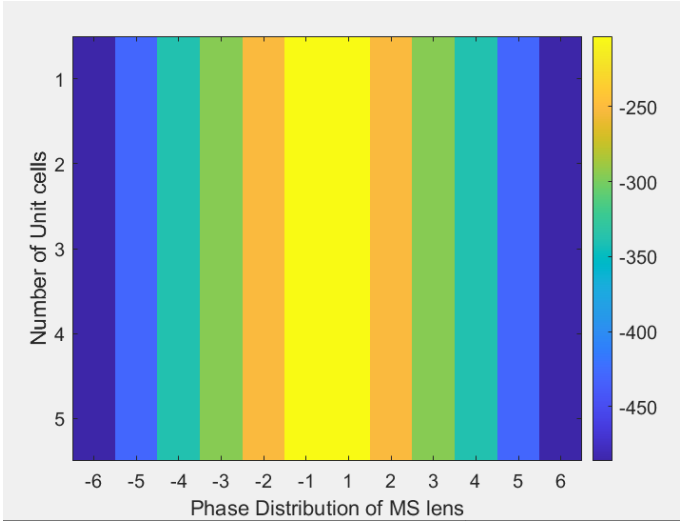

Fig. 6.15: Phase distribution on the 5 × 12 array.

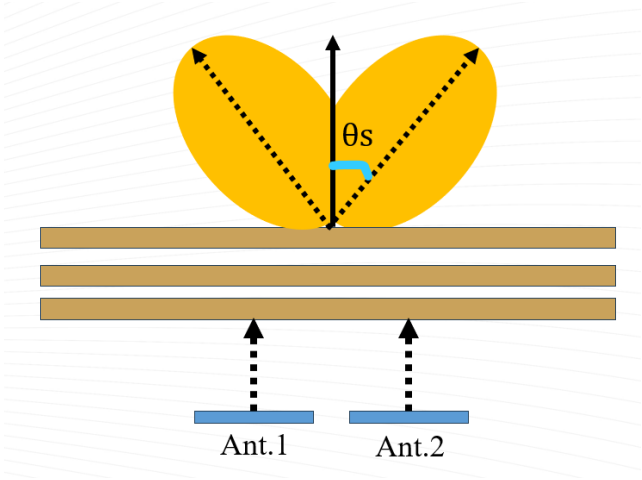

Fig. 6.16: Schematic of the proposed beam tilting MIMO antenna.

The angle at which the beam tilt will be observed is 20º for the phase difference (Δφ) of 45º between two successive PGMS UC. This means the broadside radiation of the MIMO antenna can be deflected to 20º, if PGMS UC are placed in phase progression on the array. Therefore, an array of size 5 × 12 PGMS UC is built, in which UCs are placed in the progressive phase from the centre to both edges of the array, as shown in Fig. 6.15. The designed tri-layered PGMS array is placed on the designed QWT MIMO antenna as a lens to deflect the radiation and tilt the beams. The Separation between the Beam tilting lens and the MIMO antenna is 5 mm, and the schematic of the proposed beam tilting antenna is depicted in Fig. 6.16.

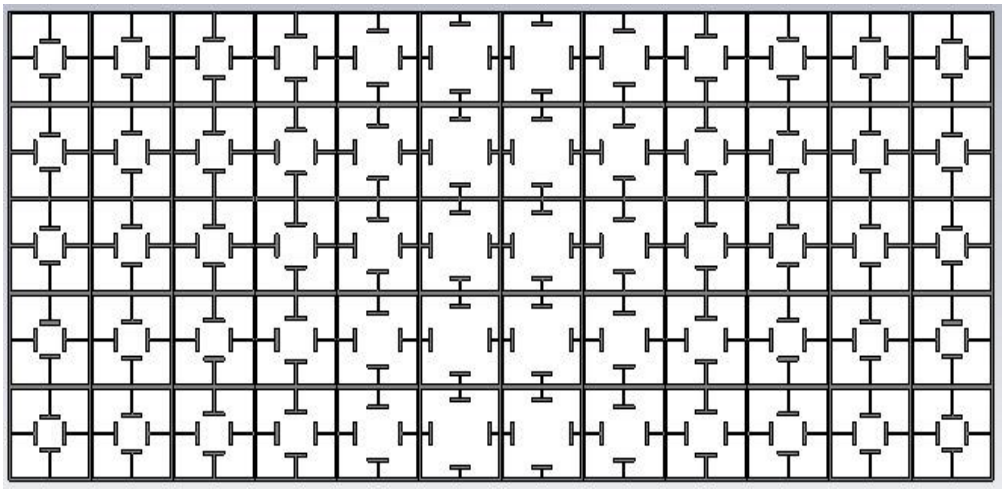

Fig. 6.17: Beam tilting PGMS UC distribution on 5 × 12 array.

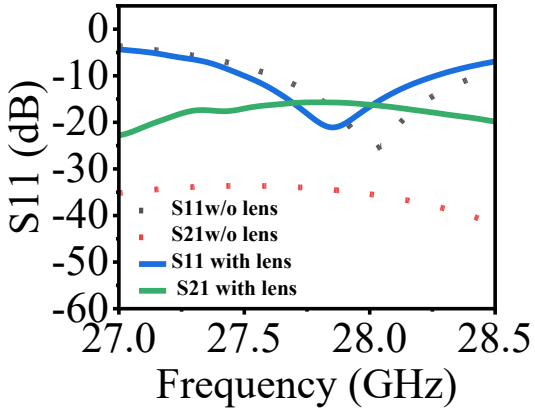

Fig. 6.18: Simulated S-parameters of the proposed MIMO Antenna.

The S-parameters of the proposed MIMO antenna with and without the beam tilting PGMS lens are shown in Fig. 6.18. A slight shift in the resonance and a reduction in isolation are caused by the coupling between the antenna and the lens. The proposed

antenna resonates from 27.4 GHz to 28.26 GHz, and the minimum isolation stands at 15.71 dB. With the introduction of the PGMS lens to the antenna, a controlled time delay or phase has pointed the beam radiation in the xz-plane to −24º and +24º for antenna 1 and antenna 2, respectively.

To avoid rigorous EM-simulations, the values for the 'S1' were chosen to result in the phase difference (Δφ) between two successive unit cells is close to 45º. Therefore, a difference of 4º is obtained between the calculated and simulated beam tilt. The beam tilts are shown in Fig. 6.19 for antenna 1 and antenna 2 in the xz-plane. In Fig. 6.20, the beam tilts of both antennas are compared, showing the directive patterns at ±24º. Since the QWT antennas are identical and the phase distribution on the lens is symmetric, identical radiation patterns are attained in the opposite direction.

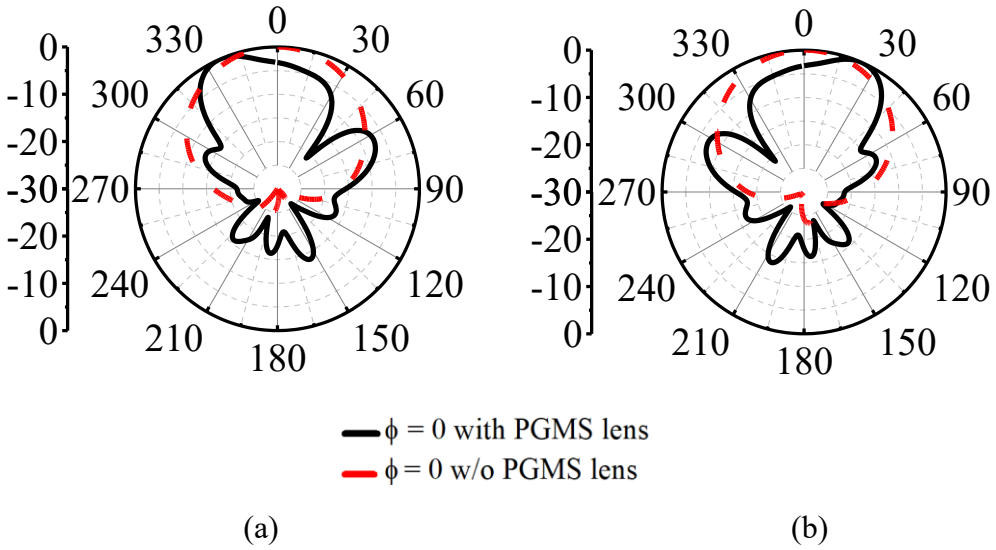

Fig. 6.19: Radiation patterns in xz-plane at 28 GHz (a) Antenna 1 & (b) Antenna 2.

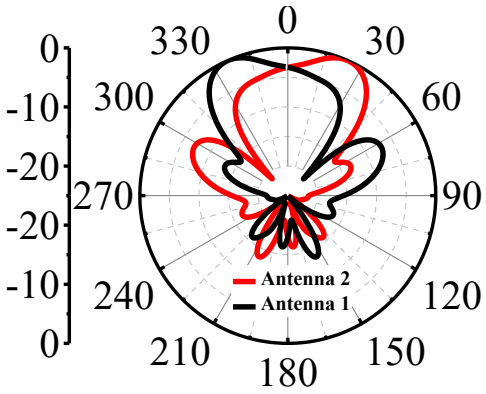

Fig. 6.20: Comparison of the beam tilts for Antenna 1 and Antenna 2.

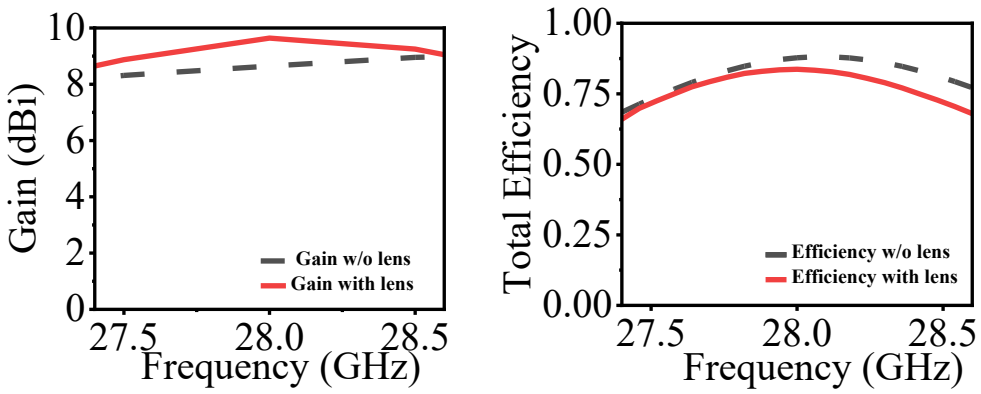

(a) (b)

Fig. 6.21: Proposed Antenna Response (a) Gain & (b) Total Efficiency.

6.4 DNG loaded mm-Wave Antenna

A DNG MS is designed to enhance the gain of the mm-Wave Dipole Antenna and to attain high FTBR. In the following subsections, the design of DNG MS and the dipole antenna are presented with results.

6.4.1 Design of DNG MS

A square SRR UC is designed with offset splits on each arm resonating at 26 GHz, as shown in Fig. 6.22. To achieve the desired DNG properties, i.e. offset splits are modified to maintain negative permittivity and negative permeability. The width of the offset split is 0.2 mm, and Rogers RT duroid 5880, which has a dielectric constant of 2.2, is used as a substrate. The thickness of the substrate is chosen to be 0.79 mm to avoid the fragility of the antenna. The size of the UC is 4 × 4 and Ux = Uy = 3 mm. The PEC and PMC are the boundary conditions applied in the x-direction and z-direction, respectively, and UC is excited in the y-direction, replicating EM incidence from the dipole antenna whose E-fields are in the x-direction. The reflection and transmission coefficient of the DNG UC are shown in Fig. 6.23, which shows that DNG UC has an operating bandwidth from 22 GHz to 30 GHz. MS to work as a transmitive MS, the transmission coefficient should be close to 0 dB for the required operating frequencies. In Fig. 6.24, negative permittivity and negative permeability, and NRI refractive index for the frequencies from 22 GHz to 26.5 GHz and RI is zero for the frequencies 26.5 GHz to 28 GHz. Therefore, the designed UC is referred to as DNG UC. To extract the MMT properties, i.e. DNG properties, are extracted referring [251].

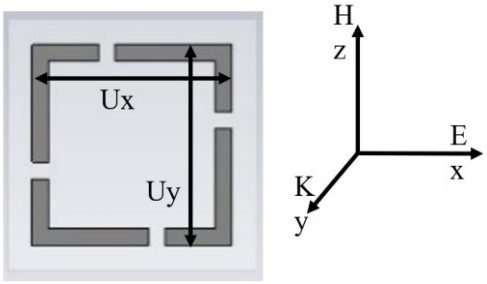

Fig. 6.22: Designed Square SRR DNG UC.

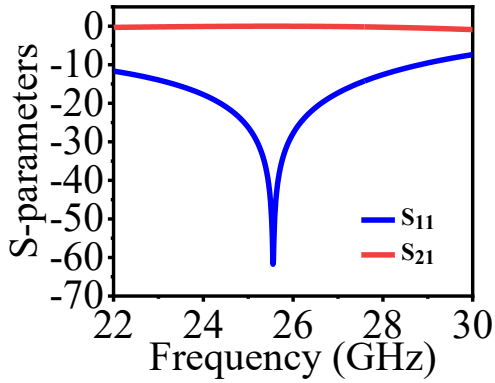

Fig. 6.23: Reflection and Transmission Coefficient for Square SRR DNG UC.

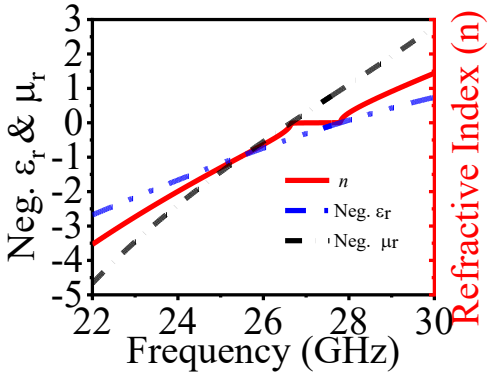

Fig. 6.24: Extracted parameters of the designed square SRR DNG UC.

6.4.2 Design of the Dipole Antenna and DNG Loading

A dipole patch antenna is designed to resonate at 26 GHz using Rogers RT duroid 5880 substrate with a thickness of 0.79 mm. The dipole arms are matched to 50 ohms for maximum power transfer. The designed DNG UCs are placed in the aperture of the dipole arm, forming an array size of 4 × 5 UCs. The DNG UCs are loaded on the dipole antenna in two stages. First, UCs are placed in the same plane as the dipole patch, i.e. top side. In

the second stage, another array of the same size is placed in the same plane as the ground plane of the dipole antenna, i.e. bottom side. The proposed dipole antenna with DNG loading is shown in Fig. 6.25. The size of the proposed antenna is 20 × 19 mm^2. The dimensions of the dipole antenna are Dw = 3.25 mm, GpL = 13 mm, GpW = 6 mm.

The proposed dipole antenna design produces maximum radiation along the y-direction by narrowing the radiation beam, while minimising the back lobe. Therefore, to enhance the gain, DNG cells are placed in front of the dipole antenna.

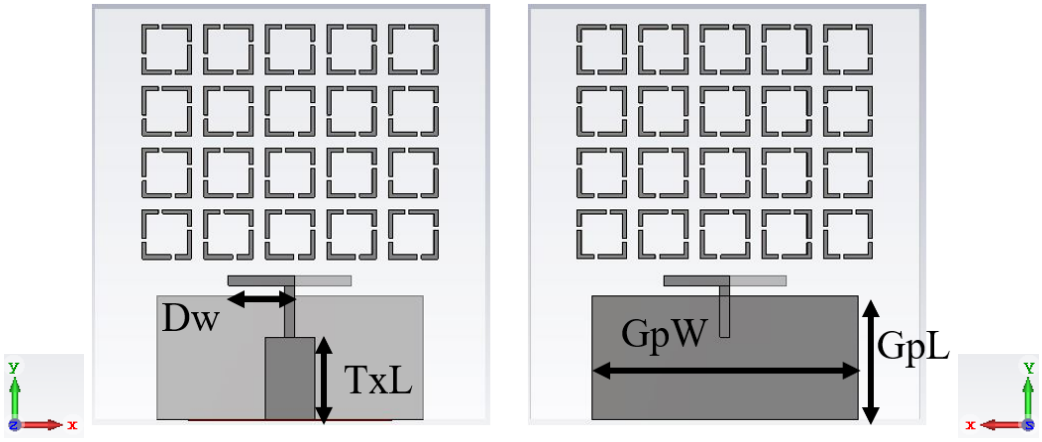

Fig. 6.25: Design of the proposed gain enhanced dipole antenna.

6.4.3 Results of the DNG Loaded Dipole Antenna

The Simulated S_{11} of the proposed DNG loaded Dipole Antenna is shown in Fig. 6.26. Fig. 6.26 also compares the S_{11} of the first stage, i.e. single DNG loaded and without any DNG loaded dipole antenna. Since the DNG UC has 0 dB transmission magnitude over the operating BW, the resonance of the dipole antenna is almost unaffected. The proposed DNG loaded dipole antenna resonates from 24 GHz to 28 GHz.

To enhance the gain of the dipole antenna, DNG arrays are loaded on the top and bottom sides of the substrate. These DNG UCs are excited by the E-fields and H-fields of the dipole antenna. Each segment of these arrays is responsible for concentrating the radiation in a single direction. At first, the dipole antenna was loaded with 4 × 5 DNG UCs on the top side, which enhanced the gain of the antenna by 3 dB for the operating BW from 24 GHz to 28 GHz, as shown in Fig. 6.27. A significant gain enhancement is achieved with just a single DNG loading. Therefore, another 4 × 5 DNG UCs are loaded on the bottom side of the antenna, as illustrated in Fig. 6.27. The gain of the dipole antenna is enhanced by 1.2 dB to 1.5 dB. At 24.4 GHz, the gain is enhanced from 5.01 dBi to 8.99 dBi, and at 27.8 GHz, the gain is enhanced from 5.6 dBi to 9.8 dBi, as shown in Fig. 6.27. The gain has been significantly enhanced by at least 4 dB, and the enhanced gain is stable and flat for the operating BW of 4 GHz.

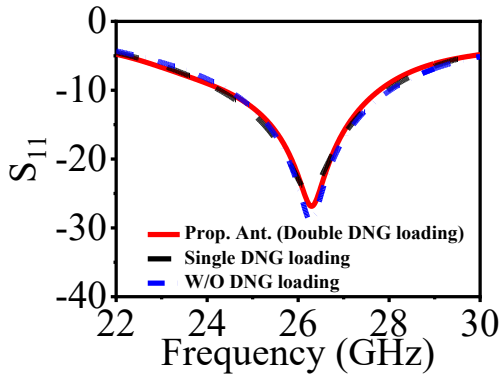

Fig. 6.26: Simulated S_{11} at all three stages of DNG loading onto dipole antenna.

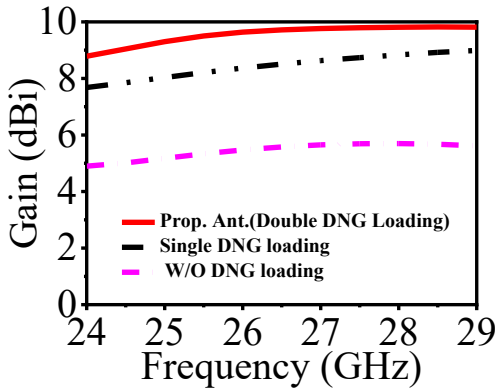

Fig. 6.27: Simulated Gains at three stages of DNG loading onto dipole antenna.

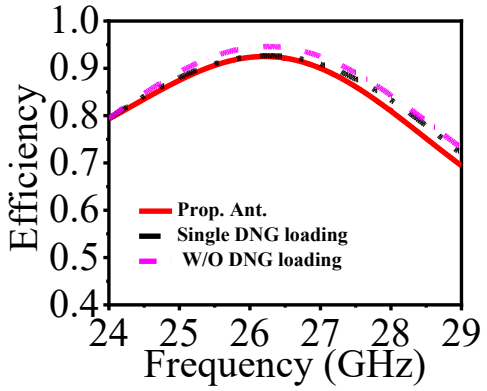

Fig. 6.28: Simulated Efficiencies at three stages of DNG loading onto dipole antenna.

The total simulated efficiency for all three stages is plotted in Fig. 6.28, which depicts that the proposed double DNG loaded dipole antenna has efficiency between 85 % and 92 %. While the first and second stages also have almost similar efficiencies. This means the efficiency of the dipole antenna is unaffected, just as resonance minor

variance is observed, which is in an acceptable range. The radiation patterns at 26 GHz are plotted in Fig. 6.29. In Table 6.2, the FTBR for three stages of DNG loading are compared at 26 GHz. A high FTBR of 20.59 dB, i.e., ~ 20.6 dB, is achieved using double layer DNG loading.

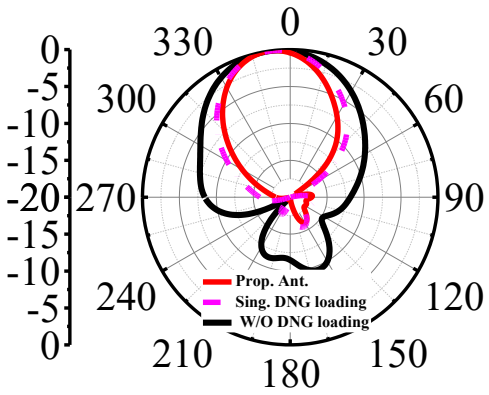

Fig. 6.29: Simulated radiation patterns in xy-plane at three stages of DNG loading onto dipole antenna.

Table 6.2: Comparison of FTBR at three stages.

Stages of DNG loadings	**FTBR (dB)**
Without DNG loading (simple dipole antenna).	10.81
Single layer DNG loading (top side loading).	17.97
Double layer DNG loading (top & bottom sides).	**20.59**

6.5 3D-Printed Metastructure

In recent times, 3D printing has evolved, and new avenues for 3D-printed MMT structures or *Metastructures* have been opened and are being explored. Different types of 3D-printing material with different dielectric constants are available in the market at low cost. Using these materials, the required structures can be easily 3D-printed. These 3D-printed structures may behave and share similar properties to MMTs/ MSs. A horn antenna is 3D-printed for mm-Wave frequencies with high gain [252]. A 3D printed hemispherical structure is used to attain high gain at microwave frequencies [253]. A 3D-printed PGMS reflectarray is incorporated with the mm-Wave antenna for its gain

enhancement [254]. 3D-printed polariser to convert LP to CP waves [173], [255]. However, the 3D-printed Metastructure are large, which makes antenna design bulky and fragile.

A 3D-printed Metastructure is designed using readily found 3D printing material, Polylactic Acid (PLA), to enhance the gain of the dipole antenna. A 4 × 2 array of Metastructures is embedded onto a dipole antenna with an offset placement at each segment to tilt the beam radiation. The design and analysis of 3D-printed Metastructure and integration with a dipole antenna are further discussed.

6.5.1 Design of 3D-printed Metastructure UC

A cuboid shaped 3D-printed Metastructure is designed as shown in Fig. 6.30. The dielectric constant of the material PLA is 2.55, and its tangent loss (δ) is 0.05. The height of the cuboid is 3 mm, which is placed on the thin Rogers RT duroid 5880 substrate with a thickness of 0.254 mm, to ensure a low profile for the dipole antenna. The designed UC is employed with boundary conditions as PEC and PMC in the x-direction and y-direction, respectively, and waveports are applied in the z-direction.

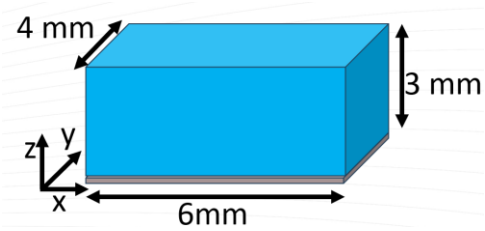

Fig. 6.30: Designed 3D-printed Metastructure UC.

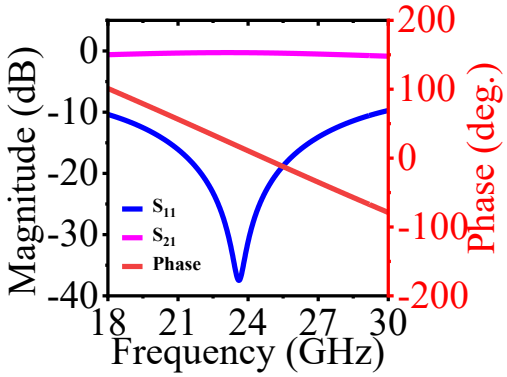

Fig. 6.31: S-parameters for the 3D-printed Metastructure and its Transmission Phase.

The simulated S-parameters for the 3D-printed Metastructure UC are plotted in Fig. 6.31, which shows that the designed UC has a UWB resonance from 18 GHz to 30 GHz and a transmission coefficient close to 0 dB with a negative phase passing through 0° at 24 GHz. This signifies that the designed 3D-printed Metastructure UC replicate the

MMT/MS properties. The MMT properties for the designed UC are extracted from [251] are shown in Fig. 6.31. These properties are similar to the MMT properties found for the copper-substrate based MMT UCs. Therefore, the designed 3D printed UC can be used as an MMT.

6.5.2 Designed dipole antenna integrated with Metastructures

The proposed dipole antenna size is 30×33 mm^2, and 0.254 mm is the thickness of the Rogers RT duroid 5880. As shown in Fig. 6.32, three directors are placed in front of the main dipole radiator at a distance of 1.7 mm to increase the directivity; also, they are placed offset from the dipole to deflect the beam radiation. An array of 4×2 Metastructures is placed in front of the three directors for the gain enhancement. Each 1×2 segment of the array is placed offset to the previous 1×2 segment by 1.5 mm in the +x-direction, as shown in Fig. 6.32. Consequently, the EM radiation in the +y-direction is deflected to 21º from the end-fire direction. Thus, beam deflection or tilting can be achieved. The parasitic arms of length Rl are introduced to the dipole antenna to improve the impedance BW. The dimensions of the dipole antenna are Gpl = 5 mm, Pl = 3.15 mm, Rl = 3 mm, Dd = 1.5 mm, Dl = 4 mm, d1 = 1.5 mm, and d2 = 1 mm.

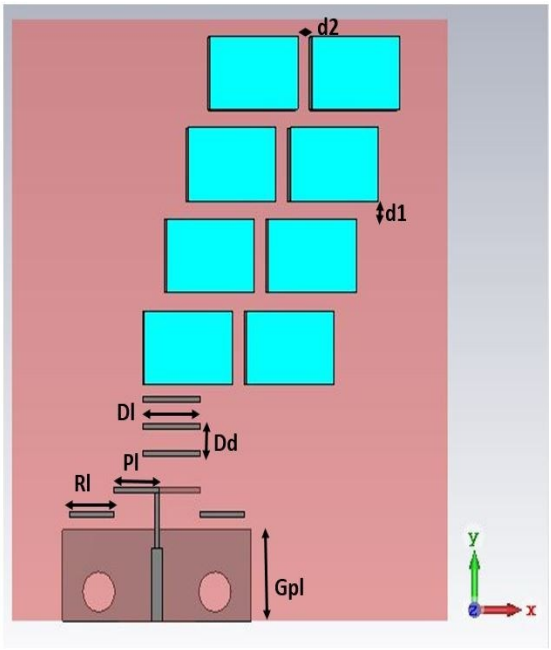

Fig. 6.32: Proposed Antenna design with 3D-printed Metastructure.

6.5.3 Results for the Dipole Antenna with 3D-printed Metastructure

The proposed antenna is designed in four stages. The first stage, a simple planar dipole antenna without any gain enhancement techniques, resonates from 21.73 GHz to 25.2 GHz. At the second stage, directors are added to the planar dipole antenna structure, which has a resonance from 22.2 GHz to 26.5 GHz; a little shift in the frequency is obtained due to

coupling between the antenna and the directors. At the third stage, a 4 × 2 array of 3D-printed Metastructures is incorporated into the planar dipole antenna with directors; this antenna resonates from 22.4 GHz to 26.6 GHz. At the final and fourth stage, parasitic arms are introduced to improve the impedance BW. The final stage antenna, which is the proposed antenna, resonates from 22 GHz to 26.6 GHz. The S-parameters for four stages are plotted in Fig. 6.33.

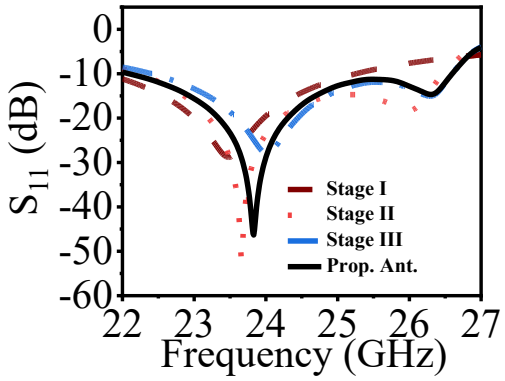

Fig. 6.33: S-parameters for the 4 stages of antenna design.

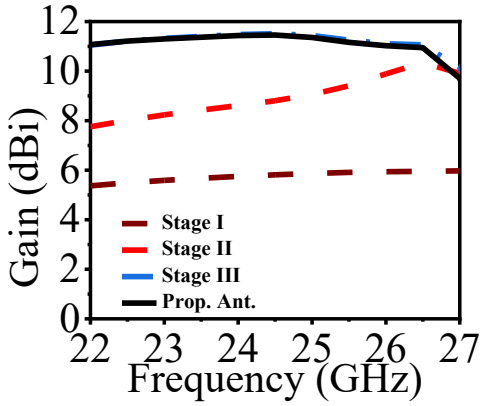

Fig. 6.34: Gain plot for the 4 stages of antenna design.

The primary aspect of designing a gain enhanced antenna is that the resonant frequencies should remain unaffected while achieving substantial enhancements for the operating BW. The gain plot shown in Fig. 6.34, suggests a high gain enhancement between stage one and stage four. At the first stage, the gain of the planar dipole antenna is less than 6 dBi for the operating bandwidth from 21.73 GHz to 25.2 GHz. At stage two, with the introduction of the directors, the gain has been enhanced by 3 dB to 5 dB, but the gain variation is close to 2.8 dB to 3 dB, which is not optimum for mm-Wave communication. Therefore, at stage three, to improve and stabilise the enhanced gain for the operating BW, a 3D-printed Metastructure is employed in the antenna structure. As shown in Fig. 6.34, the enhanced gain is improved significantly at lower frequencies from 7.2 dBi to 11.04 dBi and at higher spectrum, enhanced gain has improved from 10 dBi to 11 dBi. The maximum enhanced

improved gain is 11.45 dBi at 24.5 GHz, and a gain variance of 0.45 dBi is achieved for the operating BW from 22 GHz to 26.6 GHz. The achieved flat gain is optimum for the mm-Wave Communication.

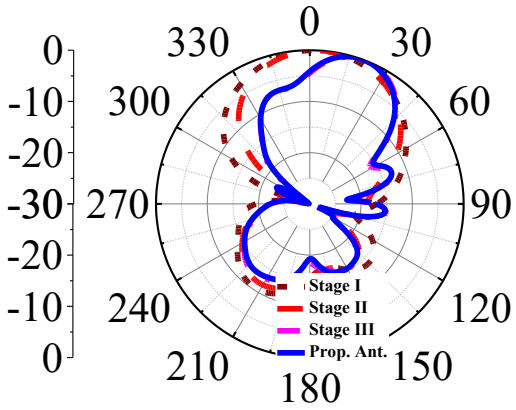

Fig. 6.35: Radiation Patterns at 26 GHz for the 4 stages of antenna design.

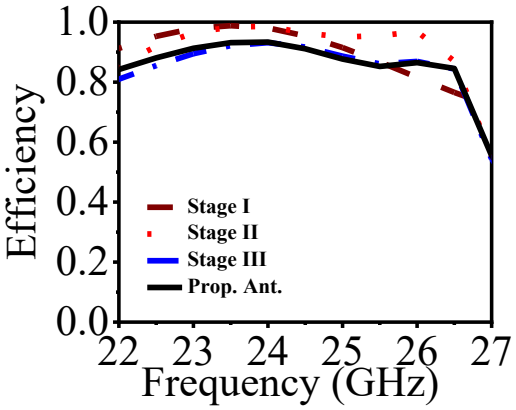

Fig. 6.36. Efficiency plot for the 4 stages of antenna design.

By placing the directors offset by 1 mm from the centre of the planar dipole antenna, the radiation is tilted to 5º, and with the placement of a 4 × 2 3D-printed Metastructure array, the gain is enhanced and the radiation beam is tilted to 21º. Since each 1 × 2 segment of the Metastructures is placed offset by 1.5 mm from the previous segment, the radiated energy gets coupled between these Metastructures, eventually tilting the radiation beam to 21º from end-fire direction. The radiation patterns in the xy-plane are shown in Fig. 6.35, which is the E-plane for the planar dipole antennas. The Fig. 6.35 also compares the radiation patterns for all four stages and depicts how the beam is tilted at every stage of antenna design. The Efficiency is plotted in Fig. 6.36, the proposed antenna has an efficiency between 85 % and 90 %. After introducing 3D-printed Metastructures, although the gain has enhanced, efficiency has dropped, due to a loss tangent (δ) of 0.05 of the PLA 3D-printing material. However, this drop in efficiency has not affected the gain of the antenna as shown in

Fig. 6. 34. With these features, the proposed dipole antenna with 3D-printed Metastructures is suitable for mm-Wave communication.

6.6 Summary

In this chapter, two mm-Wave MIMO antennas and two single mm-Wave antennas are proposed with gain enhancements for p2p communication. For these four antenna structures, four distinct MTM/MS structures were designed and analysed, such as UWB AMC, PGMS UC, DNG UC & 3D-printed Metastructures. All four structures have unique designs and novel results with high gain, which ensures the p2p connectivity between Users and mm-Wave Base stations. For *Antenna 1*, TM20 is excited in the AMC, which resulted in a UWB phase BW of 14.08 GHz from 23.49 GHz to 37.57 GHz measured at $\pm 90^{o}$. An array of 10 × 10 UCs is constructed to enhance the gain of the UWB MIMO antenna resonating from 23.27 GHz to 39.3 GHz. The maximum gain is enhanced from 5.66 dBi to 12.21 dBi at 31.5 GHz, and the obtained isolation is close to 20 dB for the operating BW. For *Antenna 2*, A PGMS lens is placed on top of the MIMO antenna at a distance of 5 mm to deflect the radiation beams in $\pm$ 24º. The total antenna profile is $0.71\lambda_0$ (λ_0 at 28 GHz), and the maximum enhanced value at 28 GHz is 9.71 dBi, and the isolation between the two ports is more than 15 dB. For *Antenna 3*, A DNG MMT arrays are placed on the top and bottom sides to enhance the gain of the antenna. With the Doble DNG loading, the gain has been enhanced to 9.8 dBi at 26 GHz, and the FTBR is increased from 10.81 dB to 20.6 dB. Lastly, for *Antenna 4*, 3D-printed Metastructures are incorporated into the antenna to enhance and stabilise the improved gain using the directors. The gain variation for *Antenna 4* is only 0.45 dB, and the maximum enhanced gain is 11.45 dBi. These features make the proposed antenna structures suitable for the p2p 5G mm-Wave communication.

Chapter 7

Conclusion, Future Scope & Social Impact

7.1 Conclusion

To improve p2p 5G communication, high gain and wide impedance BW antennas play an important role. Antenna parameters, such as BW, Directivity, Gain, Efficiency & Polarisation, can be influenced as per user demand employing MMTs/MSs. In this thesis, an in-depth investigation is conducted for the design and analysis of the gain enhanced microstrip antennas using MMT, MS & 3D-printed Metastructures. To satisfy user demand for high data rates in Gbps, wideband/UWB antennas with high and compact sizes are the main attraction for the researchers. Therefore, through a combination of theoretical and simulation analyses, different wideband/ UWB antennas, embedded with MMT/ MS, are designed and analysed to enhance their gain while maintaining a low antenna profile. The other antenna parameters, such as directivity, polarisation and efficiency, are also equally significant, as high gain. Therefore, MMTs/ MS are designed in such a way that these parameters can also be influenced. The microstrip or patch antennas are designed for 5G spectrums spanning 2 GHz to 8 GHz, 10 GHz to 13 GHz and 20 GHz to 40 GHz, and different MMTs/MSs such as AMC, PGMS, PRMS, DNG & 3D-printed Metasurface are utilised to enhance the gain of these antennas.

A Sub-6 GHz MIMO antenna is designed, which has UWB impedance BW from 2.37 GHz to 8 GHz, and the fractional BW stands at 108.58 % for the IoT/IoV applications. To enhance the gain of the MIMO antenna, an AMC is designed with dual rings, which generate dual resonance. These dual resonances have two PMC and PEC bands, which, in combination with the ground of the AMC, enhanced the gain of the MIMO antenna. An AMC array of size 5 × 8 AMC array is placed at a height 0.11 λ_o (λ_o at 2.37 GHz). Meanwhile, to improve port isolation, the same AMC structure wall of size 1 × 3 is constructed and placed between the ports, enhancing the isolation. The maximum enhanced gain achieved is 7 dBi from 2.3 dBi at 3 GHz, and port isolation > 19.66 dB for the operating frequencies. The Sub-6 GHz antenna integrated with the vehicle retains the free space radiation patterns. The MIMO parameters, ECC < 0.0037, CCL < 0.12 bits/s/Hz, TARC < -10 dB are in the acceptable range for the MIMO communication. The Sub-6 GHz UWB MIMO antenna structure size is only 0.39 λ_o × 0.63 λ_o × 0.14 λ_o, and its impedance BW covers all major frequencies such as WiFi/ WiMax/ Bluetooth/ LTE Frequency, Mid Band, 5 GHz band and WiFi-6E, which makes it advantageous for the IoT/ IoV applications.

The avoid transmission and reception loss through polarisation mismatch, CP antennas are always preferred in the base station/ satellite communication. However, the ARBW are narrow compared to impedance BW. It is challenging to match ARBW with the impedance BW. Therefore, a PRMS is designed and modified to enhance the ARBW

of the PCA by forming an FPC cavity of an array of 9 × 9 PRMS UCs. The EP waves are converted into CP waves by optimising 9 × 9 PRMS UCs of the FPC cavity array. The proposed antenna, FPC-PCA, is an RHCP antenna that has resonance from 9.9 GHz to 12.31 GHz and 3 dB ARBW from 9.9 GHz to 12.21 GHz. This implies 2.31 GHz of ARBW matches with its 2.41 GHz of impedance BW. The FPC-PCA has a cavity height of 12 mm, and the volume is 80×80×15.89 mm^3. The 3 dB ARBW is enhanced from 790 MHz to 2.31 GHz; meanwhile, the gain has enhanced from 7.3 dBi to 17.1 dBi at 10 GHz. The design PRMS UC or array is compatible with RHCP waves and LHCP waves, making it CP friendly. These features make the proposed antenna suitable for CubeSat applications.

The above designed CP CubeSat antenna needs a terrestrial CP antenna with high gain and low profile antenna, operating at 10 GHz to 12 GHz for p2p terrestrial 5G communication. A polarisation insensitive PGMS-FL array of size 15 × 15 UCs is constructed to generate high gain with narrow beams. Each PGMS UC generates a time delay (ΔT) ranging from 6.76 ps to 46.13 ps at 11 GHz and phase gradience 0º to 182.68º. The attained beamwidths are between 13.2º and 16.5º for the xz-plane and yz-plane. Maximum enhanced gain 17.7 dBi at 11.2 GHz, and gain variation is less than 2.5 dB for the impedance BW from 10.42 GHz to 13.26 GHz. The polarisation insensitive property is leveraged to attain 3dB ARBW from 10.51 GHz to 11.7 GHz. The size of the PGMS-FL is 5.21 λ_0 × 5.21 λ_0, focal distance (*f*) of 1.04 λ_0, PGMS lens profile is 0.124 λ_0 (λ_0 at 10.42), and *f/D* is 0.2. This verified that the proposed PGMS-FL antenna has a compact profile with high gain and narrow beam widths.

Although lower spectrum frequencies have better propagation, the growing demands for higher data rates could be overcome by utilising mm-Wave frequencies high gain antennas. Therefore, a UWB mm-Wave MIMO antenna embedded with UWB AMC phase BW. The UWB AMC phase BW of 14.08 GHz, ranging from 23.49 GHz to 37.57 GHz, is designed by exciting the TM20 mode by etching capacitive slots in the AMC patch. A 10 × 10 UWB AMC array is placed at a height of 0.395 λ_0 (λ_0 at 23.27 GHz) below the MIMO antenna to enhance its gain. The gain is enhanced from 8.5 dBi to 12.21 dBi for the resonating frequencies from 23.27 GHz to 39.3 GHz, and port isolation is found to be more than 19 dB for the orthogonally placed MIMO antenna elements. The size of the proposed antenna is 3.95 λ_0 × 3.95 λ_0 × 0.395 λ_0.

In the second mm-Wave MIMO antenna, a PGMS beam tilting lens is designed to deflect EM radiation ± 24º from the broadside direction. This ensures the NLOS communication and increases the SNR. The PGMS lens has the phase gradience of 0º to 226.5º, with transmission magnitude more than 0.7. A 5 × 12 PGMS array is constructed and placed on top of the MIMO antenna at a height of 0.46 λ_0 (λ_0 at 28 GHz) to tilt radiation away from the broadside direction. The proposed antenna resonates from 27.4 GHz to 28.26 GHz, and the port isolation is more than 15.71 dB. The obtained gain is between 8.7 dBi and 9.71 dBi.

In the third mm-Wave antenna, the DNG UC are designed to enhance the gain and increase the FTBR of the planar dipole antenna. The DNG UC have the impedance BW

of 8 GHz, and the transmission coefficient is close to 0 dB. Two 5 × 4 arrays are embedded in the planar dipole antenna on the top side and bottom side for gain enhancement. The gain is enhanced by 4 dB for the operating BW from 24 GHz to 28 GHz. The enhanced gain is between 8.99 dBi and 9.8 dBi. The FTBR is increased from 10.81 to 20.6 dB. The total size of the antenna is only 1.73 λ_0 × 1.64 λ_0 (λ_0 at 26 GHz).

In the fourth mm-Wave antenna, a 3D-printed Metastructures 4 × 2 array is introduced, a planar dipole antenna to enhance and stabilise its gain. A PLA 3D-printing material with a dielectric constant of 2.55 is chosen for its readily availability. The offset placement of the 3D-printed Metastructures array and director tilted the beam from end-fire direction to +21°. The proposed antenna resonates from 22 GHz to 26.6 GHz, and the enhanced gain varies from 11.07 dBi to 11.45 dBi, i.e. a flat gain is achieved by using a 3D-printed Metastructures array. The size of the planar dipole antenna with 3D-printed Metastructures is 2.4 λ_0 × 2.64 λ_0 × 0.26 λ_0 (λ_0 at 24 GHz). The achieved high in all four structures is suitable for mm-Wave 5Gcommunication with a compact antenna size or profile.

To sum up, the findings in each chapter highlight the significance of the design and structure of the MMT/ MS UC. The symmetry, polarisation insensitivity, and polarisation stability for different angles of incidence are crucial for the gain enhancement of the antenna. The proposed gain enhanced microstrip antenna designs operating at Wifi / WiMax / Bluetooth / LTE frequency, Mid-band, 5 GHz band and Wifi-6E and downlink satcom band, X-band, MVDDS and mm-Wave frequencies offer promising results with their compact and low profile for 5G communication.

7.2 Future Scope

The results and findings open up new avenues for future research in terms of optimisation, fabrication and real-time tested results to improve p2p2 communication.

- **Optimisation:**
  - Although the proposed antenna delivers promising results of gain enhancement and high efficiency for the wideband/UWB antenna.
  - There is still room for improvement and analysis to present better results. Optimisation of these antennas may enhance the performance and analysis.
- **Fabrication:**
  - Post optimisation, the antenna needs to be fabricated with precision through machine and less human interference is important.
  - This will improve the quality of antenna structures and precision in measured results.

- 3D-printed stands to hold the MMT/MS array, which will give stability to the antenna structure to achieve more precise measured results.

- **Real-Time Measurements:**
  - The proposed antennas can be tested in a real-time environment by placing a Sub-6 GHz antenna on vehicles for IoT/IoV applications.
  - An FPC antenna can be placed on a 1U CubeSat, and measurements can be carried out. The PGMS-FL antenna can be tested in an open-air environment.
  - The mm-Wave antennas can be installed in the small base stations to measure their radiation pattern with enhanced gain to verify their potential as base station antennas.

- **Real-Time Deployment:**
  - If satisfactory results are obtained in the real-time measurements, then these antennas can be deployed as the 5G base station antennas in the Bus, Metro, Cars, Satellites, and Small Base Stations for the close proximity p2p communication.

7.3 Social Impact

The rapid growth in wireless communication and demand for high data rates has forced the deployment of 5G for the betterment of society. This will enable, high speed, reliable and seamless connection. This thesis addresses several crucial aspects and challenges, such as high gain variance, mismatch of ARBW and impedance BW, low FTBR in compact devices, polarisation sensitivity, importance of symmetric designs etc. The proposed antenna designs, which cover Sub-6 GHz, X-band, and mm-Wave frequencies, have a profound social impact in several domains:

- **Seamless Connectivity:**
  - The Wifi / WiMax / Bluetooth / LTE frequency, Mid-band, 5 GHz band and Wifi-6E bands provide excellent connectivity and high data rates through UWB Sub-6 GHz MIMO antenna in the urban and populated areas.
  - The PGMS-FL antenna can provide connectivity in rural areas where terrestrial infrastructure is lacking
  - The mm-Wave antennas with gain and low variance, with their huge BW, can provide data rates in Gbps in the local area network (LAN).

- **Intelligent Vehicular Transportation:**

- Sub-6 GHz MIMO antennas designed for IoV applications, which enhance vehicle-to-vehicle (V2V) and vehicle-to-infrastructure (V2I) communication.
- This contributes to safer roadways, intelligent traffic systems, and the foundation for autonomous vehicles.

- **Contribution to Space and Satellite Communication:**
  - The CP CubeSat antenna with high gain supports small satellite missions, enabling affordable space research, Earth observation, and global communication.
  - These advancements promote low-cost satellite launches, benefiting climate monitoring, disaster management, and global connectivity.

7.4 Summary

In summary, the proposed gain enhanced antennas operate over different frequency bands from 2 GHz to 40 GHz, enveloping crucial 5G frequencies for p2p communication. The designed patch antennas have a large BWs to accommodate high data traffic, and the addition of MMT/MS to the antenna structures has significantly enhanced the gain of the antenna. The directive patterns of the antennas will serve a specific set of users in a given direction. The high will consequently reduce the interference and increase the SNR. The gain enhanced MIMO antenna configuration diminishes fading effects, improves coverage, capacity and reliability. Collectively, these features improve wireless link capacity. The outcomes of this research not only provide technical advancements in antenna engineering but also contribute to the betterment of society by connecting people to the internet and empowering them with the power of 5G wireless communication.